MiNDSTEp differential photometry of the gravitationally lensed quasars WFI2033-4723, HE0047-1756 and Q2237+0305

Emanuela Giannini

2016

Cover picture: *The Phoenix*, Marisa Milan (2014)

Dissertation
submitted to the
Combined Faculties of Natural Sciences and Mathematics
of the Ruperto-Carola-University of Heidelberg, Germany
for the degree of
Doctor of Natural Sciences

Put forward by
Emanuela Giannini
born in: Colleferro (RM), Italy
Oral examination: February 8th, 2017

MiNDSTEp differential photometry of the gravitationally lensed quasars WFI2033-4723, HE0047-1756 and Q2237+0305

M.Sc. Emanuela Giannini
Astronomisches Rechen–Institut
Zentrum für Astronomie der Universität Heidelberg
Fakultät für Physik und Astronomie

Referees: Prof. Dr. Joachim Wambsganss
Dr. Sabine Reffert

A Lea e Rosa

Nothing is ever really lost, or can be lost,
No birth, identity, form–no object of the world.
Nor life, nor force, nor any visible thing;
Appearance must not foil, nor shifted sphere confuse thy brain.
Ample are time and space–ample the fields of Nature.
The body, sluggish, aged, cold–the embers left from earlier fires,
The light in the eye grown dim, shall duly flame again;
The sun now low in the west rises for mornings and for noons continual;
To frozen clods ever the spring's invisible law returns,
With grass and flowers and summer fruits and corn.

Continuities—Walt Whitman

Never, never, never give up.

—Winston Churchill

Abstract

This work focusses on studying the brightness variation of gravitationally lensed multiply imaged quasars. The main goal is the optimization of the relative differential photometry procedures, which are based on the difference image analysis (DIA) method. Moreover, it aims at isolating uncorrelated flux variations among the quasar images, which can be explained as due to quasar microlensing events, and at the estimation of the time delays of the observed systems from the retrieved light curves.
We present V and R photometry of the gravitationally lensed quasars WFI 2033-4723, HE 0047-1756 and Q 2237+0305. The analyzed data belong to the MiNDSTEp collaboration and were taken with the 1.54 m Danish telescope at ESO/La Silla from 2008 to 2012. The differential photometry is based on the already published method by Alard & Lupton as implemented in the HOTPAnTS package, and additionally uses the GALFIT package for obtaining the quasar photometry.
The quasar WFI 2033-4723 shows brightness variations of ≈ 0.5 mag in V and R during the campaign. The two lensed components of quasar HE 0047-1756 vary by $\approx 0.2 - 0.3$ mag within five years. We provide for the first time an estimate of the time delay of component B with respect to A of $\Delta t = (7.6 \pm 1.8)$ days for this object. We also find evidence for a secular evolution of the magnitude difference between components A and B in both filters, which we explain as due to a long-duration microlensing event. We also find that both quasars WFI 2033-4723 and HE 0047-1756 become bluer when brighter, which is consistent with previous studies. The quasar Q 2237+0305 shows impressive uncorrelated variations of the four components in both the V and R bands, with brightness variations between ≈ 0.2 and ≈ 1.3 mag. In particular, component D shows flux variations of ≈ 1.3 mag in the V band and ≈ 0.8 mag in the R band during the 5-year monitoring campaign, along a caustic-crossing feature of the light curve. We also find that the color of this component becomes redder by ≈ 0.6 mag while it becomes fainter. Image C becomes brighter by ≈ 0.7 mag between the last two monitoring seasons and this again suggests a high-magnification microlensing event.

Zusammenfassung

Diese Arbeit konzentriert sich auf die Studie der Helligkeitsveränderung von mehrfach abgebildeten gravitationsgelinsten Quasaren. Das Hauptziel ist die Optimierung der relativen differentiellen Photometrie-Verfahren, die auf Methoden der Differenz-Bildanalyse (DIA) basieren. Darüber hinaus strebt sie die Isolation unkorrelierter Fluss-Variation unter den Quasar-Bildern an, die durch Quasar-Mikrolinsenereignisse erklärt werden können, und beabsichtigt die Schätzung von Zeitverzögerungen der beobachteten Systeme von den gewonnenen Lichtkurven. Wir präsentieren V- und R-Photometrie der

gravitationsgelinsten Quasare WFI 2033-4723, HE 0047-1756 und Q 2237+0305. Die analysierten Daten gehören zum MiNDSTEp-Kollaboratorium und wurden mit dem 1,54 m großen Dänischen Teleskop in ESO/La Silla zwischen 2008 und 2012 aufgenommen. Die differentielle Photometrie basiert auf der bereits veröffentlichten Alard- und Lupton-Methode, wie sie im HOTPAnTS-Paket implementiert wurde, und verwendet zusätzlich das GALFIT-Paket, um die Quasar-Photometrie zu bestimmen. Der Quasar WFI 2033-4723 zeigt während der Kampagne Helligkeitsveränderungen in einer Größe von $\approx 0,5$ mag in V und R. Die beiden gelinsten Komponenten des Quasars HE 0047-1756 variieren zwischen $\approx 0,2 - 0,3$ mag innerhalb von fünf Jahren. Für dieses Objekt bieten wir erstmals eine Schätzung der Zeitverzögerung der Komponente B im Bezug auf A von $\Delta t = (7,6 \pm 1,8)$ Tagen an. Weiterhin finden wir in beiden Filtern einen Hinweis für eine säkulare Evolution des Helligkeitsunterschiedes zwischen den Komponenten A und B, die wir durch ein lang anhaltendes Mikrolinsenereignis erklären können. Wir finden außerdem heraus, dass beide Quasare, WFI 2033-4723 und HE 0047-1756, blauer werden mit Zunahme der Helligkeit, welches konsistent mit vorherigen Studien ist. Der Quasar Q 2237+0305 zeigt beeindruckende unkorrelierte Variationen in seinen vier Komponenten mit Helligkeitsveränderungen zwischen $\approx 0,2$ und $\approx 1,3$ mag sowohl im V- als auch im R-Band. Insbesondere Komponente D zeigt Fluss-Variationen innerhalb der fünfmonatigen Beobachtungskampange von $\approx 1,3$ mag im V-Band und $\approx 0,8$ mag im R-Band in einem kaustikähnlichen Merkmal der Lichtkurve. Wir finden außerdem heraus, dass die Farbe dieser Komponente um $\approx 0,6$ mag roter wird. Bild C wird zwischen zwei Beobachtungssaisons um $\approx 0,7$ mag heller und dies deutet ebenfalls auf ein Mikrolinsenereignis großer Verstärkung hin.

Contents

1 Motivation

Since the prediction of the gravitational lensing effect ([2], [44]), according to which the light rays emitted from a distant background source are bent by an intervening gravitational field, first proposed in the early 18th century, impressive progress has been made in the attempt of observing this phenomenon. It has been classified in a variety of regimes, called strong, weak and micro-lensing. This means that different kinds of light sources and gravitational fields, which are placed at different distances from the observer, concur on realising a plethora of gravitational lensing system configurations, which act on a multitude of angular scales. This phenomenon has often contributed to independent measurements and confirmations of results obtained by applying traditional principles and methods. For example it provides an independent method of measuring the Hubble constant [121] and a further means of investigating the existence and nature of the dark matter (for a detailed review see [94]).
Gravitational lensing magnifies or demagnifies the flux of the affected images, distorts their original shapes, changes their center of light positions and produces multiple images. Strong lensing usually involves a background galactic source and a foreground lensing galaxy and produces multiple images of the source, which can be strongly distorted and elongated (arcs), and have angular separations of the order of arcseconds.
Weak lensing happens when a foreground matter distribution, like a cluster of galaxies, affects the light sources behind it with a little overall effect that can be detected only by measuring the average distortion of a multitude of slightly distorted source shapes.
Microlensing arises when the gravitational field of a Galactic star bends the light from a background Galactic star. It also happens when the compact objects in a foreground galaxy affect the light from the multiple images of a strongly lensed quasar. This gives rise to the *quasar microlensing phenomenon*. In these cases mutiple images are produced on angular scales from milliarcseconds to microarcseconds. This implies that the production of the multiple images is undetactable. Nevertheless the overall flux variation can be measured.
To list only a few results obtained by considering the gravitational lensing phenomenon we mention that the validity of the general theory of relativity has also been confirmed by the observation of multiply imaged quasars [20] and strongly distorted galactic arcs

[112].
The measurement of the Hubble constant has been optimized in the last 25 years by observing systems such as supernovae ([61], [70]), Cepheids [51] and strong lensing systems [74].
The existence of new exoplanets orbiting distant Galactic stars has been confirmed through the radial velocity method [82], the observation of transits [56] and, more recently, by the method of microlensing of Galactic bulge stars [16].
Moreover, the nature of the extragalactic halos has also been investigated by studying their gravitational effect on background sources [63].
Of particular interest for this thesis is the fact that the spatial structure of multiply imaged quasars has been studied by observing the effect of compact objects in foreground galaxies on their multiply imaged components [20]. The inner structure of quasars is not otherwise easily accessible and quasar microlensing is a unique method for studying the physical sizes of these lensed systems. The method requires constant monitoring of the multiply imaged quasar in order to build their light curves. From those, the source size can be estimated, according to the principle that the microlensing features of the light curves depend on the size of the lensed source, which in turn depends on the observed wavelength. Enourmous effort has been made in this direction and many ground- and space-based observatories have contributed the coverage in wavelength and time for many multiply imaged quasars in the last 30 years ([114], [96]). In particular, the Optical Gravitational Lensing Experiment [111] – OGLE – has been monitoring several multiply imaged quasars since 1997 and has produced those among the longest existing light curves. Despite the enourmous amount of data produced, this application of gravitational lensing is currently shared and applied by a quite small community, meaning that its great potential is not yet fully exploited.
Here we present our implementation of an already published method of difference image analysis (DIA) and apply it to several multiply imaged quasars of great interest, for which we received data from 2008 to 2012, in order to build their light curves. Besides analyzing the obtained data, the aim is also to provide us with a method to retrieve light curves at a higher speed when getting new quasar monitoring data. The multiply imaged quasars analyzed in this work, WFI 2033-4723, HE 0047-1756 and Q 2237+0305, are very interesting gravitational systems for which we have been able to prolong the already existing light curves and proceed, in the case of HE 0047-1756, to the calculation of the time delay between its two images. This is the time lag between the arrival time of the light rays emitted from the two images, as due to the different geometrical pathways and the effect on light of the gravitational field they cross. The determination of the time delays from several lensing systems concur on the determination of the Hubble constant H_0 at an increased statistical accuracy and constitutes one of the most valuable contributes of gravitational lensing to Cosmology.

2

Introduction to AGNs and Quasar Microlensing

2.1 ACTIVE GALACTIC NUCLEI

2.1.1 The AGN class

In this section we present the basic theory behind the phenomenon of active galactic nuclei (see [144] and references therein; see also [80]).

Active galactic nuclei, shortly AGNs, are galaxies with a compact central region which emits strongly over the entire electromagnetic spectrum. Many of them emit strongly in the optical, UV and X-ray regimes. Others are powerful radio sources. All emit high energy amounts from a tiny volume, comparable to that occupied by the Sun and its planetary system. AGNs are believed to host central super massive black holes (SMBHs) with masses in the range $10^6 - 10^{10}\ M_\odot$. Although all galaxies seem to contain SMBHs ([92],[60]), those in AGNs accrete matter, whose gravitational energy, possibly along with the rotational energy of the SMBH, is transferred into electromagnetic radiation. Moreover, part of the accreting material escapes from the accretion disk as collimated jets and uncollimated outflows, which are called winds. The size scales of the AGN phenomenon span 11 orders of magnitude, from the event horizon scales of the SMBH (10^{13} cm) to the jet scales, which can be as large as a few Mpc [91].
AGNs are among the most luminous sources in the universe, with luminosities of 10^{45} – 10^{48} erg s^{-1}. Their observational differences are generally believed to derive from looking at few types of AGNs from different angles with respect to a simmetry axis. Besides, the physical explanation of the observed variety of AGNs has also to be attributed to their different accretion flows and environments. This means that the total luminosity [83] and the cosmic epoch of the AGN [150] play an important role as well.

Figure 2.1 shows the structure of the inner working mechanism of an AGN. It shows what are the components producing most of the observational features seen in AGNs:

1. A central SMBH is located at the center of an accretion disk, whose typical size is

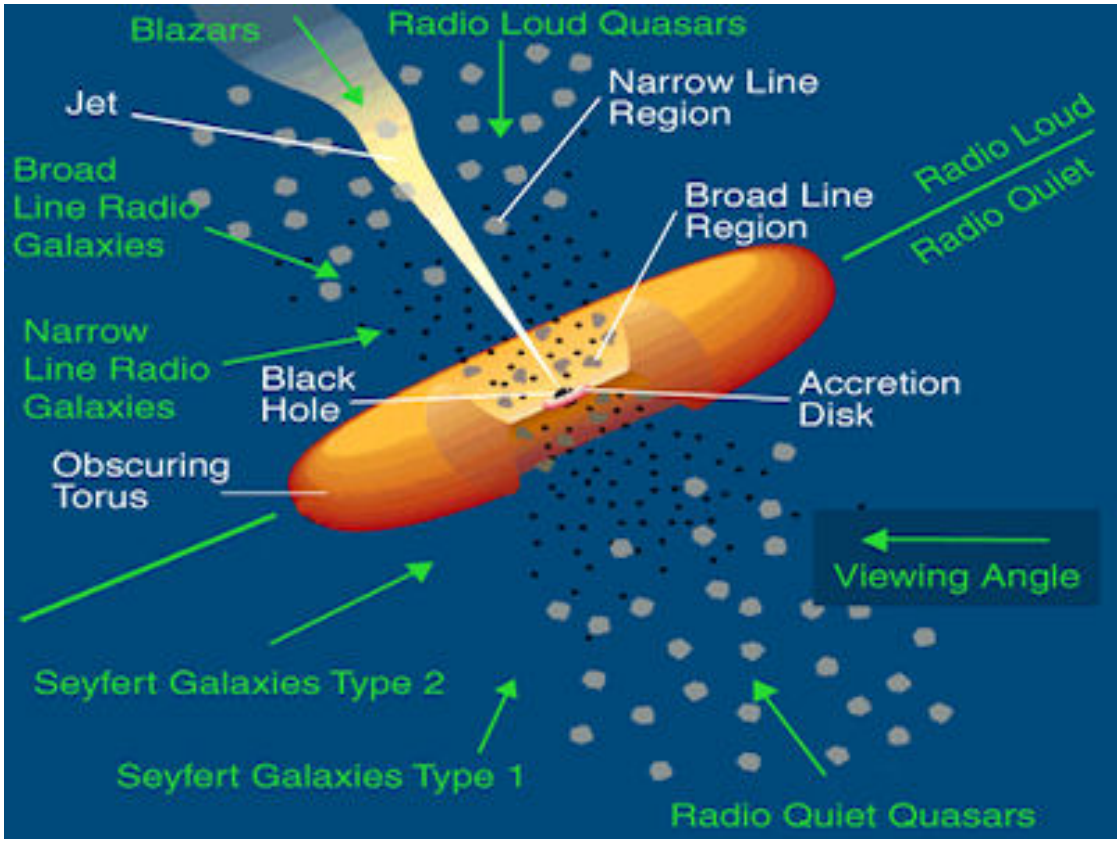

Figure 2.1: Sketch of the working mechanism at the basis of the AGN phenomena. The central SMBH, with mass in the range $10^6 - 10^{10}\,M_\odot$, is surrounded by an accretion disk, whose typical size is $\sim 10^{14} - 10^{15}$ cm. Broad emission lines are emitted from gas clouds orbiting the SMBH at a distance of $\sim 10^{16} - 10^{17}$ cm. A dusty torus, with inner radius of $\sim 10^{17}$ cm, obscures the BLR if the AGN is observed at a large viewing angle with respect to the simmetry axis. Clouds at much larger distances of $\sim 10^{18} - 10^{20}$ cm from the central engine emit narrow lines. Radio jets, in favourable conditions, are channelled from the regions close to the SMBH (at $\sim 10^{15}$ cm) up to several 10^{24} cm in radio loud AGNs. The sketch is reproduced from www.oa.uj.edu.pl.

$\sim 10^{14} - 10^{15}$ cm. The accretion disk is believed to derive from gas falling into the central SMBH. The gas slowly flows towards the AGN center, forming a disk that rotates around the central SMBH ([89], [138]), and whose angular momentum is transferred towards the outskirts of the disk as a result of its viscosity. This process heats the disk, which therefore radiates away its gravitational energy over a broad range of wavelengths [140]. The resulting continuum thermal emission, defined as Big Blue Bump, covers a rest frame emission range from the optical to the soft X-ray band ([28],[78]). A fraction of the continuum emission can get comptonized by a corona of hot material, surrounding the disk. The resulting radiation is emitted in the hard X-ray band.

2. Dense gas clouds, at $\sim 10^{16} - 10^{17}$ cm from the disk, constitute the Broad Line Region (BLR), which gives rise to broad emission lines. The line widths reveal that the orbital speed of the emitting gas clouds is of the order of $\sim 10^4$ kms^{-1}. Farther clouds, placed at a $\sim 10^{18} - 10^{20}$ cm distance, constitute the Narrow Line Region (NLR), which emits much narrower emission lines, with widths corresponding to orbital velocities below 10^3 kms^{-1}. The lines from strongly ionized atoms in the BLR vary according to the continuum variations with time lags of a few days. The low-ionized atom lines instead vary with delays of a few weeks, as one would expect if they are excited at larger distances from the central nucleus. The narrow emission lines, on the other hand, do not show any significative variations, since they originate much farther away from the central engine. [1]

3. In a radio-loud AGN, favorable conditions (i.e. strong magnetic fields) have determined the formation of collimated, highly relativistic radio jets, which extend from the inner regions of the AGN over distances as long as $\sim 10^{24}$ cm. The jets, in the regions adjacent to the SMBH, are believed to be mostly made up by electromagnetic radiation. At distances of ∼pc, the electromagnetic energy in transferred to electrons, positrons or to the Interstellar Medium (ISM) ([120],[88],[131], [14]).

   Roughly 10% – 20% of AGNs are radio loud. They are classified in two types [48]: the low-power Fanaroff-Riley Class I (FRI), with radio features distributed closer to the center, and the high-power Fanaroff-Riley Class II (FRII), with larger distances between the jet extremities, of the order of a few Mpc.

   A large number of radio-loud AGNs also shows X-ray emission from the jets

[1] Observations of the BLR emission lines and the disk continuum emission provide a means of estimating the mass of the SMBH, by making use of the reverberation mapping technique [117]. This method uses the widths of the emission lines (from which the orbital velocities of the clouds are estimated) and the time lags between the variability of the continuum and that of the line fluxes (hence an estimate of the distance between the engine and the BLR). Velocity and distance of the BLR provide the orbital parameters necessary for the estimation of the SMBH mass.

[62]. For the Fanaroff-Riley I, the radio to X-ray emission well matches the Synchrotron emission from TeV electrons in magnetic fields of $< 1000\,\mu$G. On the other hand, for the Fanaroff-Riley II, the radio to X-ray spectrum is not well represented by a single Synchrotron component. For these sources, the electromagnetic spectrum between the optical and the γ-ray bands becomes brighter. This might be due to inverse Compton scattering of Cosmic Microwave Background (CMB) photons from highly relativistic electrons ([12], [5], [176]).

AGNs jets might play a role in galactic and galaxy cluster systems, because of their possible contribution to the heating processes of the ISM and intracluster medium, which would ultimately affect the star formation process [97].

4. A thick dusty torus, with an inner radius of $\sim 10^{17}$ cm, obscures the accretion disk and the BLR when the AGN is observed at an angle with respect to its simmetry axis. It re-emits the central engine continuum in the infrared. The presence of the above torus can explain some of the differences between different AGN classes ([46], [106]). The appearance of the observed object depends on the viewing angle, whether or not the AGN has a jet emission, and the luminosity of the central engine. If the torus is on the line of sight towards the AGN, it will conceal the BLR and only narrow lines will be observed, producing the Type-2 Seyfert galaxies (all Seyfert galaxies are in general quite modest radio sources found in spiral galaxies) and the narrow line FRI and FRII radio galaxies (all FRI and FRII radio galaxies are in general observed in giant elliptical galaxies, with highly polarized synchrotron radiation up to $10^{12}\,L_{\odot}$). If the torus does not obscure the BLR, the AGN will appear as Type-1 Seyfert galaxies, radio quiet quasi-stellar objects (QSOs), broad line FRI and FRII radio galaxies and quasars, quasi stellar radio sources. Although the terms quasar and QSO are today widely used as synonims – and we will only use the term quasar in the following – the word quasar was introduced to describe extremely luminous, high-redshift, star-like radio sources, while the term QSO was attributed later to apparently stellar sources with no intense radio counterparts. Quasars are today regarded as powerful versions of a Seyfert galaxy, with the bolometric luminosity of transition between the two classes at $\sim 10^{11}\,L_{\odot}$. Both emit abundantly from the infrared to the X-rays, most of them are not strong radio emitters. At small observing angles, the non-thermal continuum emission from the relativistic jets will prevail and the quasars will appear as radio-loud blazars, with strong variability on scales of days and strongly polarized optical and radio emission.

5. The observation of blue-shifted broad and narrow absorption lines from the optical to the X-ray wavelengths implies the existence of fast AGN outflows or winds [22]. The location at which the broad absorption line (BAL) winds are loaded is still uncertain, whereas it is believed that the narrow absorption line (NAL) winds

are launched at about the same distance as the NLR, of the order of ∼pc.

The emission from AGNs is in general a means of studying the objects, diffuse matter and radiation fields between us and the AGNs.

2.1.2 Black hole formation and accretion

According to most black hole (BH) formation models, primordial black holes appeared at redshift z larger than 15. There are two leading scenarios explaining how the first black holes have appeared. The first states that the primordial BHs are the final product of the evolution of the first ultra metal-poor generation of stars. Such BHs emerged at z∼ 20 with masses $100-1000\,M_{\odot}$ ([167],[103]). The other scenario attributes the formation of $10^2-10^5\,M_{\odot}$ BHs to direct gas collapse at z∼ $10-15$ ([17],[33]). Since the typical observed SMBH mass is of $10^6-10^9\,M_{\odot}$, most of the growth happens in AGN systems, particularly in quasars ([89], [143],[148]). Their activity is likely ignited by major mergers of two massive galaxies [13] and is often referred to as *quasar phase*. A clear correlation between the quasar phase and major mergers has been observed in some luminous quasars and infrared luminous star forming galaxies [128]. On the other hand, most AGNs are neither in mergers nor in particularly populated environments [32]. Other galaxy internal interactions might explain the moderate activity in these AGNs, defined as secular-driven AGNs ([32], [100], [79]). Several studies ([151], [149]) show that the number of AGNs driven by secular processes is about 10 times larger than that of merger-driven AGNs. The latter make up for the ∼ 60% of the whole SMBH growth at high redshifts z > 1, where mergers are gas richer and relatively more numerous [67]. The amount of matter that the SMBH accretes during the quasar phase, which lasts ∼ 10^8 years ([93], [139], [34]), is of about $10^8\,M_{\odot}$.

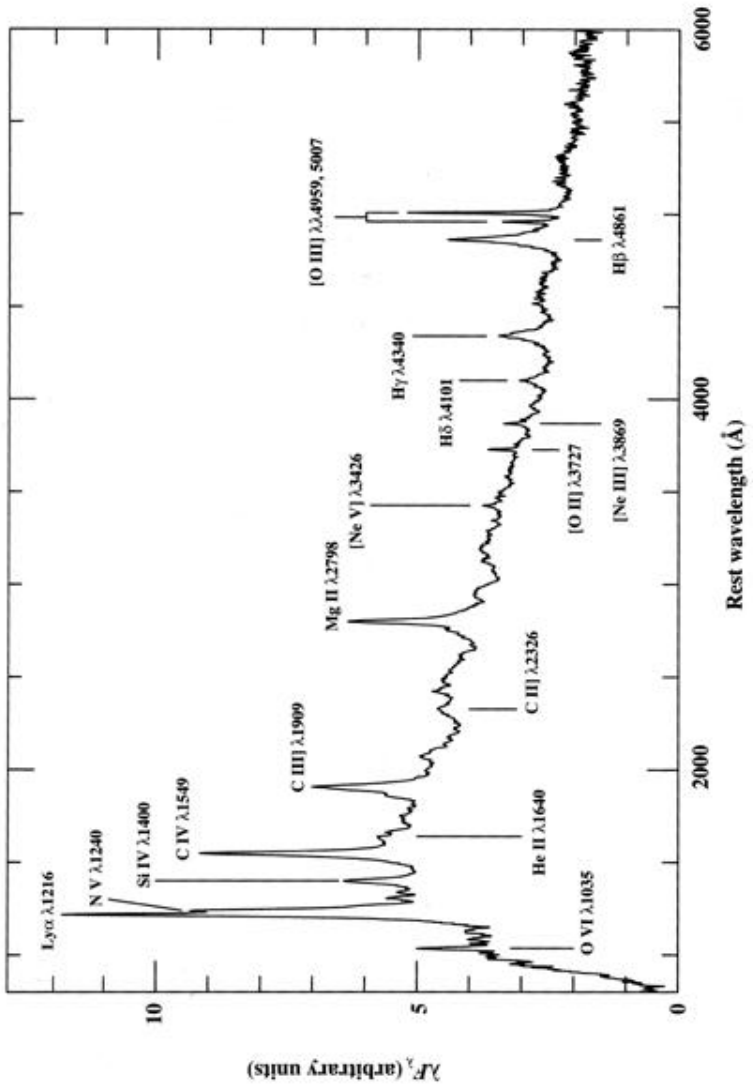

Figure 2.2: A mean quasar spectrum obtained by averaging spectra of more than 700 quasars from the Large Bright Quasar Survey [50]. The main emission lines are indicated. Courtesy of P. J. Francis and C. B. Foltz. Adapted from [1].

2.1.3 Zooming-in on Quasars

Quasars are the most luminous and distant objects among the AGNs. They were identified as stellar-appearing, highly redshifted sources of radio and optical radiation, which showed very broad non-stellar emission lines ([132], [95]). The emitted radiation extends from the γ-rays over the radio regime, with intense emission in the UV and optical bands. Only a small minority (5-10%) of these sources are the strong radio sources which defined the original quasar class. The remaining radio-quiet quasars have less than 1% the radio power of the radio-loud versions. The latter can be up to a hundred times more powerful in the radio regime than a typical radio galaxy. In this case the radio luminosities are up to $10^{12}\,L_{\odot}$. The spectral energy distribution of a quasar is shown in Fig. 2.2. The optical and UV regions of the spectrum tipically show strong broad emission lines from a variety of ions, whose ionization requires very high energy photons, most likely the soft X-rays emitted by the nucleus. The brightest lines are those of hydrogen, helium, carbon, magnesium, iron and oxygen. More than 200.000 quasars are known today, mostly from the Sloan Digital Survey. The observed spectra show redshifts in the range 0.056-7.085. The brightest quasar in the sky is 3C 273, with an absolute magnitude of -26.7 mag [132] at redshift 0.158. A multiply imaged quasar is a quasar whose light, according to the effect predicted by Einstein's general theory of relativity ([44],[45]), has been gravitationally bent by a foreground mass along the line of sight, giving rise to multiple differently magnified images of the same source and resulting in what is referred to as a gravitational lens system. The first gravitational lens Q0957+561 was discovered in 1979 and was a double-imaged quasar [159].

2.2 GRAVITATIONAL LENSING

Gravitational lensing generally indicates the bending of light rays from a background light source by the gravitational field of a foreground mass, such as a star, a galaxy or a galaxy cluster. The lensing effect can produce multiple images of the background source, which show different amplifications of the initial flux, called magnifications, and distortions of the original shape.
Scientists started to think about light deflection more than 300 years ago. In his treatise published in 1704 [2], Newton first argued that light particles were affected by gravity as ordinary matter. In the beginning of the 19th century, Soldner wrote an article where he investigated the possibility that a light ray could be attracted by the gravitational field of a body and derived the deflection angle for a light ray passing by the solar limb. In 1911 Einstein had also thought about light deflection and published the same value of the deflection angle obtained by Soldner, which was half of the correct value. Only with further development of the general theory of relativity the phenomenon was correctly described by Einstein in 1915 [44]. In 1919 Eddington measured the deflection angle

of a light ray passing by the solar limb during a total solar eclipse and proved the recent prediction by Einstein to be correct [38]. Some years later, Einstein computed in a paper [45] the magnifications of the two images of a background star lensed by a foreground star that transits close to the line of sight towards it. Fritz Zwicky ([182], [181]) introduced the idea that galaxies could work as gravitational lenses as well, providing a further test for the theory of general relativity and a means of estimating galactic masses. The images of a gravitationally lensed quasar have light travel time differences between them, so that any intrinsic variability of the quasar appears at different times in the light curves of the multiple images. Refsdal [121] first showed that time delays between the multiply lensed images of variable sources, such as supernovae, provide a means of determining the Hubble constant H_0, given a mass model for the lensing galaxy. Apart from measuring the Hubble constant [74], gravitational lensing also provides a means of estimating the surface mass density of intermediate-redshift lensing galaxies [71] and investigating the composition and structure of the galactic dark matter halos ([57], [130],[30]). After [159] published the discovery of the first double lensed quasar Q 0957+561, it was proposed that foreground stars close to the line of sight could gravitationally affect the fluxes of the multiple images [20]. Another area of application of gravitational lensing referred to as *quasar microlensing* was born. The term microlensing was first introduced by Paczynski [109], who meant to describe both the action of stars in distant galaxies on quasar images and of stars in the Milky Way on far away stars of the Galactic bulge or the Magellanic Clouds [68]. Quasar microlensing is caused by compact objects along the line of sight towards quasars, which are multiply imaged by foreground lensing galaxies ([20], [57], [180]). The perturbative effect on the light curves of the quasar images consists of brightness variations up to a magnitude over timescales of weeks to years. Multiply imaged quasars are particularly suitable for isolating microlensing variations, which rise in an uncorrelated fashion between the images, in contrast to the correlated intrinsic quasar fluctuations. Quasar microlensing can thus be used as a method to study the structure of quasars, since the amplification of the microlensing signal depends on the size of the quasar emitting region. It also works as a probe for the existence of compact objects between the observer and the quasar and for their mass distribution.

2.2.1 Basic theory of gravitational lensing

In principle all the matter, distributed between the source and the observer, affects the propagation of the behind emitted light. Nevertheless, in many cases, it is a good approximation to assume that the light deflection happens on a plane containing all the lens mass, at a definite distance between the observer and the lens. The basic theory of gravitational lensing will be introduced in this *thin lens approximation* (see [134]).

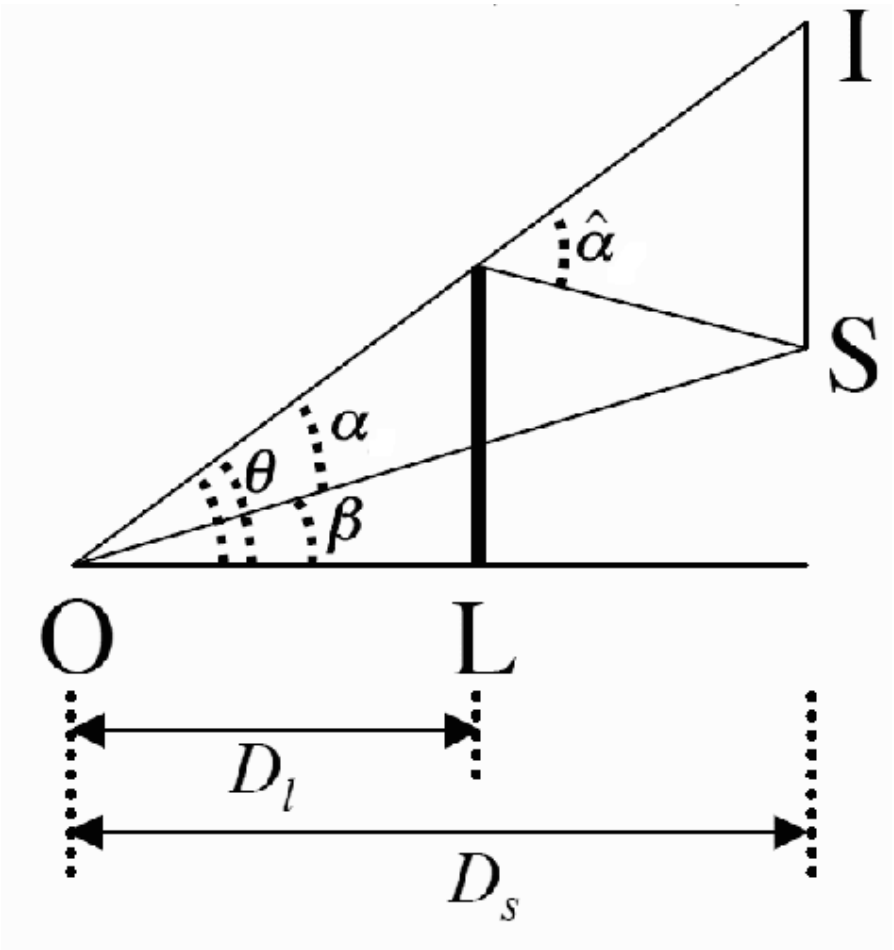

Figure 2.3: The lens L, at a distance D_l from the observer O, deflects light from a source S, at a distance D_s, by the deflection angle $\hat{\alpha}$. The angular positions of the image and source are θ and β, respectively. Adapted from Gaudi (2010).

The lens equation for a point-like source/point-like lens system. Figure 2.3 shows the configuration of the simplest lensing system. An observer placed in O receives the light rays emitted from a point source S at distance D_s, which are deflected by a point-like lens L, at a distance D_l, by an angle $\hat{\alpha}$. In the thin lens approximation, the length over which the lens mass is distributed along the line of sight is $<< D_s$, D_l, and $D_s - D_l$. Moreover, the relative velocities of the source, image and observer are much smaller than the speed of light $v << c$.

We define β as the angular separation between the lens and the source in case of no lensing and θ as the separation angle between the generic source image and the lens. The relation existing between β and θ is called *lens equation* and is given by $\beta = \theta - \alpha$, where

α is defined as in figure. By making use of the small angle approximation, $\hat{\alpha}(D_s - D_l) = \alpha D_s$, the lens equation assumes the shape:

$$\beta = \theta - \frac{4GM}{c^2\theta}\frac{D_s - D_l}{D_s D_l}, \tag{2.1}$$

where the following result for the deflection angle $\hat{\alpha}$ in the case of a point source and a point lens of mass M, valid as long as the bending is small,

$$\hat{\alpha} = \frac{4GM}{c^2 D_l \theta} \tag{2.2}$$

has been used [44]. If the lens and the source are perfectly aligned ($\beta = 0$), the image of the source is a ring with angular radius given by the *Einstein radius*

$$\theta_E = \sqrt{\frac{4GM}{c^2}\frac{D_s - D_l}{D_s D_l}}. \tag{2.3}$$

By defining the variables $u = \beta/\theta_E$ and $y = \theta/\theta_E$, the lens equation takes the following form:

$$u = y - y^{-1}. \tag{2.4}$$

In case of imperfect alignment, the quadratic lens equation yields two images, at angular positions

$$y_\pm = \frac{1}{2}(\pm\sqrt{u^2+4} + u). \tag{2.5}$$

The positive solution is always placed outside of the Einstein ring, whereas the negative one is always inside on the opposite side of the lens (see Fig. 2.4). When the angular separation between the lens and the source reaches its minimum value, the separation between the images is $\sim 2\theta_E$. Since the images are distorted and gravitational lensing conserves the surface brightness of the source, the flux of each image is either larger or smaller than the flux of the unlensed source. In other words, the images are magnified or demagnified. Since the surface brigthness is conserved, the magnification of each image is given by the ratio between the areas covered by the image and the source.

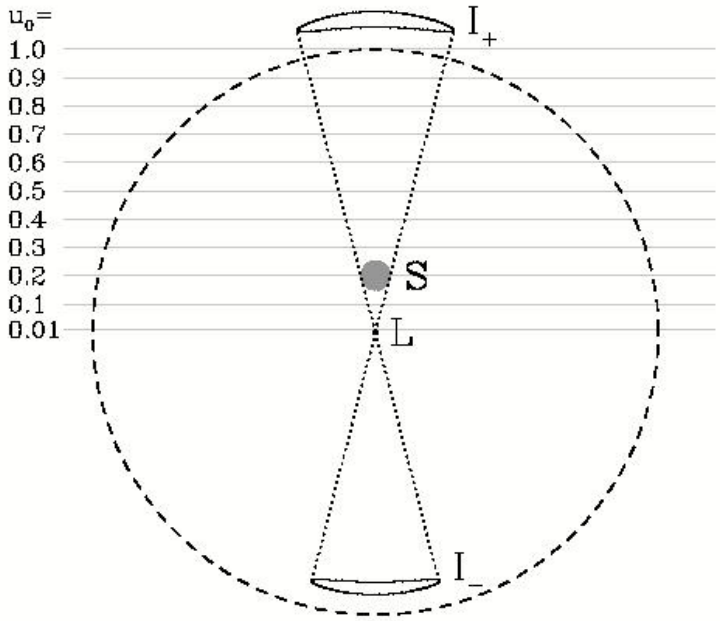

Figure 2.4: Point-mass microlensing for a source S located at an angular separation u=0.2 (Einstein radius units) from the lens L. Two images are created: I_+ outside the Einstein ring and I_- inside the Einstein ring. Adapted from [53].

Figure 2.4 shows the images of a source at an angular separation from the lens of $u = 0.2$. The images are elongated tangentially by $y_\pm/u$ and compressed radially by $dy_\pm/du$. These considerations allow to compute the magnifications as follows:

$$A_\pm = \left|\frac{y_\pm}{u}\frac{dy_\pm}{du}\right| = \frac{1}{2}\left[\frac{u^2+2}{u\sqrt{u^2+4}} \pm 1\right]. \tag{2.6}$$

The total magnification is obtained by summing up the two magnifications above:

$$A = \frac{u^2+2}{u\sqrt{u^2+4}}. \tag{2.7}$$

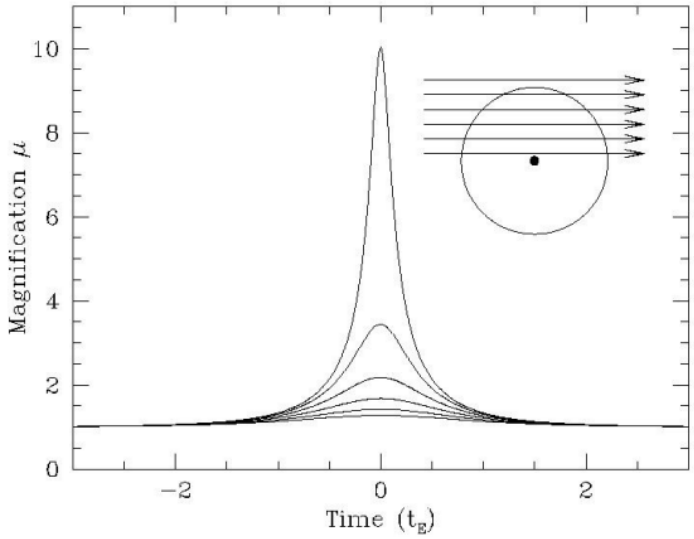

Figure 2.5: Magnification of a point-like source by a point-like lens for different impact parameters as a function of time. Adapted from [160].

Since the lens, the source and the observer are in relative motion, the angular separation between the lens and the source is a function of time and the magnification of the source is a function of time as well. The time scale of the flux variation t_E is given by the time that the source takes to cross the Einstein radius of the lens. The magnification of a point source by a point lens for different impact parameters (the minimum angular separation from the lens) is shown in Figure 2.5 as a function of time. Event characterized by very small impact parameters, smaller than ~ 0.1 Einstein radii, are referred to as high-magnification events.

General expression for the lens equation and the image magnification. It can be showed that, for any generic lensing configuration, the deflection angle is the gradient of an effective lensing potential ψ [136]. This allows to rewrite the lens equation as

$$(\boldsymbol{\theta} - \boldsymbol{\beta}) - \nabla_{\theta}\psi = 0 \tag{2.8}$$

where boldface indicates 2-dimensional vectors. The number of the produced images depends on the shape of the lensing potential. If the lens equation is non-linear, multiple images of the source will appear. An additional form in which the lens equation can be written is the following:

$$\nabla_\theta(\frac{1}{2}(\boldsymbol{\theta}-\boldsymbol{\beta})^2-\psi)=0. \tag{2.9}$$

From the above equation it can be seen that the lensed images of a source appear at angular positions $\boldsymbol{\theta}$ that correspond to extrema of the expression in parentheses. This expression is also found in the time delay function for the lensed images, which is a function of the angular positions $\boldsymbol{\theta}$ and $\boldsymbol{\beta}$, the potential ψ and the distances involved in the lensing configuration:

$$\tau(\boldsymbol{\theta},\boldsymbol{\beta})=\frac{1+z_L}{c}\frac{D_l D_s}{D_s-D_l}(\frac{1}{2}(\boldsymbol{\theta}-\boldsymbol{\beta})^2-\psi). \tag{2.10}$$

The previous equation shows that the images produced in a generic lensing configuration arise at extrema of the light travel time, which is a re-statement of the principle of Fermat's, first introduced in classical optics.

It can be shown that, given a lensing system with the source at angular position $\boldsymbol{\beta}$, the magnification of the corresponding images, which arise at angular positions $\boldsymbol{\theta}$, is given by the determinant of the inverse matrix of the Jacobian J of the lens mapping:

$$A=det\left(J^{-1}\right), \tag{2.11}$$

with

$$J=\frac{\delta\beta}{\delta\theta}=\delta_{i,j}-\psi_{,ij}, \tag{2.12}$$

where the indices on ψ define its second partial derivatives with respect to the components of $\boldsymbol{\theta}$. The total magnification is defined as the sum of the magnifications of the individual images. There are some source positions at which the magnification A is formally infinite. The set of all such source positions define closed curves called *caustics*. The corresponding set of image positions defines the closed curves called *critical curves*. Caustics consist of multiple concave segments, referred to as folds, joining at points called cusps.

Lens equation with compact objects along the line of sight. In this paragraph an additional way of writing the Jacobian of the lens mapping is introduced. This will be used to write the lens equation in the particular case of the existence of compact object moving in a foreground lensing galaxy.

The Jacobian matrix can be decomposed as a sum of two terms, a diagonal and a traceless matrix. By defining $k=\frac{1}{2}(\psi_{,11}+\psi_{,22})$, $\gamma cos2\phi=\frac{1}{2}(\psi_{,11}-\psi_{,22})$ and $\gamma sin2\phi=\psi_{,12}=\psi_{,21}$, the matrix becomes

$$\begin{bmatrix} 1-k & 0 \\ 0 & 1-k \end{bmatrix} - \gamma \begin{bmatrix} cos2\phi & sin2\phi \\ sin2\phi & -cos2\phi \end{bmatrix}. \tag{2.13}$$

The convergence k, which corresponds to a dimensionless surface density on the lens plane and measures the optical depth of a lens system, produces an isotropic broadening or shrinking of the section of a bundle of light rays and the terms γ and ϕ, called shear and shear orientation respectively, its distortion. In case of a circular source, the action of the term k alone is to map it into a larger or smaller circle, the action of the term γ alone is instead to distort the circle into an ellipse with axis ratio equal to $\frac{1+\gamma}{1-\gamma}$ and an axis orientation defined by ϕ.

The Einstein radius θ_E sets a reference for the angular separation between the images of a lens configuration. The typical Einstein radius correponding to a galaxy lens of mass M is of the order of $\theta_E \sim$ arcsec, while for stars in the lensing galaxy the Einstein scale is of the order of a few 10^{-6} arcsec. This means that it is possible to resolve the images of a background source produced by an intervening lensing galaxy (macrolensing), but not those produced by lensing stars in a galaxy (microlensing). The images arising in the case of a source lensed by a galaxy are magnified and distorted. The compact objects in the galaxy further lens the source images. The local behaviour of the lens mapping in the neighborhoods of an angular position θ_0, described by the Jacobian matrix, allows to linearize the part of lens equation containing the effects of the intervening galaxy. The effects of the individual compact objects can be simply summed up. The lens equation takes the following form [110]

$$\boldsymbol{\beta} = \begin{bmatrix} 1-k_{gal}-\gamma & 0 \\ 0 & 1-k_{gal}+\gamma \end{bmatrix} \boldsymbol{\theta} - \frac{D_s - D_l}{D_s D_l} \frac{4G}{c^2} \sum \frac{m_i(\boldsymbol{\theta}-\boldsymbol{\theta_i})}{(|\boldsymbol{\theta}-\boldsymbol{\theta_i}|)^2}. \tag{2.14}$$

2.3 The special case of Quasar Microlensing

One in every 500 quasars is seen through a lensing galaxy and about 100 multiply imaged quasars have been observed so far, most of them made up of two or four images [114]. The typical mass of a macrolensing galaxy in a quasar lens is of the order of $10^{12} M_{\odot}$. Quasar microlensing arises when compact objects, with masses in the range $10^{-6} - 10^{3}\ M\odot$, additionally lens the quasar images and define a very interesting lensing regime, through which it is possible to address several open questions, such as those regarding the size and brightness profile of quasar disks and the distribution of compact objects along the line of sight to the quasars. The category of compact lenses includes planets, brown dwarfs, stars, black holes, gas clouds and star clusters, most of the times found in a foreground galaxy, but in principle also in the intergalactic medium. The combined effect of several microlenses does not combine linearly, instead it determines a very complicated magnification pattern in the quasar plane, made of overlapping

caustic curves. An example of such a magnification distribution produced by stars in a lensing galaxy, is shown in Figure 2.6, where the different colors indicate different magnification levels produced by the resulting caustic structure [134]. The light curves of a quasar moving along the dashed tracks shown in Figure 2.6 are displayed in Figure 2.7. If the quasar has a small size compared to the space between caustics, the light curves will show high magnification peaks, because the passage through a caustic line is fully resolved. On the other hand, a larger source will cause the peaks to be washed out and the resulting (dashed in figure) light curve will be smoother. The typical angular scale for microlensing due to stars in a lensing galaxy, of the order of 10^{-6} arcsec, is equivalent to a length scale of $\sim 10^{16}$ cm in the quasar plane, assuming the lens at redshift $z_l = 0.5$ and the source at $z_s = 2$. In other words, under the assumption that the quasar lies at a distance of ~ 1 Gpc from us, the spatial scale on the sky which subtends an angular scale of 10^{-6} arcsec is $\delta s = 10^{-6}\, arcsec \times 1\, Gpc = 1.5 \times 10^{16}\, cm$. The images produced at such a small angular separation cannot be resolved, but the relative motion between the observer, the lenses and the source determines a variation of the total magnification as a function of time and a change of the center of light position over time. The flux fluctuations are expected on time scales comparable to the crossing time t_{cross}, which is defined as the time a source of radius R_{source} takes to cross a caustic portion (a place of formally infinite magnification for a point source), determining a large flux variation. Taking into account a source size of the order of 10^{15} cm and a typical relative transverse quasar velocity of 600 km/s, the crossing time t_{cross}, in other words the flux variability duration scale, is of the order of four months. This time scale is much shorter than the time t_E it takes the source to cross the whole Einstein ring of a typical compact lens, which is of the order of ~ 10 years and sets the duration scale of the flux perturbation produced by the gravity of any single lens [134].
Microlensing acting on the images of a multiply imaged quasar is expected to happen at any given time, since a number of microlenses is constantly moving in front of each quasar image within galactic regions characterized by convergence k of the order of unity.

From an observational point of view, any variability which appears in all quasar images, with a time lag matching the different path lengths, is to be considered intrinsic to the quasar. Once the time delays of a lens system are measured, the light curves can be shifted by the time delays and by the different magnifications due to the lensing galaxy, and the remaining fluctuations can be attributed to microlensing. Many ground- and space-based observatories have contributed the coverage in wavelength and time for many multiply imaged quasars. The best sampling has been obtained in the optical bands. There are also several photometric and spectroscopic monitoring campaigns at other wavelengths, from the radio to the X-ray regime ([42], [43], [73], [153]).
Quasar microlensing has been used as a probe to investigate the size and brightness

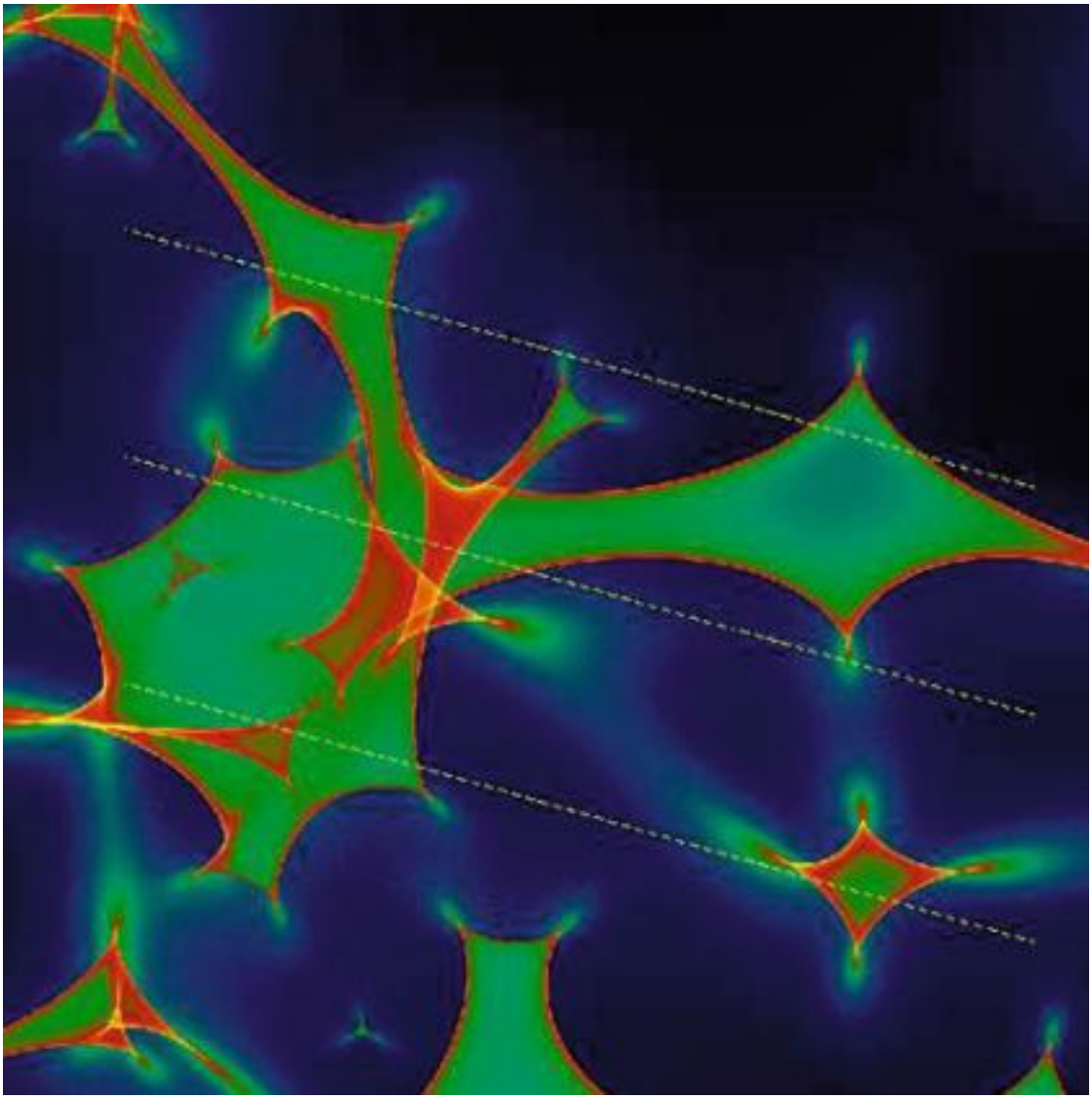

Figure 2.6: Caustic magnification pattern in the quasar plane produced by lensing stars in the macro-lens galaxy. The dashed lines crossing the caustics represent three source trajectories. Adapted from [134].

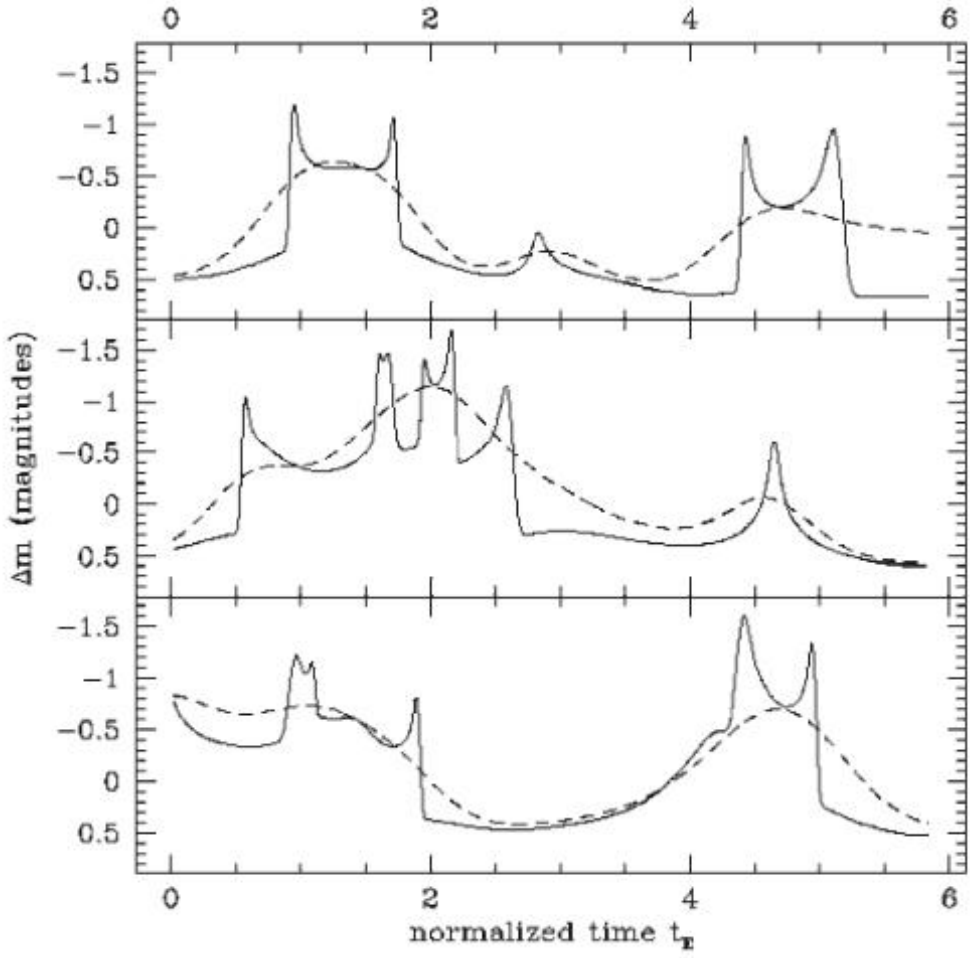

Figure 2.7: Light curves from a source crossing the caustic pattern in Figure 2.6. The first panel corresponds to the upper trajectory, the second to the middle trajectory, the third to the bottom one. Two sets of light curves are displayed. The black line corresponds to a small source, the dashed one to a source 10 times larger. The resulting light curves are different. Larger sources wash out the microlensing signal as they cross the caustics, as a consequence of their finite size. Adapted from [134].

profile of multiply imaged quasars. This is based on the correlation between the microlensing magnification of a quasar image and the quasar emitting region size, which depends on the observed passband [138]. Several authors have looked into the possibility of recovering the brightness profile of a quasar ([7], [58], [59], [179], [118], [104]) by observing caustic crossing events in many bands. Several studies have addressed the question whether the microlensing effect on broad emission lines could be used to resolve the broad line emission regions ([137],[87],[3],[4],[84], [86],[126]).
[166],[85] and [152] have considered the variation of the quasar positions in multiply lensed quasars at the caustic crossings, when a bright image pair appears or disappears. The resulting position displacement is estimated to be of the order of 100 microarcsec, observable with high resolution interferometers. Astrometric microlensing, as this technique is referred to, might help estimate the masses of the compact object from a variation in the quasar center of light position. Several works ([165], [122], [24], [23]) were also able to exclude certain mass values of the compact objects lenses making up the halo of the lensing galaxy in the particular case of the multiple quasar Q 0957+561. In all these studies, the absence of microlensing fluctuations with amplitudes larger than ~ 0.1 mag over certain periods of time allowed to exclude that the galaxy halo dark matter consists of compact objects with masses $<< M\odot$. [52] was, on the other hand, able to exclude that the galaxy halo in the galaxy of the above lensing system is made up of objects with masses $10^6 M\odot$ (see also [162]).
Flux ratio anomalies are found in lensed quasars. This means that the flux ratios observed between the produced images of a multiply imaged quasar do not match the predictions of a simple macrolensing galaxy model. Two different scenarios might provide an explanation to the flux-anomaly issue. The first argues that unmodeled substructure nearby the lensing galaxy can change the magnifications of the lensed images [99]. This effect would not depend on the wavelength. On the other hand, [130] suggests that microlensing by compact objects can perturb the observed flux ratios, also demagnifying the flux from images emerging in saddlepoint extrema (whose observed flux is often demagnified compared to the predicted one) and causing an effect both wavelength- and time- dependent. In the case microlensing alone is at work, since quasar disks are predicted to emit radiation peaked at longer wavelengths at larger radii [138], it is expected to observe weaker microlensing signals and flux ratios more similar to the macro-model values when approaching the long wavelength regime of the electromagnetic spectrum. The quadruple quasar HE 0435-1223 [168] shows indeed emission line ratios between the images that match predictions better than the continuum flux ratios, showing that the lines are emitted from regions at larger distances from the central engine than those emitting the continuum.

3

Overview of the quasars studied in this work

3.1 WFI J2033-4723

WFI 2033-4723 is a quadruply imaged quasar, see Fig. 4.4, which was discovered by [102]; the four images, B,A1,A2,C are at redshift $z_Q = 1.66$ and have a maximum angular separation of 2.53″. A Hubble Space Telescope (HST) image of the quasar, adapted from [158], is shown in Fig. 3.1. [102] defined the system as an interesting target for microlensing studies, since the system flux ratio between the images C and B varied by 0.23 mag from the bandpass u to i, while the emission line ratios of the same images agreed much better with the macromodel predictions than the ratios corresponding to the continuum and broadband filters. The emission line ratios suggest that the anomalous flux ratio between images C and B in the blue is caused primarily by microlensing induced perturbations rather than unmodeled substructure in the lensing potential. [41] found that the lens galaxy spectrum is consistent with an elliptical or lenticular galaxy template at redshift $z_L = 0.661 \pm 0.001$. The lensing galaxy is a member of a group with at least 6 galaxies, whose distance from the lens is at most 20″ [102]. [158] determined the time delays between the quasar components to be $\Delta t_{B-C} = 62.6^{+4.1}_{-2.3}$ days and $\Delta t_{B-A} = 35.5 \pm 1.4$ days between C and B, and A and B, respectively. The label A indicates the combination of images A1 and A2. Since A1 and A2 are predicted to have a negligible relative time delay, they are treated as a blend by [158].

3.2 HE 0047-1756

The quasar HE 0047-1756, see Fig. 4.5, was discovered in the Hamburg quasar survey (ESO) at the Magellan 6.5 m telescopes on Cerro Las Campanas, Chile ([170], [123], [169],[172]). This survey used spectra to search for quasars over the entire southern sky. An HST image of the double quasar, adapted from [21], is shown in Fig. 3.2. [172] found that the quasar was in fact a lensed system, with identical redshifts of the

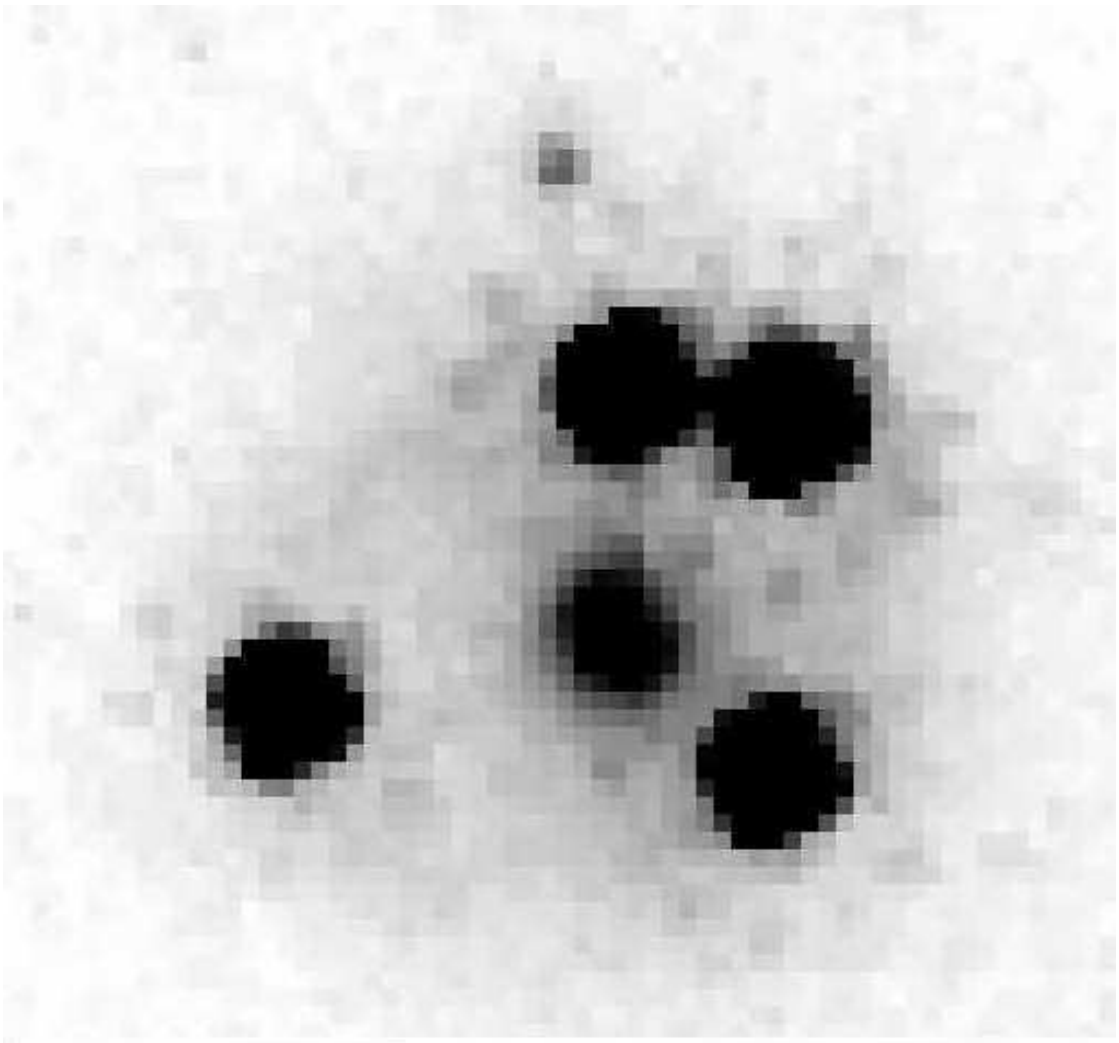

Figure 3.1: HST NICMOS2 image of quasar WFI 2033-4723, taken in the F160W band. This image has a total exposure time of 46 minutes. North is up and East to the left. The field of view is of 4 arcsec.

two images, similar emission line profiles, with a galaxy located between the two components, and a partial Near Infrared (NIR) Einstein ring. The two observable images were separated by $\Delta\theta = 1.44''$ and the quasar redshift was estimated at $z_Q = 1.67$. They reported a flux ratio for the two components of roughly 3.5 to 1 that slightly depended on wavelength. The emission line ratio differed from that in the continuum. They attributed these small differences to microlensing. However, spectral variability and time delay effects could not be ruled out. The lensing galaxy, discovered by [172] using the Magellan 6.5 m telescopes, is at redshift $z_L = 0.408$ according to [107] (see also [41]). The lens galaxy spectrum matched well with an elliptical galaxy template ([107], [41]). The time delay has not been measured yet. The time delay is a strong increasing function of the lensing galaxy redshift and is predicted to be of 32.1 days at $z_{lens} = 0.6$ [172].

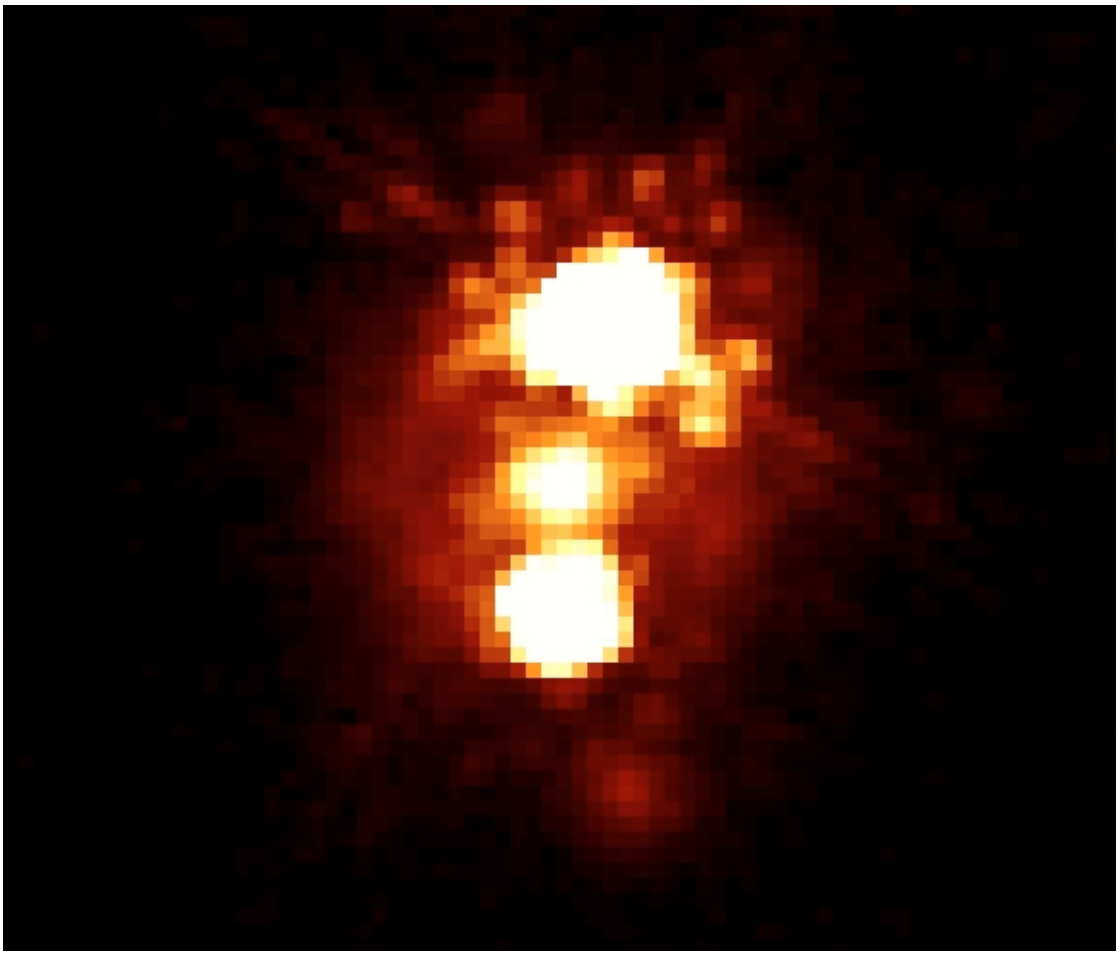

Figure 3.2: HST NICMOS2 image of quasar HE 0047-1756.

3.3 Q 2237+0305: Huchra's lens

Huchra's lens Q 2237+0305 was discovered by [65], and is also known as the Einstein Cross. It is one of the most impressive examples of the gravitational lensing phenomenon. An HST image of this system in the V band is shown in Fig. 3.3. The average distance of the images from the system center is about 0.9″. The four images were resolved by [177] and [135] and are at redshift $z = 1.695$. They appear in a cross-like pattern around the nucleus of a barred Sab galaxy, which is at redshift $z = 0.039$. This special geometrical configuration leads to small time delays between the lensed images, which are estimated to be of the order of a day ([135], [127], [163], [133]). The light from the four lensed images travels through the densely populated inner region of the lensing galaxy. This aspect makes of the Einsten Cross an optimal system to study microlensing, because of the large number of microlensing stars passing through the inner disk of the galaxy [69]. Another peculiarity is the unusually short distance between the lensing galaxy and the observer, which leads to microlensing events with durations from a few week to a few months. The duration of the typical microlensing event and the short time delays imply that the uncorrelated microlensing perturbations can be easily recognized among the almost simultaneous intrinsic brightness variations. The blending of the four lensed images and the bright deflecting galaxy make it difficult to obtain accurate photometry of the four lensed components. The system has been widely investigated since 1987, when the *g*,*r* and *i* Gunn magnitudes of the four lensed images were first published by [177]. The first light curves of the four lensed images were built in 1991, by [25], which brought together all the existent images. Their light curves extend from September 1986 over December 1989 and include the first observed microlensing brightness variation in 1988 reported by [66]. In 1994 [64] built new light curves by merging the data from [25], [27], [119], [127] and [64]. The first 5-year multicolor monitoring program of Q 2237+0305 was started in 1990 at the Nordic Optical Telescope [108], and allowed for the construction of a set of light curves that covered nine years of observations. An impressive long-term monitoring program was started by the Optical Gravitational Lensing Experiment (OGLE) in 1997 and is still going on at the 1.3 m Warsaw telescope in Las Campanas (Chile), revealing continuous flux variations in the light curves, up to a factor of two over few months, as shown in Figure 3.4. The first OGLE data have been presented by [173] and [174]. In 2002 the Gravitational Lensing International Time Project (GLITP) published data in the V and R bands which extended over a 4-month period between 1999 and 2000 ([10], [101]). The color indices of the four lensed images have also been studied in order to unveil any color changes since the first color measurements by [177]. The Maidanak monitoring campaign [155], whose set of light curves in the R band is shown in Fig. 3.5, and [19] found that the B component had indeed become the bluest in the system, differing from the observations by [177]. Other attempts to determining colors and colors changes were made by [36]

and [37], which found significant color variations, and by [156]. A great amount of observations in photometric bands different than the optical range have also been collected, at 20 cm and 3.6 cm [47], in the near and mid infrared ([105], [6]) and at the emission lines wavelenghts ([49], [119], [31], [87], [129], [42]). Moderate microlensing perturbations have been found in these spectral bands, which indicates that the infrared, radio and emission lines regions are larger than the optical continuum emission region. Long-term spectrophotometric monitoring has been conducted at the Very Large Telescope over three years from October 2004 to December 2007 to constrain the energy profile of the quasar ([40],[42], [141]). These data showed that the continuum and the broad line region are microlensed. Observations in the UV bands with the HST [15] and in the X-ray regime with the Chandra X-ray Observatory [29] respectively provided accurate relative astrometry of the components and the estimate of the time delay between the A and B components of 2.7 hours. Several attempts to determine the time delays from ground based observations in the visual wavelengths have also been published. [154] provided the first direct measurements of time delays from optical ground-based data, namely $\tau_{AB} \approx -6$, $\tau_{CA} \approx 35$ and $\tau_{DA} \approx 2$ hours. [77], on the other hand, considered the possibility of measuring the time delays between the components of the Einstein Cross and showed the impossibility of unambiguously determining the time delays between the lensed components of Q 2237+0305 by making use of ground-based optical data taken with telescopes of ≈ 1.5 m.
[164],[175],[178], [72], [11] and [98] showed, by comparing observed light curves and simulations, that the continuum emission region of the quasar is of the order of $\sim 10^{15}$ cm. Thanks to a spectrophotometric monitoring of the quasar over a long period of time, [40] could show that the accretion disk of Q 2237+0305 is consistent with a Shakura-Sunyaev accretion disk [138]. In particular, they showed that the microlensing signal in several bands becomes stronger moving towards shorter wavelengths, an effect originally predicted by [161].

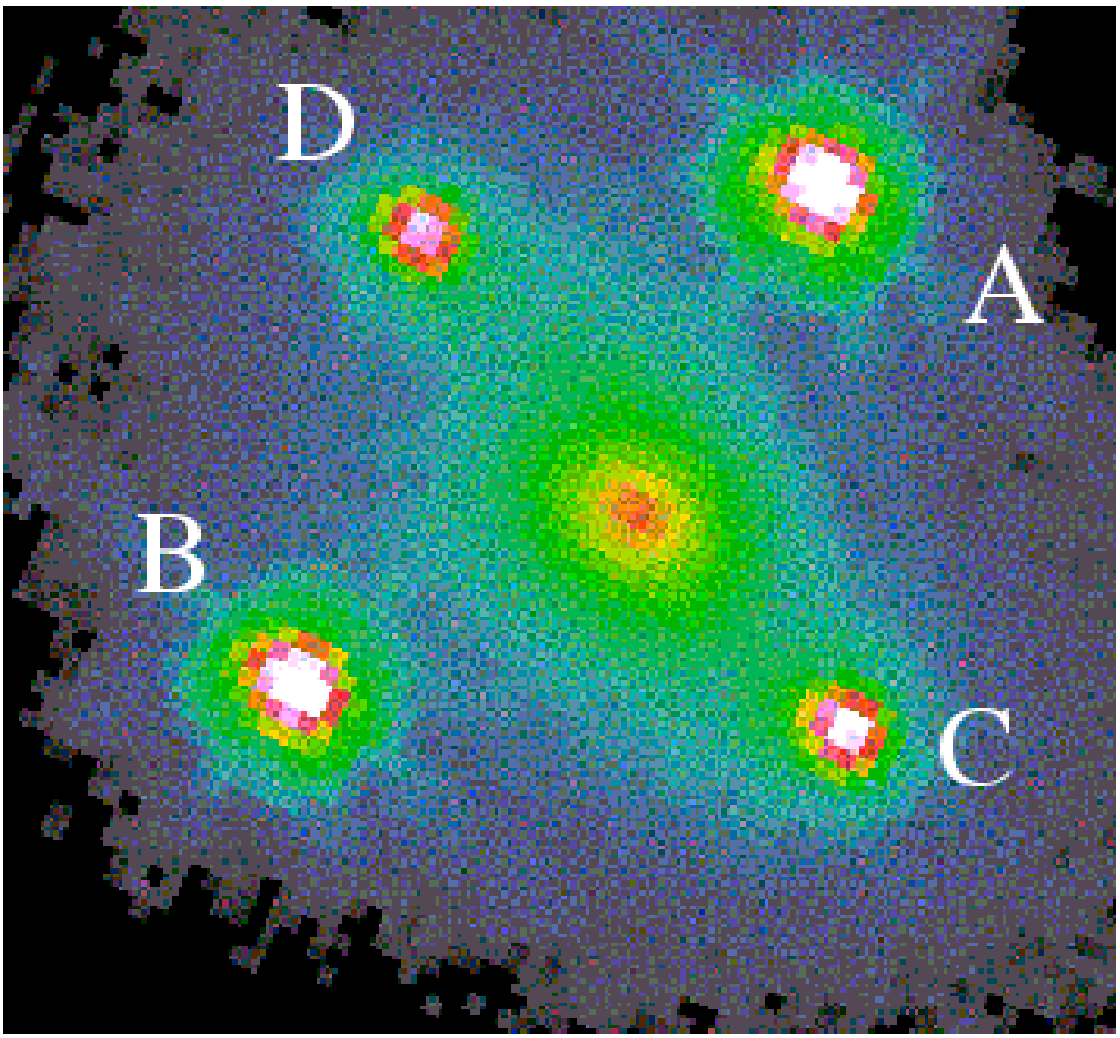

Figure 3.3: The gravitational lens Q 2237+0305 observed with the HST in the V-band. Adapted from R. W. Schmidt (2000).

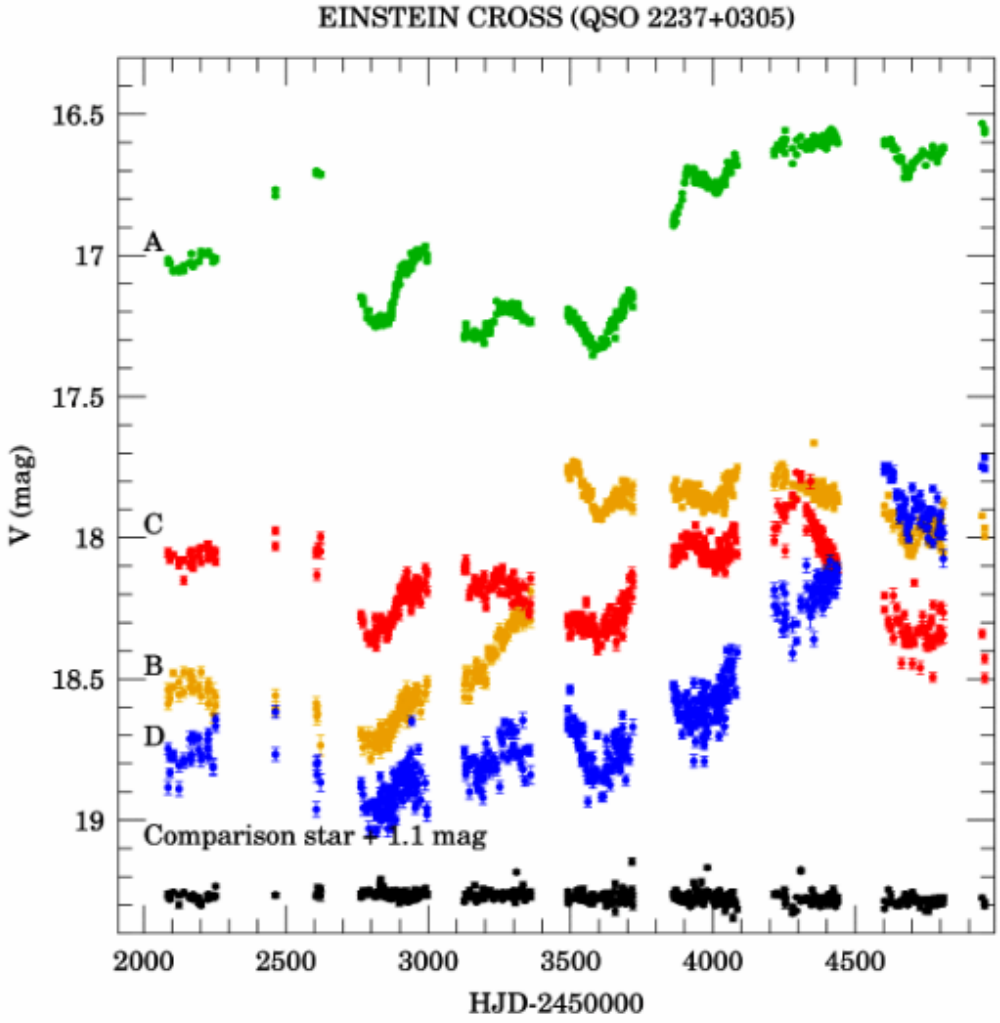

Figure 3.4: Light curves for the gravitational system Q 2237+0305 observed by the OGLE-III (http://ogle.astrouw.edu.pl/) monitoring campaign in the V band.

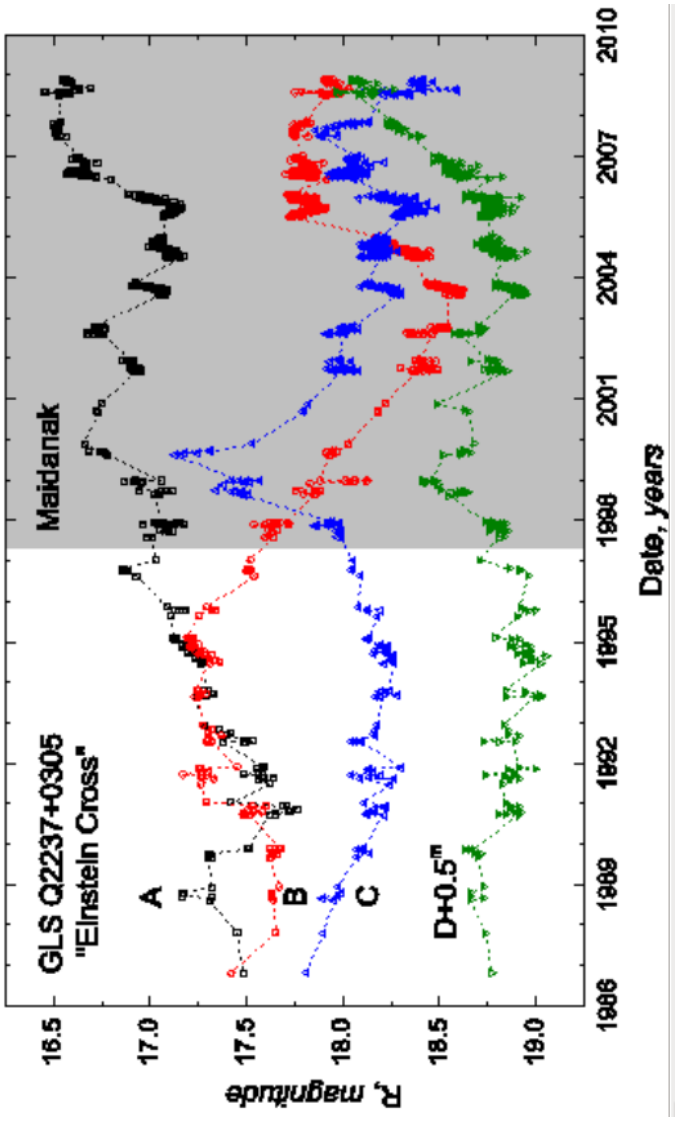

Figure 3.5: Light curves for the gravitational system Q 2237+0305 observed by the MAIDANAK monitoring campaign from 1997 in the R band. Light curves prior to 1997 have been obtained by joining up already existing observations. From http://www.astron.kharkov.ua/dip/maindep.htm.

4

The MiNDSTEp collaboration and data acquisition

4.1 MiNDSTEp: Objectives and first results

The MiNDSTEp consortium (Microlensing network for the detection of small terrestrial exoplanets) is the largest European/Eurasian collaboration which monitors ongoing gravitational microlensing events. It aims at the investigation of the nature of the population of planets down to Earth mass in the Milky Way. The telescope network, including in 2008 only the Danish 1.5 m telescope at ESO LA Silla (Chile), has been expanded to involve the two MONET 1.2 m telescopes at McDonald Observatory (Texas, USA) and the South African Astronomical Observatory. MiNDSTEp relies on microlensing surveys as OGLE and MOA (Microlensing Observations in Astrophysics, New Zealand) and realizes by itself the further steps of follow up and monitoring. Quasar microlensing is one of the other projects, other than exoplanetary microlensing, carried out by MiNDSTEp. Five different lensed quasar were observed by the collaboration at the Danish 1.5 m telescope.
The Danish 1.54 m telescope has been at La Silla since 1979, see Fig. 4.1. It is now equipped with the Danish Faint Object Spectrograph and Camera (DFOSC). The telescope has allowed several first discoveries. It has also produced many impressive astronomical images. Some important facts regarding the Danish telescope are summarized in Fig. 4.2. The observations of quasars WFI 2033-4723, HE 0047-1756 and Q 2237+0305, from 2008 to 2012, are matter of this thesis; the observations of HE 0435-1223 and UM673 have been published in two papers by [125] and [124]. In the first paper, they presented the *VRi* photometric observations of the quadruply imaged quasar HE 0435-1223, with the aim to study magnitudes and colors of each lensed component as a function of time. The target was monitored during the seasons 2008 and 2009 and analyzed with two different techniques, differential image photometry and Point Spread Function (PSF) fitting. They found a significant decrease in flux by 0.2-0.4 mag of the lensed components in all photometric bands, together with a significant increase

of $\approx 0.05 - 0.015$ mag of the colour indices $V - R$ and $R - i$ between the two seasons. They concluded by arguing that the flux and colour variations are very likely caused by intrinsic variations of the quasar between the observing seasons, with microlensing affecting probably the brightest A component, which showed the largest shift in color. The flux and color variations of the doubly lensed quasar UM673 as a function of time are analyzed in the second paper. The observations were carried out during four seasons from 2008 to 2011 in the photometric bands *VRi*. Data were reduced by making use of the PSF fitting alongside with aperture photometry. The brightest lensed quasar component A showed some flux decrease between 2008 and 2009 in all bands of the order of ≈ 0.1 mag, followed by an increase of the order of ≈ 0.1 mag during the following seasons. The colour index variations found between the seasons were smaller than those found by previous studies.

Figure 4.1: The Milky Way and the Magellanic Clouds above the Danish telescope dome, on the right in the picture. From http://www.eso.org/public/images/.

Name:	Danish 1.54-metre telescope
Site:	La Silla
Altitude:	2375 m
Enclosure:	Classical dome
Type:	Spectrographic telescope
Optical design:	Ritchey-Chrétien Reflector
Diameter. Primary M1:	1.54 m
Material. Primary M1:	Cervit
Diameter. Secondary M2:	0.61 m
Material. Secondary M2:	Cervit
Mount:	Off-axis equatorial mount
First Light date:	20 November 1978

Figure 4.2: Table summarizing the main properties of the Danish telescope. Adapted from (http://www.eso.org/public/.)

4.2 Data acquisition

The observations of the lensed quasars WFI 2033-4723, HE 0047-1756 and Q 2237 +0305 were obtained in the *V* and *R* bands with the 1.54 m Danish telescope at ESO/La Silla, Chile, by the MiNDSTEp (Microlensing network for the detection of small terrestrial exoplanets, [35]) quasar monitoring campaign. The observations were collected during five observing seasons, from 2008 to 2012. The quasars were observed within the following temporal intervals: from June 5 to October 4 2008, from June 19 to September 18 2009, from May 9 to August 21 2010, from June 11 to August 31 2011 and from July 16 to September 16 2012. During these periods we observed the quasars every two days, weather permitting, in the *V* and *R* filters of the Bessel system. The quasars were observed on average three times per night. WFI 2033-4723 was observed with an exposure time of 180 s in *V* and *R*, except for a small number of images, with longer exposure times of 300 s and 600 s, at the start of 2008. Exposure times for HE 0047-1756 varied from 180 s in both filters during the first two seasons to 240 s in *V* and 210 s in *R* during the last three years. A few images in both bands at the start of the first season were taken with exposure times of 300 s and 600 s. Exposure times for Q 2237+0305, were of 180 s in both filters for most part of the observing campaign. A few images in both bands at the start of the first season were taken with exposure times of 300 s and 600 s and in June 2009 with exposure times of 200 s.

The median seeing of the observations was $\approx 1.3''$, taking into account both filters and all data. The observations were made with the DFOSC imager, shown in Fig. 4.3, with a pixel scale of $0.39''$. The full field of view (FOV) was 13.7 arcmin $\times$ 13.7 arcmin. A section of the FOV centred on the quasars is shown in Figs. 4.4, 4.5 and 4.6.

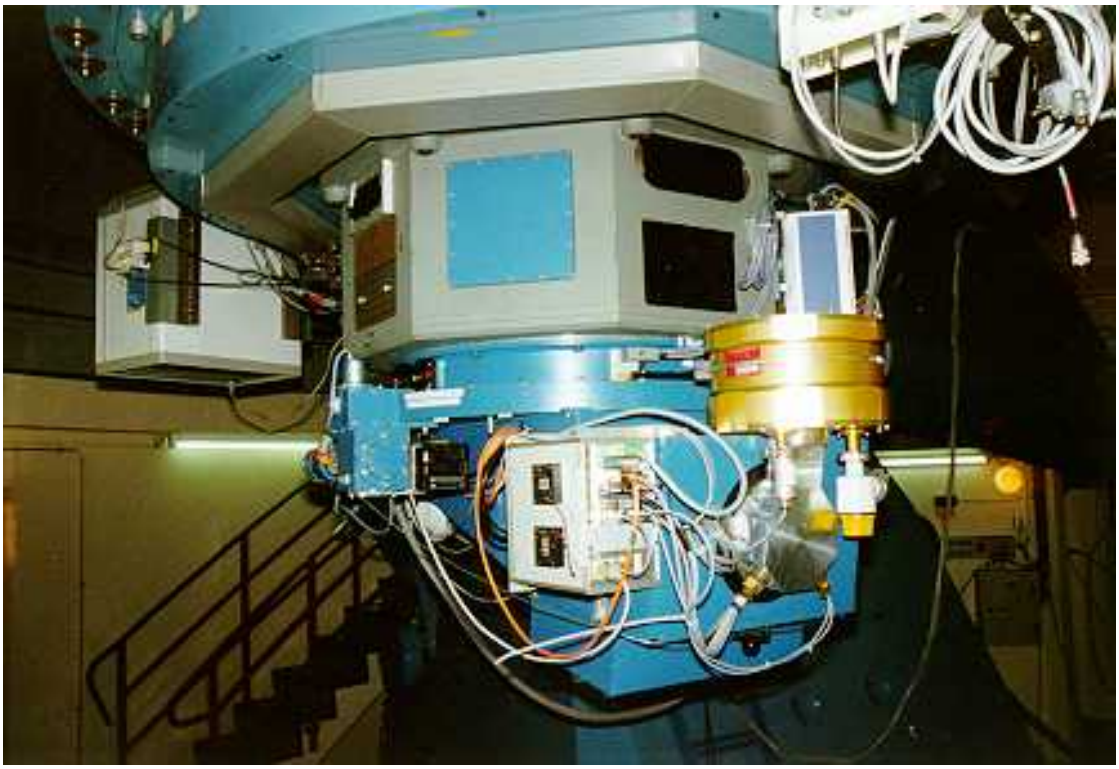

Figure 4.3: The Danish Faint Object Spectrograph and Camera (DFOSC). It consists of a collimator and a camera, between which are a filter and a grism wheel. An aperture wheel is at the telescope focus. Adapted from http://www.ls.eso.org/sci/facilities/lasilla/.

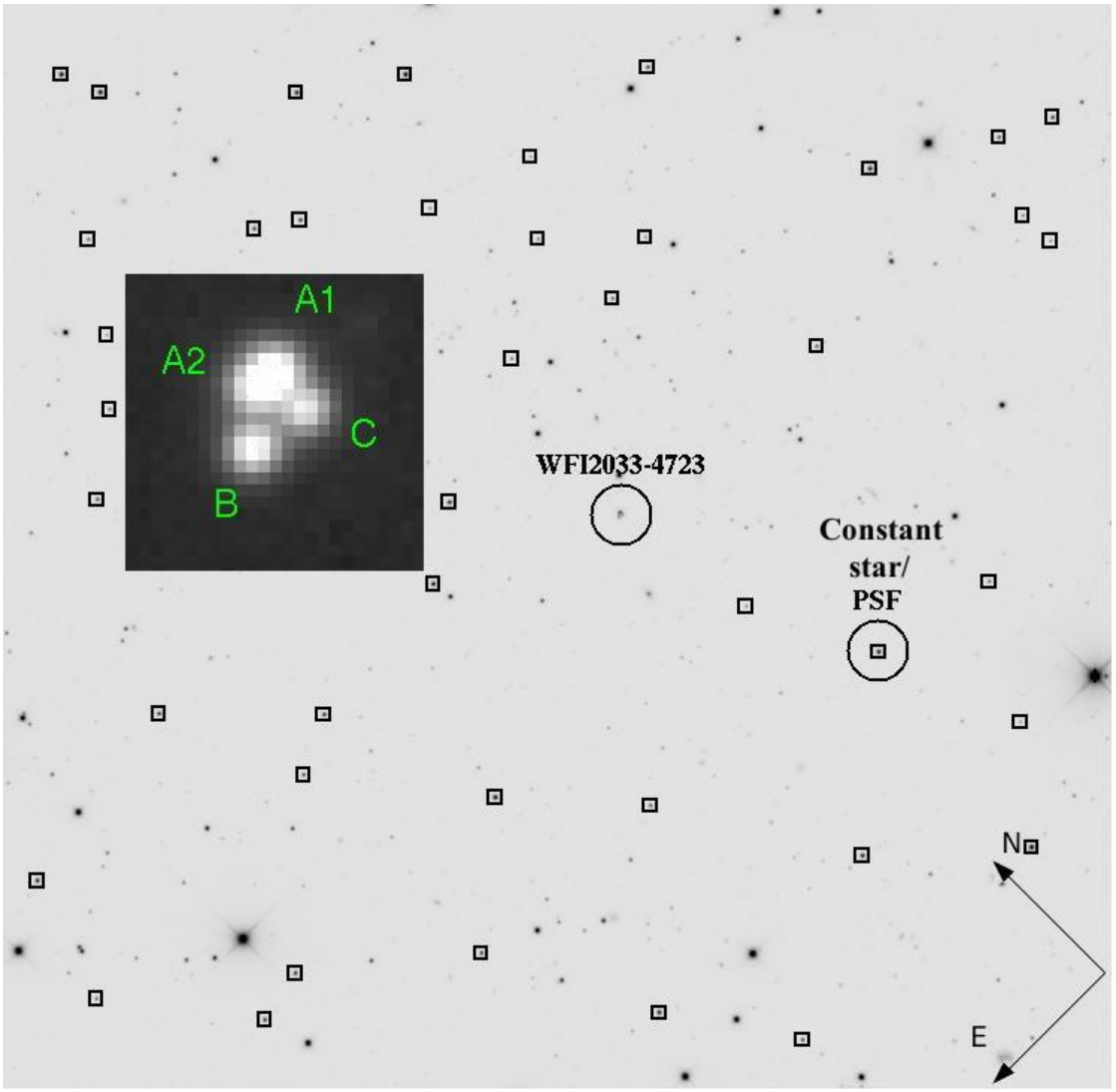

Figure 4.4: V-band image of WFI 2033-4723 obtained by stacking the 14 best seeing and sky background images (V-band template image). The quasar and the star, which we use both as a constant reference and a PSF model, are labelled. The four lensed quasar components are enlarged in the darker box. The field size is 9.7 arcmin × 9.5 arcmin. The stamps used for the kernel computation are defined as 17-pixel squares (See Sect. 6.3.2).

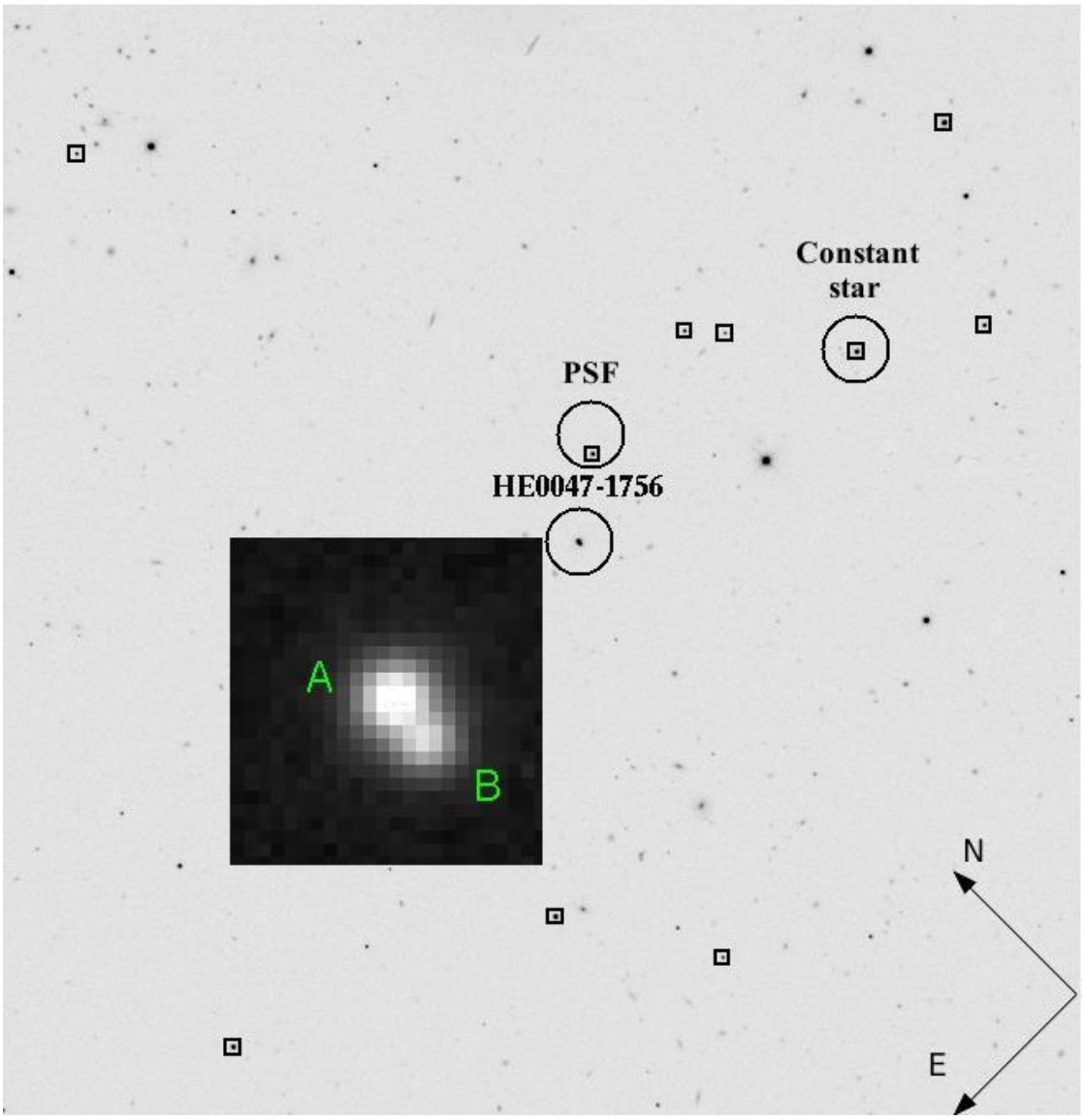

Figure 4.5: V-band image of HE 0047-1756 obtained by stacking the 10 best seeing and sky background images (V-band template image). The quasar and the stars that we use as a constant reference and PSF model are labelled. The double lensed quasar is enlarged in the darker box. The field size is 8.5 arcmin × 8.8 arcmin. The stamps used for the kernel computation are defined as 17-pixel squares (See Sect. 6.3.2).

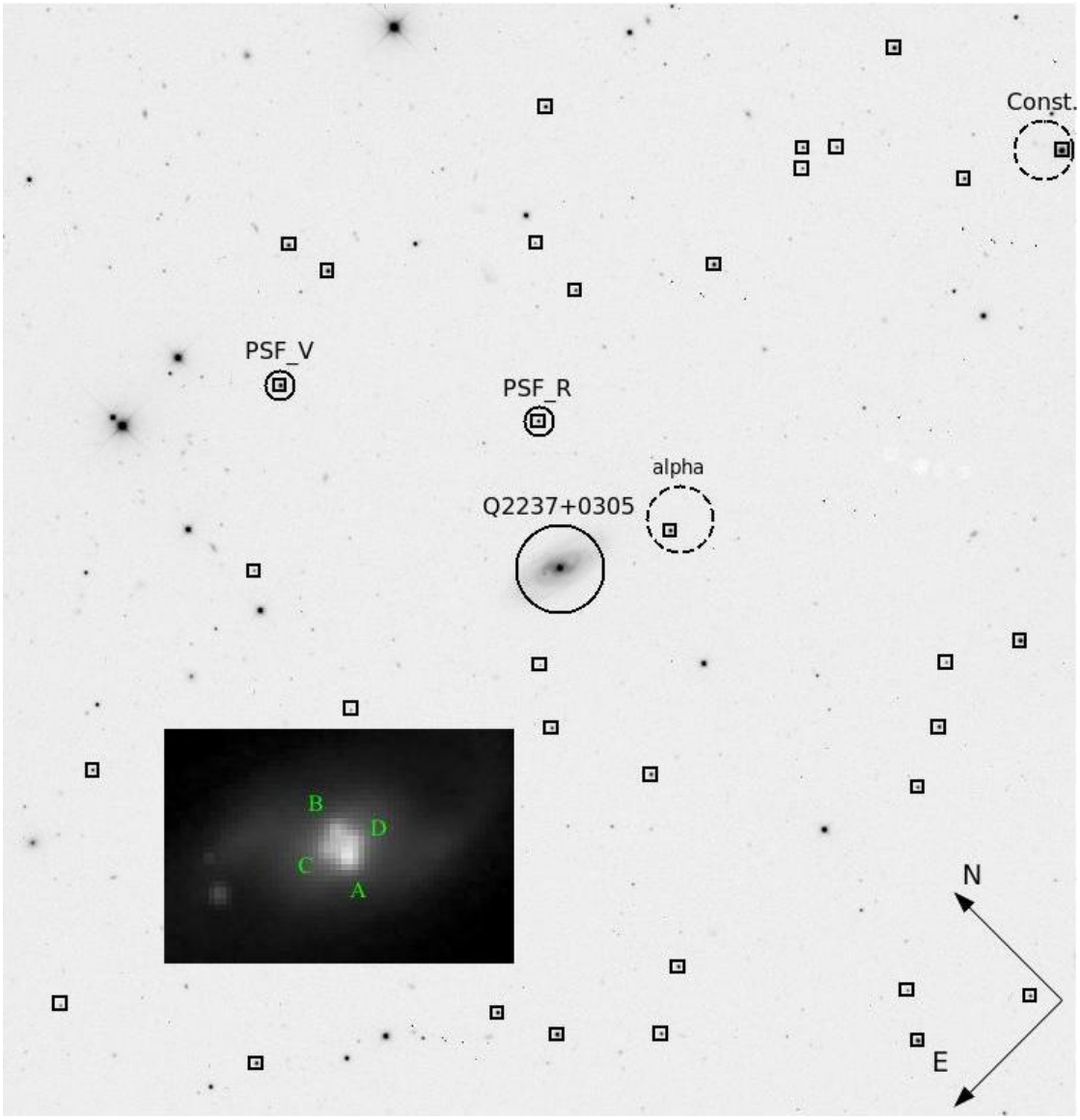

Figure 4.6: V-band image of Q 2237+0305 obtained by stacking the 7 best seeing and sky background images (V-band template image). The quasar and the stars that we use as a constant reference and PSF models are labelled. The alpha star, used in [25] for photometric calibration, is also shown. The quasar is enlarged in the darker box. The field size is 9.7 arcmin × 10 arcmin. The stamps used for the kernel computation are defined as 17-pixel squares (See Sect. 6.3.2).

5 Data Reduction

5.1 Data storage

All the images have been downloaded from the MiNDSTEp wiki page, where all the data taken at the Danish telescope are available, apart from the frames acquired during the year 2012, which were stored on an external hard drive enclosure at the end of the observing run at La Silla in August/September 2012. Before proceeding with further analysis, all the nightly frames have been flat fielded, bias subtracted, corrected for bad columns, aligned to a common reference frame, trimmed at the edges in order to enclose the same region, and finally, the images taken during a single night have been median combined, in order to improve their signal-to-noise ratio and remove cosmic rays.

5.2 Flat Fielding and bias correction

All but 2012 data have been processed right after they were acquired at the telescope, using a software with the purpose of performing flat fielding and bias subtraction. The above pipeline also deleted all raw flat field and bias frames afterwards. Unfortunately we found two computational mistakes in the pipeline, both in the flat fielding and bias subtraction procedures. It was necessary to construct a back-up method to retrieve the correct flat field correction and bias subtraction. The pipeline at the telescope computed the master flat field frame by mean-combining a set of single dome flat field exposures and dividing the resulting frame by its mean value, calculated though without excluding the overscan regions of the DFOSC detector. The resulting flat field frame was subtracted with a wrong bias master frame normalized by dividing the correct mean-combined master frame by its mean, calculated over the entire set of pixels. In other words, the subtracted bias frame had average one, practically meaning that no bias frame was ever subtracted by the collected data. An example of frame produced by the above pipeline is showed in Fig. 5.1: the typical donuts related to the inhomogeneous response of the detector remain uncorrected. In order to obtain the correct flat field frame, the flat field frame computed by the pipeline was subtracted a bias mean value,

calculated from the overscan regions, and then divided by its mean calculated over a smaller region of responsive pixels. The flat field master frames for the year 2012 were instead computed by mean-combining the available dome flat field exposures and dividing them by the mean of the resulting frame, after having subtracted from each of them the corresponding bias master frame. All the science images (except for 2012) were then subtracted their mean bias value (from the overscan regions) and divided by the retrieved flat field master frames. Bad columns were replaced with the appropriate median of surrounding pixels. An example of science image, processed as described above, is shown in Fig. 5.2. As it can be seen, the chip response inhomogenities and the bad column features have been now correctly treated. Science frames collected in 2012 were instead subtracted the corresponding bias master frame and divided by the appropriate flat field master frame.

5.3 Image alignment

Before subtraction, all images need to be astrometrically aligned to a reference frame. The reference image of a given source is an image in a given passband characterized by a very good seeing and low sky background. All the other images of the same quasar are registered onto the reference coordinate grid, also when taken in a different photometric band. This is carried out using the ISIS[1] package by C. Alard ([9], [8]). The astrometric alignment routine of this package efficiently identifies reference stars in the field and performs a two-dimensional polynomial mapping to the reference image. We chose a polynomial transformation of order 2 to remove the shifts and small rotations between the images. In the case of WFI 2033-4723, the average residuals corresponding to the astrometric transform along the x- and y-axes were of the order of 0.1 pixel and the mapping was computed using on average ≈ 275 objects. The astrometric transforms corresponding to HE 0047-1756 were characterized by average residuals of the order of 0.2 pixel and obtained taking into account on average ≈ 220 objects. In the case of Q 2237+0305, the average residuals were of the order of 0.18 pixels and 164 objects were identified on average for the tranform computations. Image resampling was performed through bicubic splines. All images of a given night for the whole data set were trimmed at the edges to contain the same region and median combined to improve the signal-to-noise ratio and correct for cosmic rays. The combination was made by using the IRAF routine IMCOMBINE, which combined images with different exposure times and sky background levels by carrying out an appropriate scaling and by adding a background constant before stacking them. After discarding images with high sky background, disturbed by moonlight, clouds, bad tracking and bad columns, we finally used 85 nights for WFI 2033-4723, 108 nights for HE 0047-1756 and 57 nights for

[1] http://www2.iap.fr/users/alard/package.html

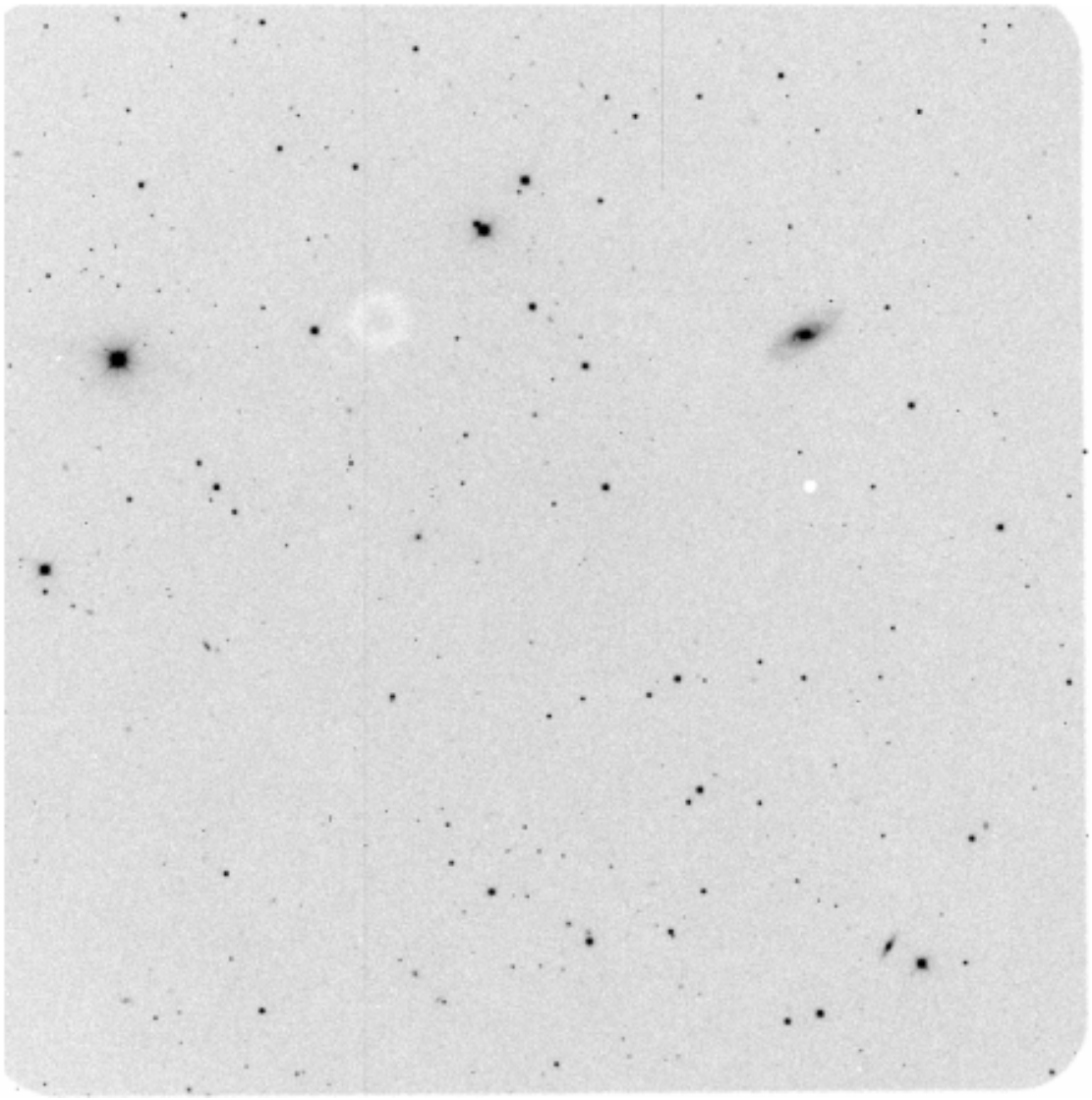

Figure 5.1: A 300 s exposure frame of the quasar Q 2237+0305 in the V band (2008-06-05), as reduced by the automated pipeline at the Danish telescope. Typical pixel response inhomogenities and bad columns are left uncorrected.

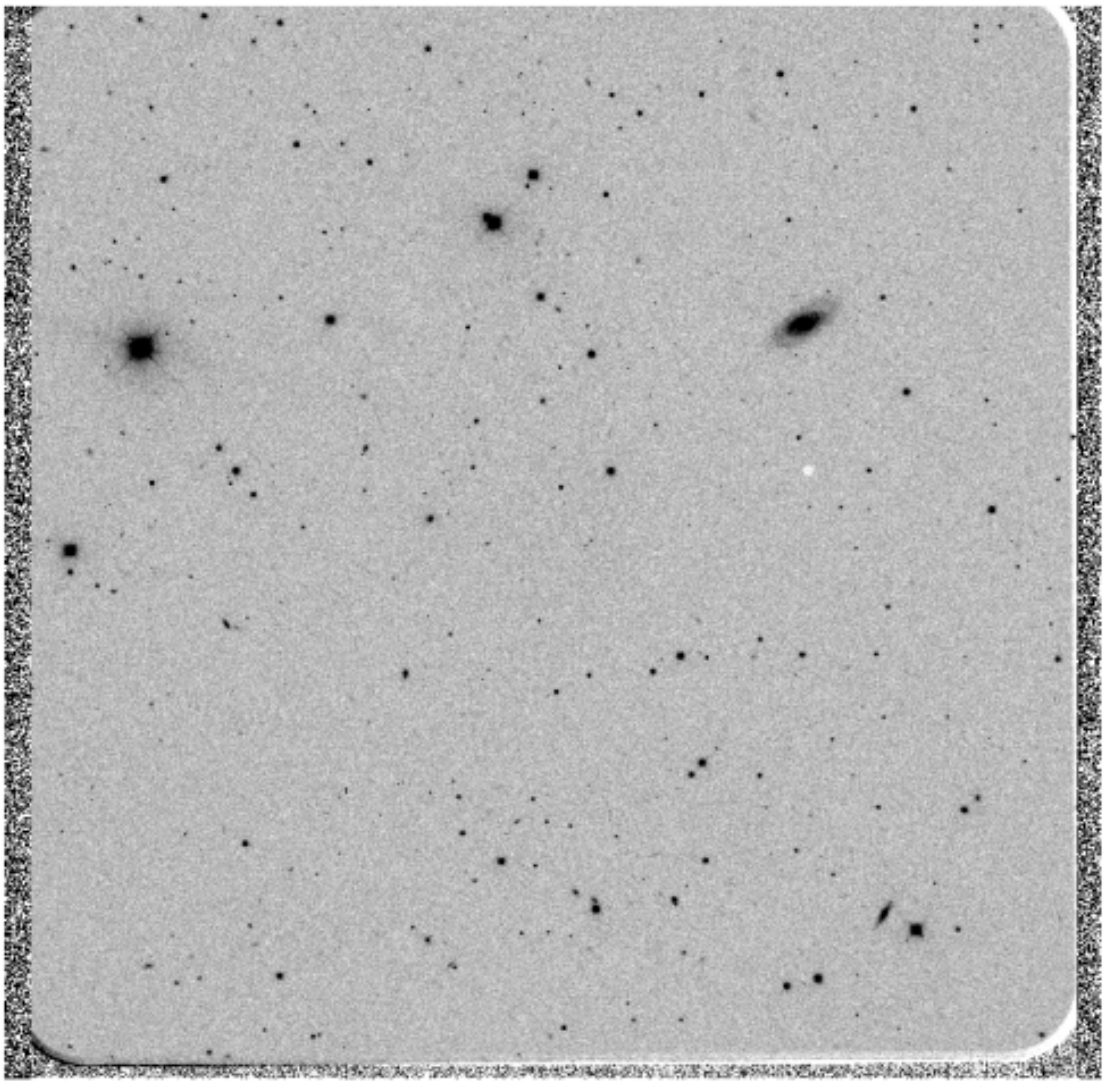

Figure 5.2: A 300 s exposure frame of the quasar Q 2237+0305 in the V band (2008-06-05), as reduced by correcting the computational mistakes found in the Danish telescope reduction pipeline. Typical pixel response inhomogenities and bad columns are now corrected.

Q 2237+0305 in five years. V- and R-band images were not always both available at a given night. The images were finally ready for applying the differential image subtraction technique and proceeding to further analysis.

6

Theory and Practice of Differential Image Analysis

6.1 Differential Image Analysis applied to lensed quasars: an overview

As was shown in the case of Huchra's lens ([173],[10],[101], [153]), an optimal procedure to perform photometry in the case of a multiply imaged quasar is the difference image analysis method (DIA) proposed by [9] and [8]. The basic principle is to use a high signal-to-noise template image, with good seeing and low sky background, which is subtracted from every other target frame in the data set. Since the contribution from the galaxy, which is not expected to vary, is removed in the subtracted images, modeling the galaxy light distribution is no longer required. This greatly simplifies the photometry of the quasars. Before proceeding to subtraction, each pair of images needs to be astrometrically and photometrically aligned. After subtraction, relative photometry can be carried out. This is achieved by building a model for the quasar images with a blend of known PSFs making use of the HST astrometry of the quasar.
The idea of Alard & Lupton [9] is to compute the best-fit spatially non-varying convolution kernel, which degrades the template PSF into that of the target frame and simultaneously matches atmospheric extinction and exposure time. The authors show that by decomposing the kernel as a linear combination of N basis functions, its computation can be as simple as determining a finite number of kernel coefficients. The coefficients are found by solving a linear system of equations containing various moments of the two input images. The chosen convolution kernel is a sum of several Gaussians, which are multiplied by polynomials to model the possible asymmetry of the kernel. The Gaussian widths depend on the relative sizes of the PSF in the template and target frame. Alard [8] extended this technique to the case of a kernel that varies across the chip. Assuming that the amplitudes of the kernel components are polynomial functions of the pixel coordinates of order n, the number of kernel coefficients of each component becomes (n+1)(n+2)/2 larger than in the constant kernel problem.

6.2 Full theory of the Alard&Lupton image subtraction method with constant and space-varying convolution kernels

In their first paper, published in 1998, [9] presented a method for optimal subtraction of two images collected with different observing conditions (i.e. seeing, exposure time, atmospheric extinction) in order to provide a new and fast method to analyze variability of astronomical sources. After choosing the best signal-to-noise, seeing and low sky background image (template) and registering the template and the target image to the same coordinate grid, the method carries out the matching between the two different PSFs. This approach consists of finding the least-square solution for the convolution kernel K(u,v), with u and v coordinates in the kernel coordinate space, which convolves the template T(x,y), with x and y coordinates in the image coordinate space, to give, as a result, the target frame I(x,y) according to the following equation

$$T(x,y) \otimes K(u,v) = I(x,y). \tag{6.1}$$

When decomposing the kernel as a sum of k basis functions, the above problem becomes a linear least-squares problem. By using a kernel of the form:

$$K(u,v) = \sum\nolimits_k a_k B_k(u,v), \tag{6.2}$$

the squared difference between $T(x,y) \otimes K(u,v)$ and $I(x,y)$ is minimized by solving the following linear system for the unknown coefficients a_k

$$\boldsymbol{M}\boldsymbol{a} = \boldsymbol{V}, \tag{6.3}$$

where

$$M_{i,j} = \int C_i(x,y) \frac{C_j(x,y)}{\sigma^2(x,y)} dxdy \tag{6.4}$$

$$V_i = \int I(x,y) \frac{C_i(x,y)}{\sigma^2(x,y)} dxdy \tag{6.5}$$

$$C_i(x,y) = T(x,y) \otimes B_i(u,v). \tag{6.6}$$

By looking for a kernel solution with least-squares, the authors have implicitly approximated the image Poisson statistics by a Gaussian distribution $\sigma(x,y)$ and assumed that the template noise is negligible. The basis functions are chosen to be Gaussian functions of widths σ_n, modified by a polynomial factor. The kernel decomposition assumes the form:

$$K(u,v) = \sum_{n} \sum_{l_n} \sum_{m_n} a_k e^{-\frac{(u^2+v^2)}{2\sigma_n^2}} u^{l_n} v^{m_n} \tag{6.7}$$

where $0 \leq l_n \leq D_n$ and $0 \leq l_n + m_n \leq D_n$, being D_n the degree of the polynomial modifying the Gaussian component n. Each component n admits a total of $(D_n+1)(D_n+2)/2$ terms. The value of k is determined by the values of the other indexes n, l_n, m_n.

In crowded fields, with many stars for modeling the PSF, the fit can be carried out over small regions and the kernel variations can be neglected. On the other hand, in the case of sparse fields when dealing with quasars or supernovae, the number of objects needed to compute the kernel cannot be found in a small area and the kernel variations cannot be ignored. Moreover, by introducing new coefficients in order to solve for the kernel variations, the computing time will increase as the square of the number of the coefficients. These considerations led Alard to the publication of a second paper, [8], in which a method for image subtraction with non-constant kernel solutions is proposed. This allows to obtain a solution investing little additional computing time.

To describe the spatial variation of the kernel as a function of the variables x and y, the kernel can be decomposed as a sum of basis functions at each spatial point (x,y). Hence, the coefficients a_k will become functions of (x,y). Assuming that the coefficients a_k are polynomial functions of degree d_k

$$a_k(x,y) = \sum_{i,j} b_{i,j}^k x^i y^j, \tag{6.8}$$

the resulting kernel can then be written as:

$$K(u,v)_{x,y} = \sum_{n} \sum_{l_n} \sum_{m_n} \sum_{i,j} b_{i,j}^k x^i y^j e^{-\frac{(u^2+v^2)}{2\sigma_n^2}} u^{l_n} v^{m_n}, \tag{6.9}$$

where the notation is the same as in Eq. 6.7, $0 \leq i \leq d_k$ and $0 \leq i + j \leq d_k$.

In this case, finding a least square solution to the Eq. 6.1 is equivalent to solving the following linear system for the coefficients $b_{i,j}^k$

$$M\boldsymbol{b} = \boldsymbol{V}, \tag{6.10}$$

where the matrix element $M_{p,q}$ is given by

$$M_{p,q} = \int W_p(x,y) P_p(x,y) W_q(x,y) P_q(x,y) dxdy. \tag{6.11}$$

The indexes p and q span over the number N of unknown coefficients, $(D_n+1)(D_n+2)(d_k+1)(d_k+2)/4$ for each component n. The functions appearing in the matrix are given by

$$W_p(x,y) = \frac{T \otimes B_p(x,y)}{\sigma(x,y)} = \frac{C_p(x,y)}{\sigma(x,y)} \tag{6.12}$$

and

$$P_p(x,y) = x^{i_p} y^{j_p}. \tag{6.13}$$

The components of vector $\boldsymbol{V}$ have the form:

$$V_p = \int I(x,y) \frac{W_p(x,y)}{\sigma(x,y)} P_p(x,y) dxdy. \tag{6.14}$$

All the above integrals extend over the entire images. By dividing the integration area into smaller sub-areas of index r and center (x_r, y_r), within which the kernel can be considered constant, the above matrix becomes

$$M_{p,q} = \sum_r P_p(x_r,y_r) P_q(x_r,y_r) \int_{D_r} W_p(x,y) W_q(x,y) dxdy \tag{6.15}$$

and the above vector takes the form

$$V_p = \sum_r P_p(x_r,y_r) \int_{D_r} I(x,y) \frac{W_p(x,y)}{\sigma(x,y)} dxdy. \tag{6.16}$$

From Eq. 6.4, 6.5, 6.6, 6.15 and 6.16, it can be seen that solving the kernel equation in the case of a spatially-varying kernel can be simply deduced from solving the equations for the constant kernels corresponding to the image sub-areas and summing over the sub-area solutions. This approximation allows to compute a non-constant kernel solution with minimum additional computing time.

6.3 Image subtraction in practice

In this thesis image subtraction was carried out with the HOTPAnTS[1] software by A. Becker, which is an enhanced and modified version of the [8] method and the corresponding implementation software ISIS. This software is given the template image and the target frames to be processed. In creating the template images, we stacked the frames with the best seeing and sky background at our disposal. In the case of WFI 2033-4723 we computed the median stack of 14 images, both in the V- and R- bands. A similar

[1] http://www.astro.washington.edu/users/becker/hotpants.html

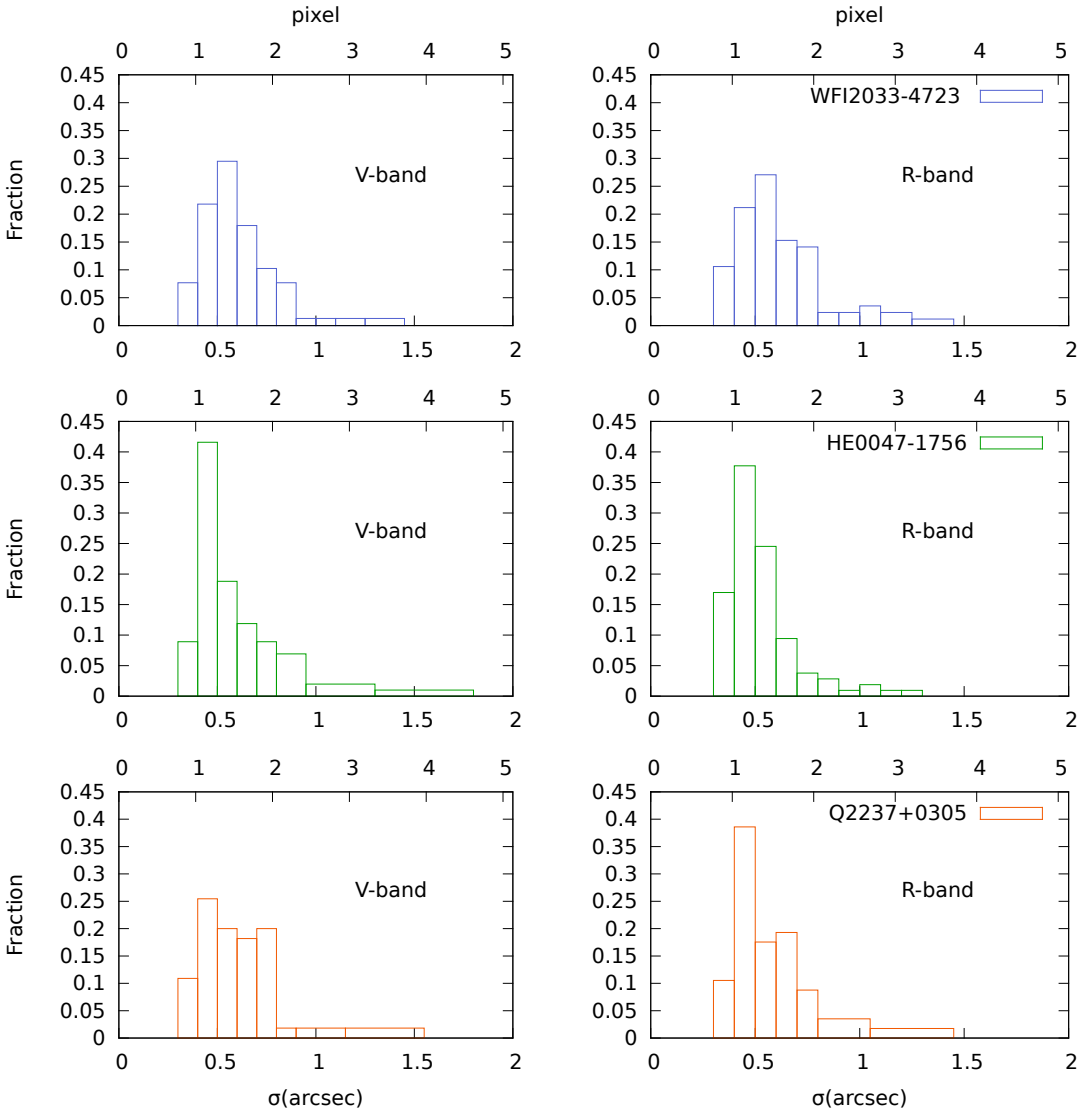

Figure 6.1: FWHM distributions of a nearby star of WFI 2033-4723 (top), HE 0047-1756 (middle) and Q 2237+0305 (bottom) in filters V (left) and R (right) in terms of the corresponding Gaussian σ.

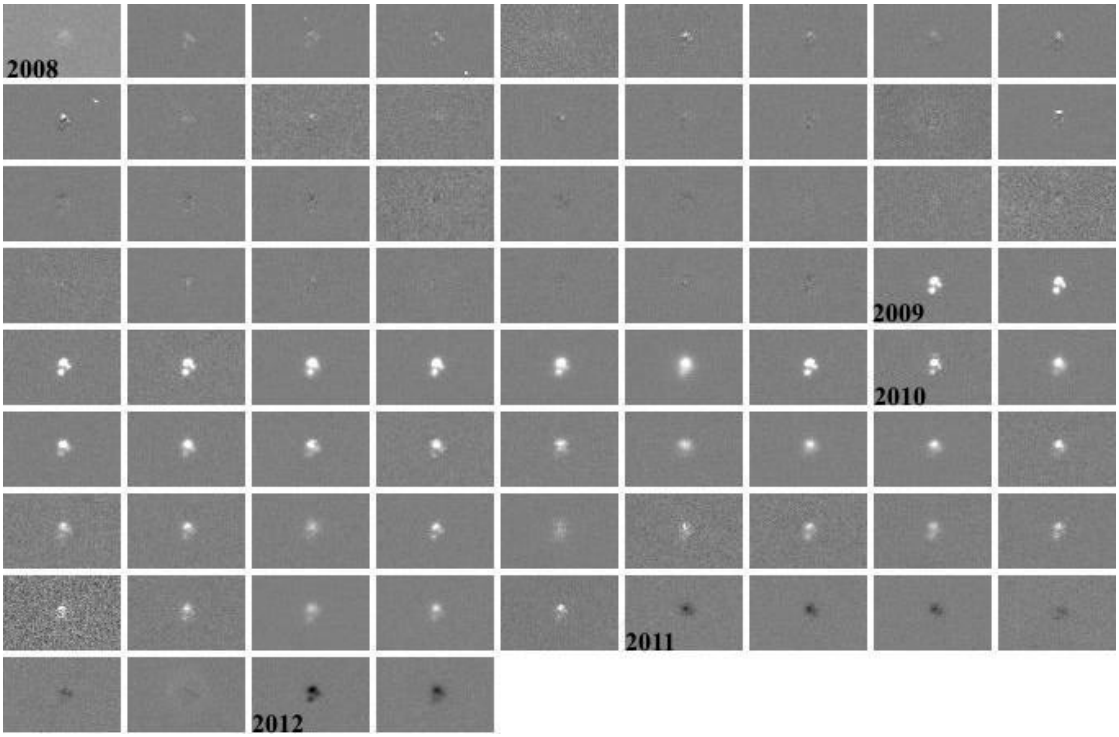

Figure 6.2: V-band difference images of WFI 2033-4723 from 2008 to 2012. The corresponding dates are listed in Table 11.2.

procedure was carried out in building the template images for HE 0047-1756, for which we were able to combine 10 frames in V and 14 frames in R. In the case of Q 2237+0305 we used 7 frames in the V-band and 14 frames in the R-band.

6.3.1 HOTPAnTS modus operandi

HOTPAnTS divides the frames into square regions, within which smaller regions called *stamps*, centered on individual stars, are chosen. The software is also given the list of stars at the center of the stamps. A kernel solution is derived for each stamp.The kernel sum is used as a first metric to discard bad stamps. The photometric scaling between two images is the sum of the convolution kernel. This result follows from Eq. 6.1 and from noticing that the integral of the convolution of two functions is the product of their integrals. In formulas,

$$\int (T \otimes K)(x,y)dxdy = \int T(x,y)dxdy \int K(u,v)dudv = \int I(x,y)dxdy. \qquad (6.17)$$

From the two rightmost terms it can be concluded that $F_I = F_T K_{SUM}$, where F_I and F_T indicate the flux of a source in the image and template respectively and K_{SUM} is the sum of the kernel.

This can be used to discard variable stars (not suitable for determining the photometric alignment between the images) by sigma-clipping outlier stamps from the distribution of the kernel sums. It is useful to have multiple choices in a particular image region in case any objects are sigma-clipped. At this stage, another metric is used to discard bad stamps: after convolution and subtraction, the mean of the distribution of pixel residuals divided by the estimated pixel variance across each stamp provides an additional figure of merit to sigma-clip stamps out and replace them with neighboring stars. The constraints on the convolution kernel for each stamp then allow for the fitting of the coordinate dependent amplitudes of the kernel components.

6.3.2 HOTPAnTS implementation

As analytical kernel basis functions we chose three Gaussians, which were modified by multiplicative polynomials of orders 4, 3 and 2, respectively, with the aim of modeling the kernel asymmetries. In general, we chose a narrow Gaussian which varied to order 4, a central wider Gaussian which varied at order 3 and a broad Gaussian, which varied at order 2, in the coordinates (u,v) of the kernel space. The values of the Gaussian widths σ were computed on the basis of the seeing range of the templates and target frames given to HOTPAnTS. For the target frames we computed, in the V and R bands, the seeing distribution of a star in the quasar neighborhoods. We obtained the

corresponding σ distribution, as shown in Fig. 6.1, making use of the relation between the Full Width at Half Maximum (FWHM) and the σ of a Gaussian profile. The triplet (0.8,1.4,2.3), expressed in pixel units, was a good general choice to build the kernel basis functions which, convolved with the typical template σ of 1 pixel, reproduced the typical target frame σ values. These values were hence adopted as our Gaussian widths. The polynomials modeling the spatial variation of the kernel amplitudes were allowed to vary at spatial order 2 in the image space coordinates (x,y). The final number of stamps differed from case to case since it in general depended on the star distribution in the field. The field characterizing the frames of WFI 2033-4723 was rich with stars, while those corresponding to HE 0047-1756 and Q 2237+0305 were quite sparse. The convolution kernel of WFI 2033-4723 was derived by taking into account on average 27 stamps in V and 26 in R; on average 8 stamps in V and 10 in R defined the convolution kernel for HE 0047-1756. In the case of Q 2237+0305, 15 stamps were used on average in the V-band and 12 in the R-band. The size of the stamps of 17×17 pixels was such that it contained the whole star flux profiles. Figs. 4.4, 4.5 and 4.6 show the squares defining the stamps that HOTPAnTS selected across all observing seasons in the filters V and R for the three systems.
Additional necessary inputs for the HOTPAnTS software were the target frame and template gain (G) and readout noise (RON). Throughout the years 2008-2011 the instrumental gain G was $0.76\,e^-/ADU$ and the readout noise RON was $3.21\,e^-$. The G and RON values changed in 2012 due to an upgrade of the DFOSC detector between 2011 and 2012. The values valid for 2012 are $G = 0.24\,e^-/ADU$ and $RON = 5.28\,e^-$. [2] The gain and RON had to be adjusted appropriately before giving them to HOTPAnTS. Since both the target frames and the templates are in general stacked images, we needed to define an effective G and RON by using standard variance propagation. Starting from the following expression for the stacked image

$$I = \sum_{1}^{N} \frac{F_i \times I_i}{N}, \tag{6.18}$$

where I_i represents a single exposure, F_i the weights which bring the single exposures to a common exposure time and N the number of single exposures, we defined the corresponding variance ${\sigma_I}^2$, in which we arranged terms in order to isolate the effective readout noise and photon noise components. Another adjustable set of parameters was the model for the sky background, which was selected to be an additive constant. The output by HOTPAnTS was the difference image, with the seeing of the current target frame and the photometric scale of the template, and the corresponding noise map. Fig. 6.2 shows the sequence of difference images for WFI 2033-4723 in filter V.

[2] The G and RON values for 2012 are kindly provided by Noé Kains.

6.4 Photometry

Photometry on the difference images was performed using the GALFIT software (version 2.0.3, [115]). The GALFIT software was modified to allow the fitting of a blend of PSFs with fixed relative separations and linear fluxes. We used it to analyze the lensed quasars in the original images *and* in the difference images. This was done as follows:

1. A nearby star was chosen as a PSF model (the chosen stars are labelled as PSF in Figs. 4.4, 4.5 and 4.6). We used only one star since we noticed a remarkable variation of the PSF through the field and decided to select the closest bright enough, isolated and not saturated star in the neighborhoods. The GALFIT software normalized the star chosen as PSF so that any variability was not an issue. The PSF was built by extracting a 17×17 pixel box surrounding the star; the PSF was sky-subtracted and centered at pixel (9,9) according to the formula reported in the GALFIT manual. We used the IRAF routine IMSHIFT for shifting the PSF center.

2. Using the PSF model, the quasar positions were determined from the *original stacked images* and the templates with GALFIT by keeping all the quasar fluxes and the position of only one of the lensed quasar images as free parameters. The sky background values at the quasar position were fixed to median values estimated from 51×51 pixel empty regions nearby the quasar. The positions of the remaining lensed quasar components relative to the free quasar component were kept fixed at the values shown in Table 6.1, obtained from the CASTLES [3] web page (C.S. Kochanek, E.E. Falco, C. Impey, J. Lehar, B. McLeod, H.-W. Rix) and determined using Hubble Space Telescope data.

   In the case of the *original stacked images* and template images, since in general they contained a number of single exposures with different exposure times, we let GALFIT build the appropriate corresponding sigma image by providing it with the equivalent GAIN and RDNOISE of the frames, since GALFIT was only able to correctly compute the noise image for a stack of N images with identical gain, readout noise and exposure time.

3. In the data of WFI 2033-4723 and HE 0047-1756 we could not significantly detect the lensing galaxies. Our positions were therefore minimally affected by the presence of the $V \approx 21$ mag (WFI 2033-4723) and $V \approx 22.5$ mag (HE 0047-1756) lensing galaxy and in these cases the above description of the determination of the quasar positions was used. Keeping fixed the nightly lensed quasar positions

[3] http://www.cfa.harvard.edu/castles/

Table 6.1: HST relative astrometry of WFI 2033-4723, HE 0047-1756 and Q 2237+0305 images, obtained from the CASTLES webpage.

		A1	A2	B	C
WFI2033	RA(")	2.196 ± 0.003	-1.482 ± 0.003	0	-2.114 ± 0.003
	DEC(")	1.261 ± 0.003	1.376 ± 0.003	0	-0.277 ± 0.003
		A	B		
HE0047	RA(")	0	0.232 ± 0.003		
	DEC(")	0	-1.408 ± 0.003		
		A	B	C	D
Q2237	RA(")	0	0.673 ± 0.000	0.635 ± 0.000	-0.866 ± 0.000
	DEC(")	0	1.697 ± 0.000	1.210 ± 0.000	0.528 ± 0.000

obtained above, we determined the fluxes at the position of the quasar images in the *difference images*. The GALFIT software was allowed to fit negative fluxes as well in order to process the differential fluxes of the subtracted images. In the case of Q 2237+0305, on the other hand, we dealt with a lensing galaxy with an optical average magnitude of ≈ 15 mag. In this case, we opted for fitting the quasar positions on the difference image residual fluxes instead of using the *original stacked images*.
Then we determined the fluxes in the *difference images* at fixed centroids of the quasar images, which were computed by yearly averaging the best fit positions of the quasar images obtained from the procedure above. The result for all quasars were the difference fluxes between the epoch considered and the template image. For the difference image photometry with GALFIT the output noise map from HOTPAnTS was used.

The robustness of the method just described has been tested also by computing the light curves of the four components of quasar HE 0435-1223 ([169], [171]), observed by MiNDSTEp and already published by [125], and comparing them with the results by [26] (in the R band). The consistency of the four light curves, obtained with two different telescopes and two different methods, is very good, as shown in Fig. 6.3, with an average weighted root mean square deviation of $rms = 1.36\sigma$. A similar test has been done by computing with this method the light curves of quasar UM673 ([90], [146], [145]), [142], [39]), observed by MiNDSTEp and published by [124], and comparing the results for the two components with the results obtained in filters V and R by [75]. The average weighted root mean square deviation was $rms = 1.6\sigma$.

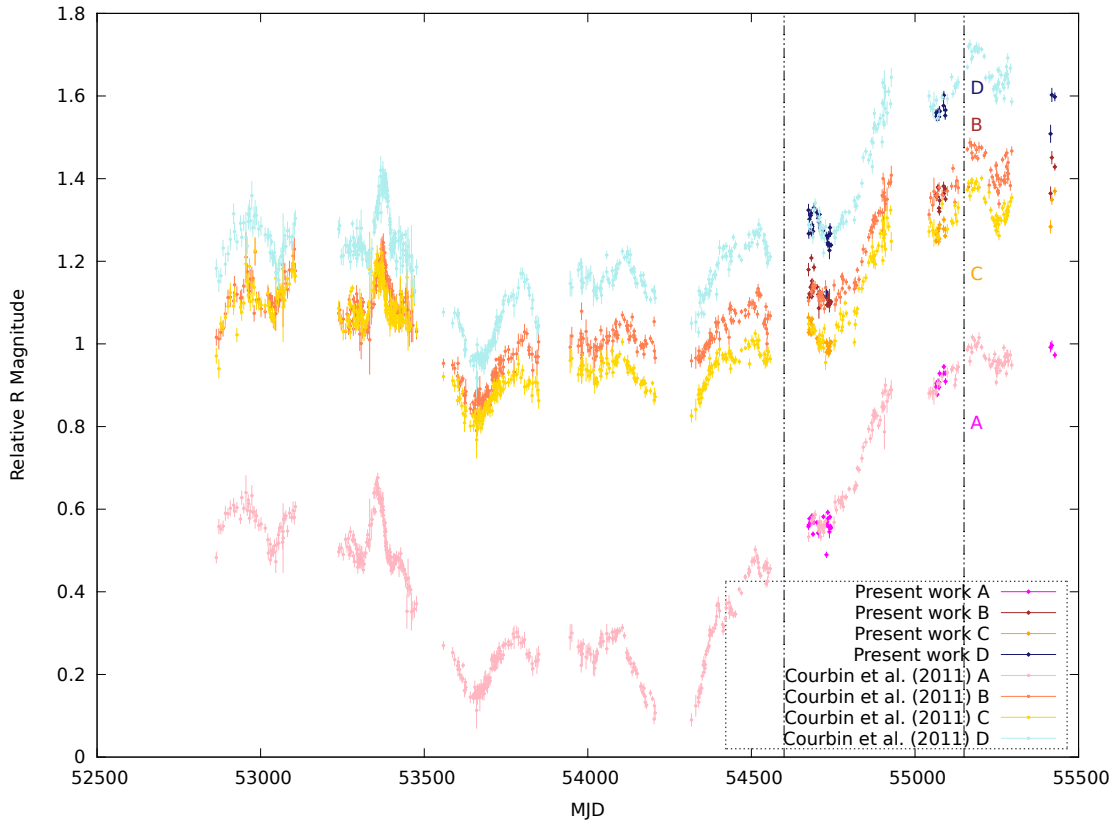

Figure 6.3: The R light curves of the four components of the quasar HE 0435-1223 as of the present work are plotted as a function of the Modified Julian Date (MJD) on top of the corresponding light curves as found by [26] (from 2004 to 2010) with the purpose of showing the consistency of the obtained light curves. The match is only possible in the time span enclosed between the two dashed lines, which corresponds to years 2009 and 2010.

6.4.1 Systematics with using GALFIT

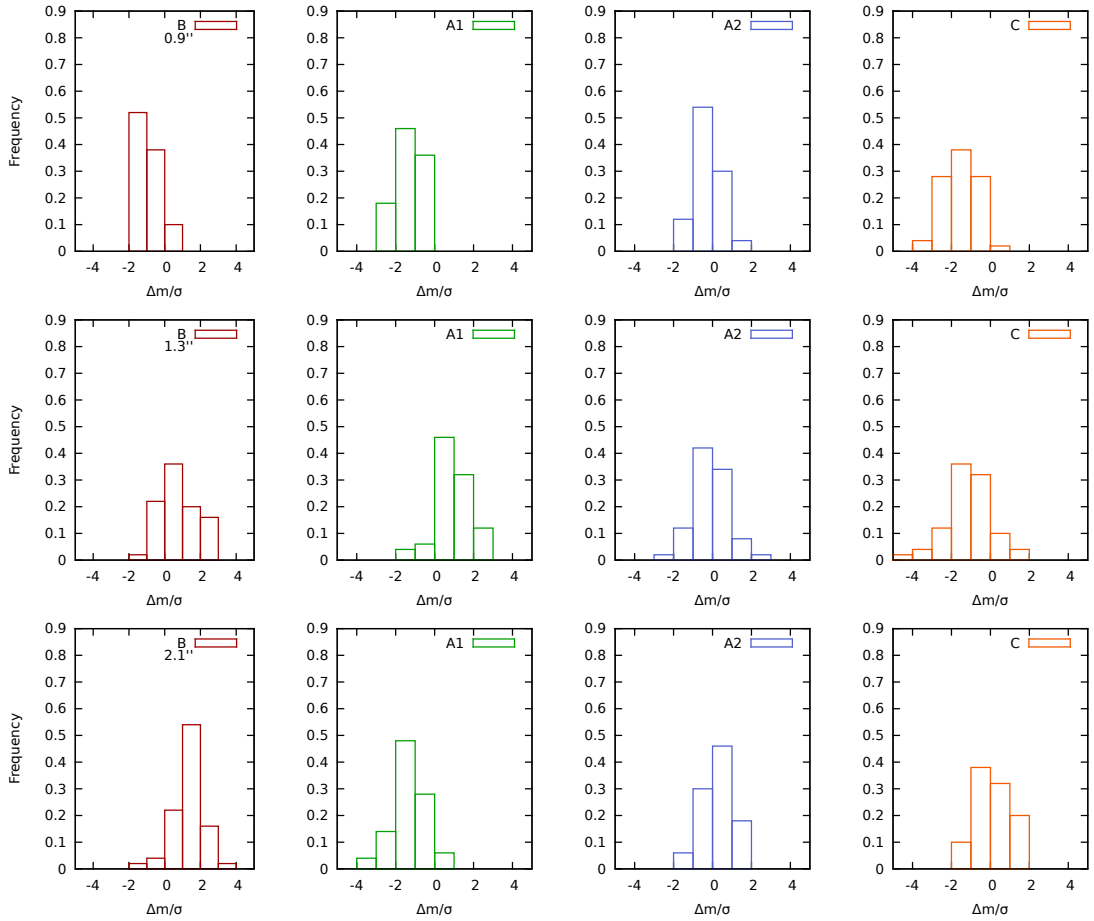

Figure 6.4: Frequency distributions of $\Delta m/\sigma$, the difference between output and input magnitudes in units of GALFIT σ, for the components B, A1, A2 and C of 50 mock models of WFI 2033-4723 under three different seeing regimes.

In order to test the PSF fitting with GALFIT, we created mock models of the quasar WFI 2033-4723 for three different values of the seeing in filter V. We chose to test the case of WFI 2033-4723 because it was characterized by low fluxes and highly blended components. Starting from three images of a real star in the surroundings of the quasar, with FWHM 0.9″, 1.31″, 2.1″, we generated with GALFIT, at each seeing value, 50 artificial realizations of the quasar, with flux values as computed from the V template and taking those into account as mean values of the corresponding Poissonian noise. The quasar centroid was chosen, at each realization, within one pixel, with a uniform distribution. To each artificial quasar was added a sky background with mean value

as computed from the V template, including Poissonian noise, and a Gaussian readout noise realization obtained with the IRAF routine MKNOISE. No lensing galaxy was included in these simulations. The photometry of the artificial models was then carried out with GALFIT, choosing a PSF close to that used in building the artificial models. Fig. 6.4 shows the distribution of the ratio $\Delta mag/\sigma$, which represents the difference between the GALFIT output flux and the known input flux, in units of GALFIT sigmas, for the quasar images and for the three values of seeing. The majority of realizations lies between $\Delta mag/\sigma \approx 0-2$ with minor tails at $\Delta mag/\sigma \approx 3$. The effects leading to the systematic discrepancy between the input and output fluxes were determined by the differences between the PSF of the quasar and the PSF chosen to model it. The average magnitude discrepancy in the most frequent seeing regime did not exceed 0.02 mag, negligible for the purposes of this thesis.

7

WFI 2033-4723

In what follows we report the results obtained for the quasar WFI 2033-4723. This material has already been published in the paper [2] listed in the List of Publications.

7.1 Light curves of the quasar WFI 2033-4723

Figure 7.1 shows the light curves for the quasar WFI 2033-4723 components B, A1, A2, C and the constant star in Fig. 4.4 in filters V and R. The light curves are computed by using instrumental magnitudes, which are defined as:

$$m_X = -2.5 \times \log_{10}((\Delta F_X + F_{X,T})/F_{X,Ref}) \tag{7.1}$$

where ΔF_X is the flux difference of the quasar components in the subtracted image, which has the photometric scale of the template, $F_{X,T}$ is the corresponding flux in the template and $F_{X,Ref}$ that of the constant reference stars, marked in Figs. 4.4, 4.5 and 4.6, in the X band. Instrumental colors are defined accordingly from the magnitudes. The individual data points composing the light curves are also listed in Table 11.2. The light curves of images B (filled dots), A1 (asterisks), A2 (squares), C (filled diamonds) are shown in red, green, orange and blue, respectively, as a function of the Modified Julian Date (MJD). The quoted error bars were determined by the GALFIT software, as explained in paragraph 6.4. The illustrated photometric data of the quasar components have been shifted in accordance with the time delays published by [158], namely $\Delta t_{B-C} = 62.6^{+4.1}_{-2.3}$ days and $\Delta t_{B-A} = 35.5 \pm 1.4$ days, with image B leading. Components B, A1, A2, C became brighter in 2009 and dimmer again across the remaining seasons, showing an overall magnitude variation of ≈ 0.6 mag in filter V and ≈ 0.5 mag in filter R. We list in Table 7.1 the average magnitudes, computed within each season, for a more detailed picture of the brightness evolution of the four images. The quoted error bars are standard deviations computed within each season. Fig. 7.2 is intended to reveal any differences between the variation of the four lensed components.

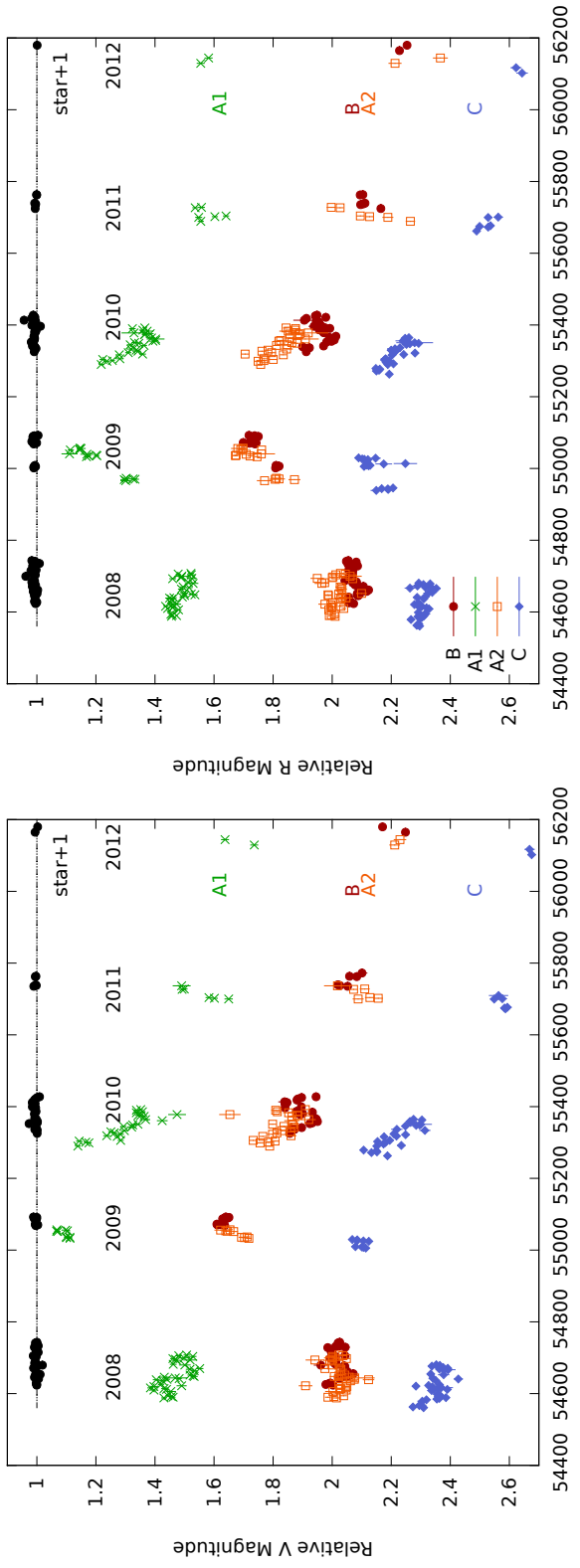

Figure 7.1: V- (left) and R- (right) band light curves of WFI 2033-4723 from 2008 to 2012. Components B (filled dots), A1 (asterisks), A2 (squares), C (filled diamonds) are depicted in red, green, orange and blue, respectively. The light curve of a star in the field, labelled as Constant star/PSF in Fig. 4.4, is shown in black and shifted by +1 mag.

The light curves A2-A1, B-A1, C-A1 are shown in the V and R bands. The differences were computed upon interpolation of the brightest component at the observation dates of the weakest one in the pair after correcting for the time delays between the pair components. The interpolated magnitude was computed according to the following linear interpolation formula

$$m_I = m_0 + (m_1 - m_0)\frac{t_I - t_0}{t_1 - t_0}, \tag{7.2}$$

where m_I is the interpolated magnitude value at the epoch t_I, while m_1 and m_0 are the observed magnitudes corresponding to the epochs t_1 and t_0, respectively, with $t_0 < t_I < t_1$. The error bars of the observed magnitudes were propagated through the interpolation formula on the interpolated magnitude m_I. The error bars of the two terms involved in the difference computation were then added in quadrature. The figures suggest that the variation of component C through the observing seasons differed from the others, showing in the R band a significant variation of ≈ 0.16 mag between 2008 and 2011.

Table 7.1: V-band and R-band yearly averages of WFI 2033-4723 instrumental magnitudes.

	2008	2009	2010	2011	2012
$(B)_V$	2.02 ± 0.03	1.63 ± 0.02	1.89 ± 0.04	2.06 ± 0.03	2.21 ± 0.06
$(A1)_V$	1.47 ± 0.05	1.09 ± 0.02	1.30 ± 0.08	1.55 ± 0.07	1.69 ± 0.07
$(A2)_V$	2.02 ± 0.04	1.67 ± 0.04	1.82 ± 0.06	2.10 ± 0.05	2.22 ± 0.01
$(C)_V$	2.35 ± 0.03	2.10 ± 0.02	2.22 ± 0.06	2.58 ± 0.02	2.67 ± 0.01
$(B)_R$	2.07 ± 0.02	1.76 ± 0.04	1.96 ± 0.03	2.11 ± 0.03	2.24 ± 0.02
$(A1)_R$	1.48 ± 0.03	1.21 ± 0.08	1.33 ± 0.05	1.57 ± 0.04	1.57 ± 0.02
$(A2)_R$	2.01 ± 0.03	1.74 ± 0.06	1.83 ± 0.05	2.12 ± 0.10	2.29 ± 0.11
$(C)_R$	2.30 ± 0.02	2.15 ± 0.04	2.22 ± 0.04	2.52 ± 0.03	2.63 ± 0.02

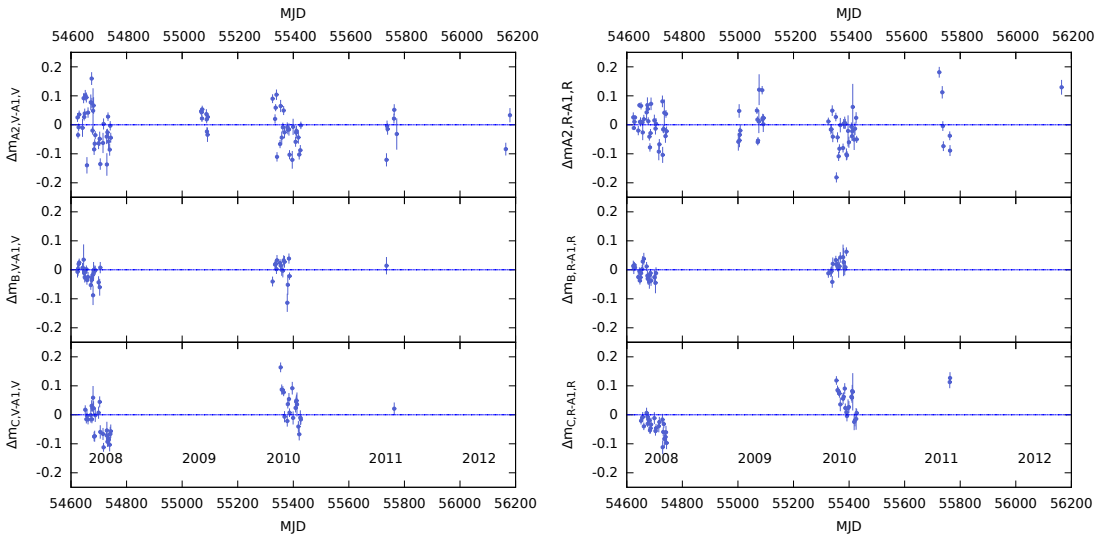

Figure 7.2: The light curves A2-A1, B-A1, C-A1 are shown in the V- (left) and R-band (right) in the upper, middle and bottom panels, respectively. The differences are computed, after correcting for the known time delays, by interpolating in between the data points of the brightest component of each pair and by subtracting their average value. The difference between C and A1 in the R-band shows a significant magnitude variation of 0.16 mag between 2008 and 2011.

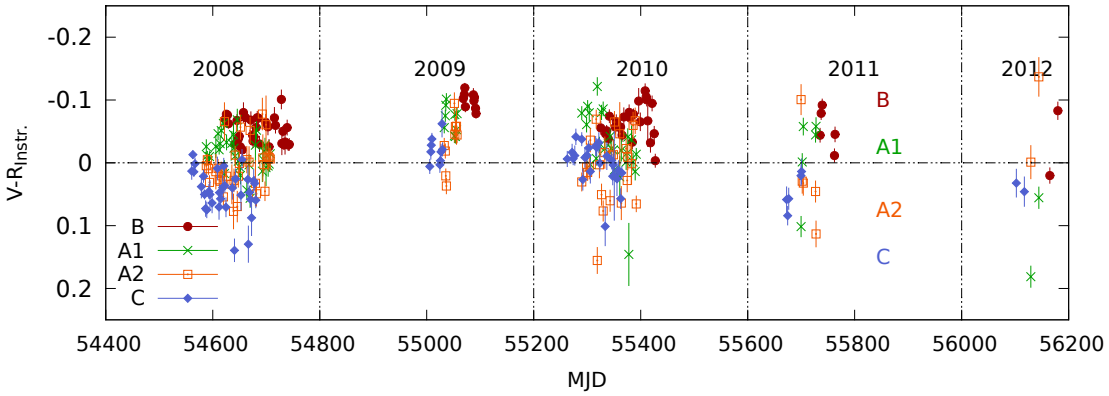

Figure 7.3: $(V-R)_{Instr.}$ light curves of WFI 2033-4723 from 2008 to 2012. Components B (filled dots), A1 (asterisks), A2 (squares), C (filled diamonds) are depicted in red, green, orange and blue, respectively.

Figure 7.3 shows the evolution of the color $(V-R)_{Instr.}$ of the four components. We note that the four images became bluer between 2008 and 2009 by ≈ 0.05 mag, in correspondence to the quasar brightening, and gradually redder through the remaining seasons. We also computed the color difference between the image pairs $A1-B$, $A2-B$, $C-B$, $A1-A2$, $A2-C$, $A1-C$, after interpolating the color of the brightest component of each pair in correspondence to the days at which the other has been observed. The error bars of the two terms involved in the difference computation were added in quadrature. Since quasars emit at different wavelengths from regions of different size, the magnification of the emitted light caused by microlensing will depend on the observed passband. This phenomenon is referred to as chromatic microlensing [161] and implies that the observed color of a quasar image undergoing a microlensing event varies. In absence of lensing we expect the colors of the quasar components to differ only by a constant, caused by the differential intergalactic extinction along their lines of sight. When the color light curves of the quasar images cannot be matched by simply shifting them by a constant, the simplest explanation we can provide is microlensing affecting images in an uncorrelated fashion [161]. We did not find systematic long-term color difference variation across the whole observing campaign, but we cannot not rule out intra-seasonal variations of the order of ≈ 0.1 mag. Intra-seasonal average values of the instrumental color $(V-R)_{Instr.}$ for the four components and color difference between all possible pairs of components are given in Tables 7.2 and 7.3.

Table 7.2: Yearly averages of the instrumental color $V-R_{Instr.}$ for the four lensed components of quasar WFI 2033-4723.

	2008	2009	2010	2011	2012
$(V-R)_{Instr.B}$	-0.05 ± 0.02	-0.10 ± 0.01	-0.06 ± 0.03	-0.05 ± 0.03	-0.03 ± 0.07
$(V-R)_{Instr.A1}$	-0.01 ± 0.03	-0.07 ± 0.02	-0.03 ± 0.05	-0.01 ± 0.07	0.12 ± 0.09
$(V-R)_{Instr.A2}$	0.01 ± 0.04	-0.03 ± 0.04	-0.01 ± 0.08	0.02 ± 0.08	-0.07 ± 0.10
$(V-R)_{Instr.C}$	0.05 ± 0.03	-0.02 ± 0.02	0.00 ± 0.03	0.05 ± 0.03	0.04 ± 0.01

Table 7.3: Yearly average differences of the instrumental color $V-R_{Instr.}$ for all the possible component pairs of quasar WFI 2033-4723.

	2008	2009	2010	2011	2012
$\overline{\Delta(V-R)_{Instr.A1B}}$	0.05 ± 0.03		0.06 ± 0.05		
$\overline{\Delta(V-R)_{Instr.A2B}}$	0.05 ± 0.04		0.03 ± 0.07		
$\overline{\Delta(V-R)_{Instr.CB}}$	0.11 ± 0.05		0.08 ± 0.03		
$\overline{\Delta(V-R)_{Instr.A1A2}}$	-0.02 ± 0.06	-0.04 ± 0.06	0.0 ± 0.1	0.0 ± 0.1	0.19 ± 0.01
$\overline{\Delta(V-R)_{Instr.A2C}}$	-0.05 ± 0.04		-0.01 ± 0.05		
$\overline{\Delta(V-R)_{Instr.A1C}}$	-0.06 ± 0.04		-0.04 ± 0.04		

8

HE 0047-1756

In what follows we report the results obtained for the quasar HE 0047-1756. This material (exception made for Figure 8.6) has already been published in the paper [2] listed in the List of Publications.

8.1 Light curves of the quasar HE 0047-1756

In Figure 8.1 we show the light curves of the quasar HE 0047-1756 from 2008 to 2012 for filters V and R. The individual data points of the light curves are also listed in Table 11.1. The error bars were determined by using the GALFIT software as explained in paragraph 6.4. The light curves for images A and B are plotted in red and green, respectively, as a function of the Modified Julian Date (MJD). The light curve of a star in the field, the constant star in Fig. 4.5, is also shown in black. In the year 2008 the light curves of both lensed quasar images are characterized by a $\Delta m \approx 0.1$ mag intrinsic variation of the quasar on time scales of ≈ 50 days. The data suggest that this rise ends around $MJD - 2450000 \approx 4680$ in image A, but around $MJD - 2450000 \approx 4690$ in image B. This delay of the brightness rise in image B is analyzed in detail in Sect. 8.2. In the year 2009, both quasar images became more luminous. Starting from 2010 the quasar became dimmer and again brighter across the last two periods. The overall variation of magnitude in both filters did not exceed ≈ 0.3 mag. The average instrumental magnitudes of components A and B across the 5 periods are shown in Table 8.1.

Table 8.1: V-band and R-band yearly averages of the HE 0047-1756 instrumental magnitudes.

	2008	2009	2010	2011	2012
$(A)_V$	-0.25 ± 0.02	-0.49 ± 0.02	-0.36 ± 0.03	-0.41 ± 0.01	-0.53 ± 0.01
$(B)_V$	1.21 ± 0.03	1.01 ± 0.03	1.16 ± 0.06	1.19 ± 0.04	1.08 ± 0.03
$(A)_R$	-0.21 ± 0.01	-0.37 ± 0.02	-0.28 ± 0.02	-0.34 ± 0.01	-0.44 ± 0.02
$(B)_R$	1.21 ± 0.03	1.08 ± 0.02	1.20 ± 0.03	1.22 ± 0.02	1.13 ± 0.03

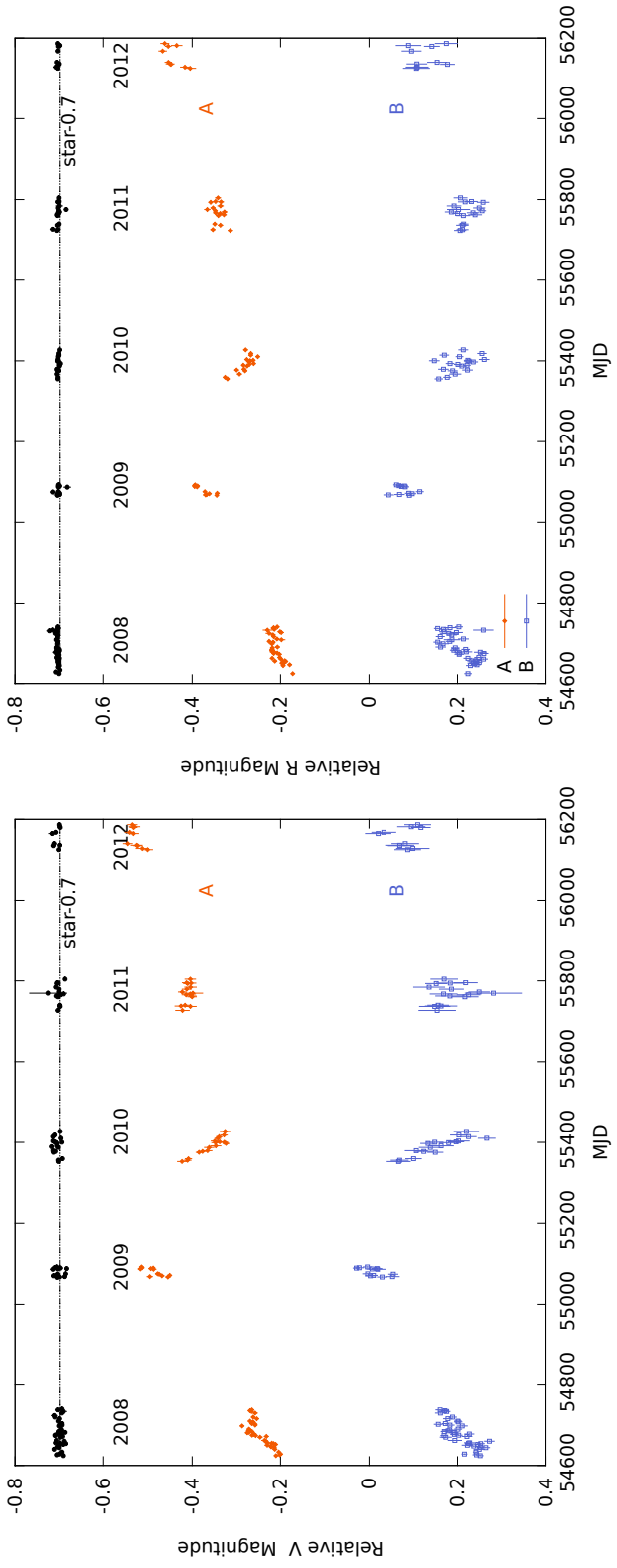

Figure 8.1: V-(left) and R-(right) band light curves of HE 0047-1756 from 2008 to 2012. Components A (filled dots) and B (squares) are depicted in orange and blue, respectively. The light curve of a star in the field, labelled as constant star in Fig. 4.5, is shown in black and shifted by −0.7 mag.

8.2 Time delay for HE 0047-1756

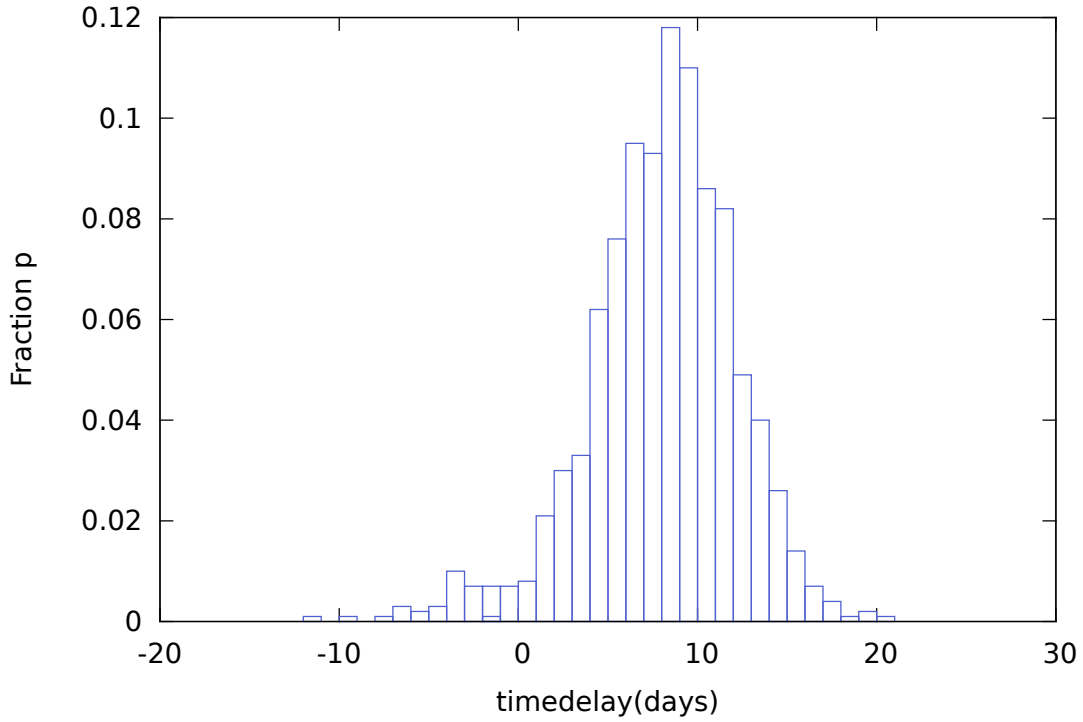

Figure 8.2: Distribution for time delays based on our light curves of components A_V and B_V according to the spline method in [147]. The probability has been computed from 1000 resamplings of the inferred model for the light curves. Mean value and standard deviation of this distribution are $\Delta t = 7.2 \pm 3.8$ days.

Several methods have been introduced in order to determine time delays in lensed systems ([81] and references therein; see also [18], [55], [113], [147]). We applied the PyCS software by Tewes [147] to our V and R light curves from 2008 to 2012. The PyCS software allows for time delay measurements in presence of microlensing, defined as extrinsic variability, as opposed to the intrinsic variability of the quasar. We used the free-knot spline technique and the dispersion method available in the package. Table 8.2 summarizes the main input parameters for the PyCS spline and dispersion methods (see [147] for further details).
The free-knot spline technique uses cubic splines (a spline consists of several polynomial pieces which are connected at the locations of the knots) to model both the intrinsic and extrinsic variability of the light curves and adjusts simultaneously the splines, the time shifts and the magnitude shifts between the light curves in order to minimize a

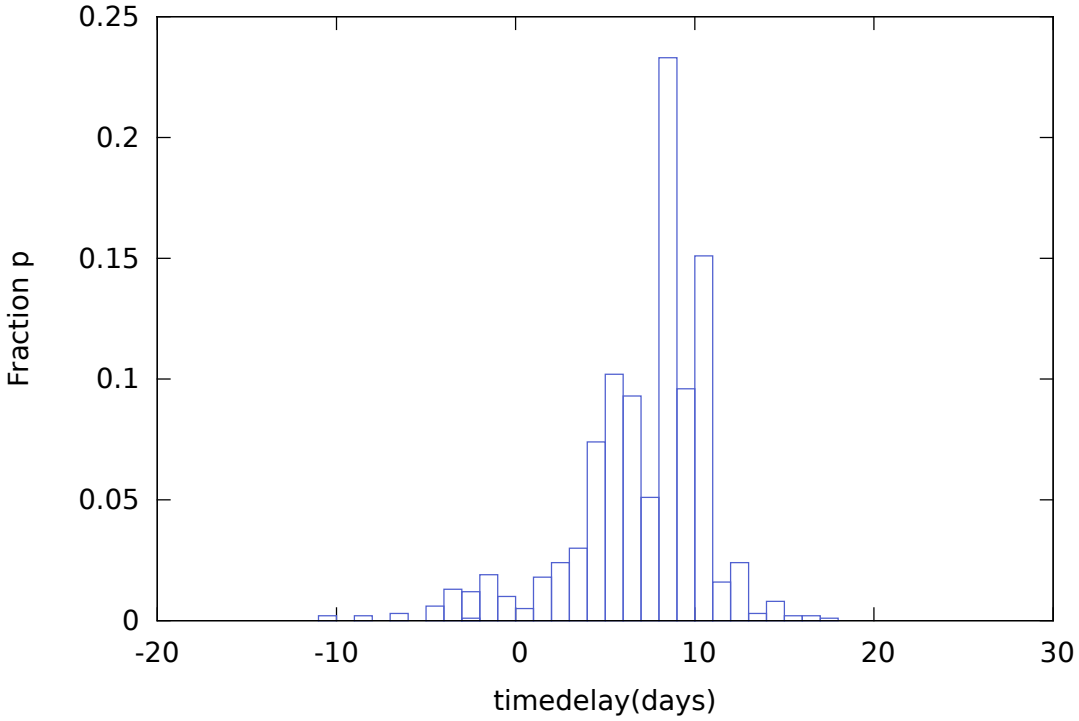

Figure 8.3: Distribution for time delays based on our light curves of components A_V and B_V according to the dispersion method in [147]. The probability has been computed from 1000 resamplings of the inferred model for the light curves. Mean value and standard deviation of this distribution are $\Delta t = 8.0 \pm 4.2$ days

Table 8.2: Summary of the main input parameters for the PyCS spline (spl) and dispersion (disp) methods. Indices A and B refer to the quasar images. η_{intr} and η_{extr} define the initial spline knot separations (in days) for the intrinsic and extrinsic variation models, respectively. ϵ indicates the minimum knot distance allowed in the free-knot spline fits. β and α are the power-law exponent and the scaling factor of the spectrum of the generated noise, respectively. In the dispersion method only data with observational gaps shorter than *interpdist* were interpolated. The low-order polynomials modeling the extrinsic variability in the dispersion method were chosen of order *nparams* (See [147] for detailed explanation.)

$spl : \eta_{intr}$	75 days
$spl : \eta_{extr}$	520 days
$spl : \epsilon$	15 days
$spl : \alpha_A$	1.1
$spl : \beta_A$	0
$spl : \alpha_B$	3.1
$spl : \beta_B$	0
$disp : interpdist$	10 days
$disp : nparams$	1

least-square fitting figure of merit that takes into account all data points.
The dispersion method goes back to the dispersion techniques by [113] and simultaneously adjusts the time shifts and low-order polynomial representations of the extrinsic variability in order to minimize a scalar dispersion function that quantifies the deviations between the two components of all possible combinations of light curves. This method does not assume any model for the intrinsic variability.
The results determined with the spline fitting technique and dispersion technique are 7.2 ± 3.8 days and 8.0 ± 4.2 days, respectively. The mean value and quoted error bars correspond to the mean and standard deviation of the resulting time delay distributions, shown in Fig. 8.2 and 8.3, obtained by drawing 1000 realizations of the observed light curves. The light curve realizations were drawn taking into account a free-knot spline model for the intrinsic variability, a free-knot spline model for extrinsic variability and power-law noise models for the light curves, as explained in [147]. On the other hand, the application of these methods to the R-band data in the years 2008-2012 failed to converge to a unique answer.

We carried out a local analysis on year 2008 in the V band in order to confirm the obtained results and show that the above analysis was not biased by the existence of the observing gaps. We found out that the best way to analyze such a short light curve portion was to follow a linear interpolation scheme, which did not introduce the difficulties of generating the model for the intrinsic and extrinsic variability – necessary inputs for the PyCS software in order to draw new realizations of the light curves – from a reduced number of data points. Our approch, aimed at determining the time delay which minimizes the magnitude difference between the light curves, was published first by [54] and goes back to [81]. It proceeded through the following steps:

1. Component A of each of 10000 bootstrap resamplings of the observed light curve was shifted by the time delay Δt to be tested. The time delay values were chosen in the range from 0 to 50 days (image A leading). Such a high number of resamplings constrained the uncertainties on the time delay measurement.

2. The light curve of the brightest component A was linearly interpolated in correspondence to the dates at which the B light curve had been observed. Only gaps shorter than 20 days were interpolated.

3. Each resampling was smoothed by using a triangular filter with a width δ of 3 and 6 days respectively for the brighter component A and the weaker component B. The use of larger windows, i.e. 6 and 12 days, did not change the results. By using a triangular filter, we determined, for a given component, the magnitude at any epoch t_i as a weighted average of magnitude values corresponding to neighboring epochs t_j with $|t_i - t_j| \leq \delta$. The triangular weight had the following shape

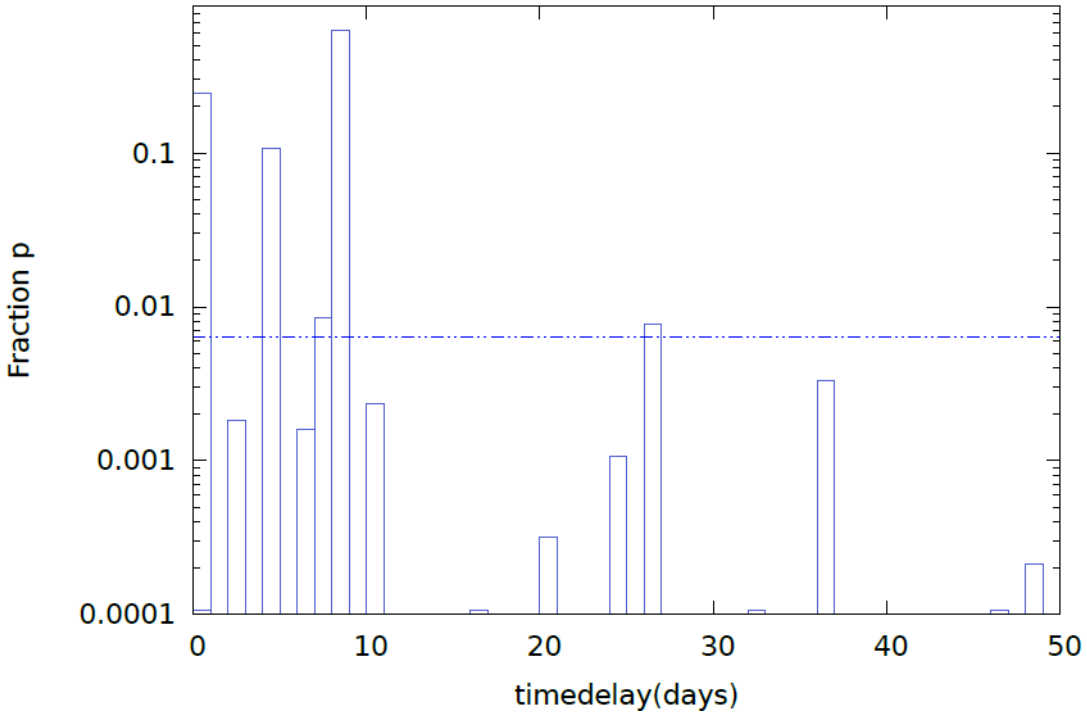

Figure 8.4: Distribution p for time delays between $0-50$ days based on our light curves of components A_V and B_V. The probability has been computed from 10000 bootstrap resamplings of the observed light curves. For each resampling the brightest component A has been interpolated in correspondence to the dates at which B has been observed. The region above the dashed line contains 95% of the statistical weight of the distribution, after discarding the peak at 0 lag. Mean value and standard deviation of this region are $\Delta t = 7.6 \pm 1.8$ days.

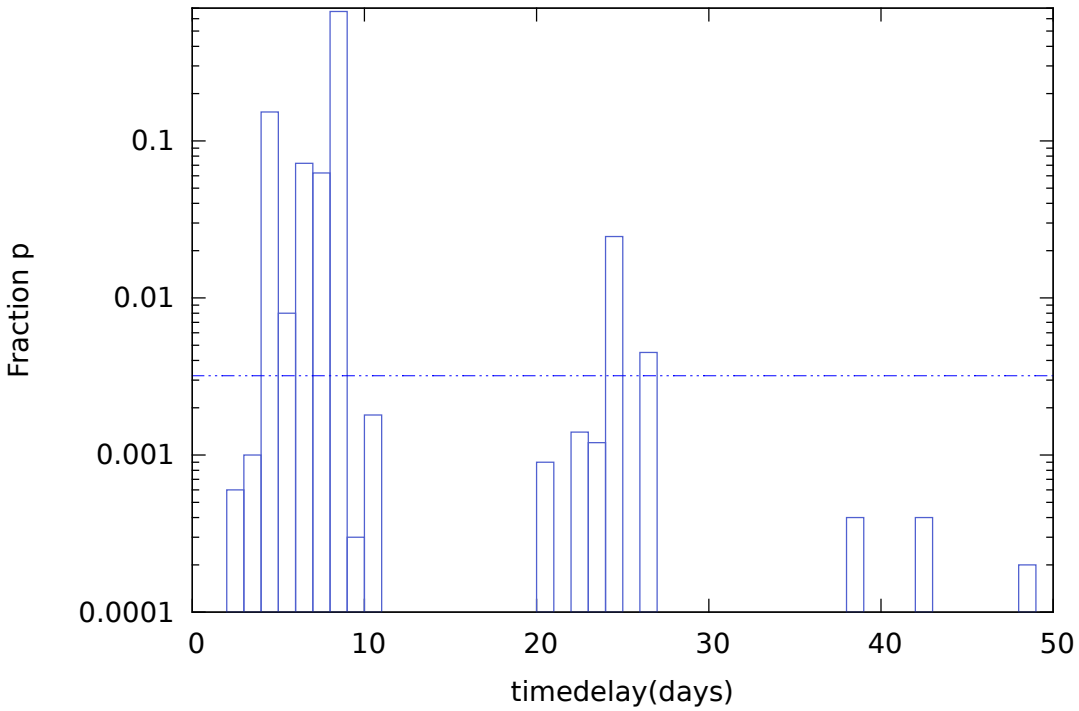

Figure 8.5: Distribution p for time delays between $0-50$ days based on our light curves of components A_V, B_V and B_R. The probability has been computed from 10000 bootstrap resamplings of the observed light curves. For each resampling the brightest component A has been interpolated in correspondence to the dates at which B has been observed. The region above the dashed line contains 95% of the statistical weight. Mean value and standard deviation of this region are $\Delta t = 7.6 \pm 2.9$ days.

$$\omega_{i,j} = \frac{1 - \frac{|t_i - t_j|}{\delta}}{\sigma_{mj}^2}, \tag{8.1}$$

where σ_{mj} indicates the Poissonian noise corresponding to the magnitude m_j observed at the epoch t_j.

4. From the resulting light curves, comprising N epochs, we computed the weighted magnitude difference between the components Δm and determined the χ^2_ν

$$\chi^2_\nu = \frac{1}{N-2} \sum_{1}^{N} \frac{(m_A(t_i) - m_B(t_i + \Delta t) - \Delta m)^2}{{\sigma_{mA}}^2 + {\sigma_{mB}}^2}, \tag{8.2}$$

where t_i is the generic time at which data has been collected. σ_{mA} and σ_{mB} are the Poissonian noise propagated through the interpolation formula for $m_A(t_i)$ and the Poissonian noise corresponding to $m_B(t_i + \Delta t)$, respectively.

5. The time delay corresponding to the minimum χ^2_ν was the optimal time delay at any given resampling (see [54]).

It turned out that only in year 2008 the light curves of components A and B were characterized by an intra-seasonal (intrinsic) variation feature useful for the purpose of determining the time delay between the two components. Moreover, the overall A and B light curves did not differ simply by an additional constant, since their difference increased as a function of time. By inspection of Fig. 8.1 we noticed that the variation of component A_R differed from that of components A_V,B_V and B_R. The algorithm was applied at first to the light curve couple $A_V B_V$. The probability distribution of time delays obtained by using this method is plotted in Fig. 8.4. The probability of each 1-day bin was calculated as the ratio between the occurence of light curves with best-fitting time delay in that bin and the total number of resamplings. This procedure also included a peak at 0-day lag as result, possibly a spurious peak deriving from correlated brightness fluctuations at 0 lag. This correlation effect appears when dealing with optical discrete data, as already reported by [154] and by [23], which described it as a *frame-to-frame correlation error in the photometry*. We computed, for the region above the dashed line, carrying 95% of the statistical weight of the distribution (not taking into account the peak at 0 lag), the mean time delay and the standard deviation, obtaining $\Delta t = 7.6 \pm 1.8$ days. In order to assess whether the distribution at 0 lag corresponded to a spurious peak, we applied the above algorithm to the light curve couple $A_V B_{VR}$, where B_{VR} is the average of the light curves of component B in both filters. The aim was to break the correlation at 0 lag between the multiple photometric data recorded on a single frame (in a given filter). Although it is not strictly clear whether this can

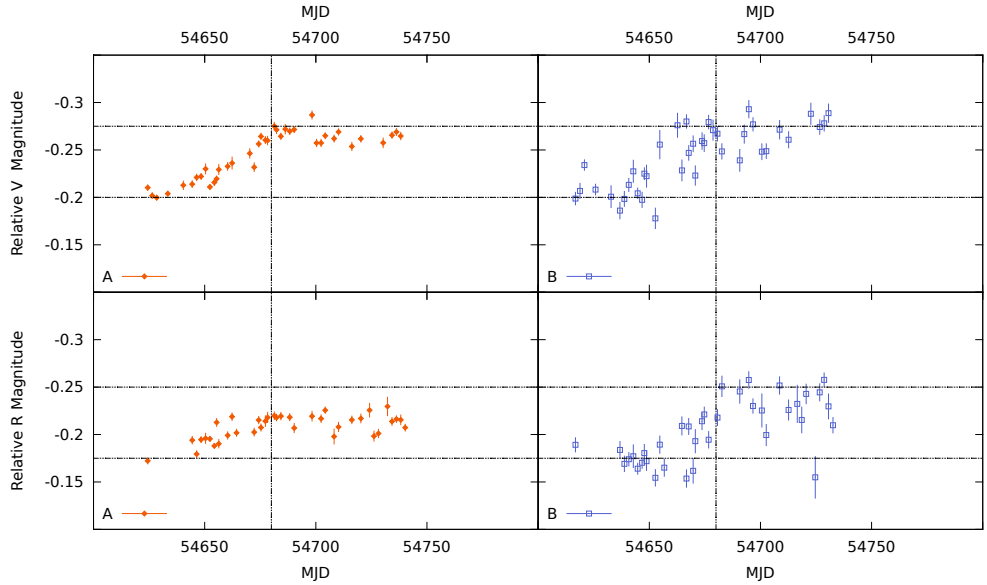

Figure 8.6: V- (upper panels) and R- (bottom panels) band light curves of HE 0047-1756 in 2008. Components A (diamonds) and B (squares) are depicted in orange and blue, espectively. Image B light curve has been shifted backwards along the MJD-axis by a time delay of 7.6 days and along the mag-axis by the average magnitude offset to A in 2008 ($\Delta m_V = -1.45$, $\Delta m_R = -1.41$). The figure is intended to highlight the different variation amplitude shown by component A in the R band, which constitutes a complication in the time delay determination.

be done since interband time delays have been measured for several non-lensed quasars [76] as due to light travel time differences between two different emission regions (and the above analysis on the full light curves in the R band did not converge to a unique result), the procedure led to a time delay distribution (shown in Fig. 8.5), with no peak at 0 lag, whose 95% statistical weight region is described by a mean time delay and standard deviation of $\Delta t = 7.6 \pm 2.9$ days. Therefore we conclude that the time delay analysis carried out by taking into account the year 2008 only in the V band produces a result consistent with the above analysis including the full light curves.

In Fig. 8.6 we show the quasar A and B light curves after shifting image A ahead by 7.6 days and image B up by the appropriate magnitude offset matching the light curves in 2008 ($\Delta m_V = -1.45$ in the V band and $\Delta m_R = -1.41$ in the R band). As stated above image A in the R band varied differently than the other images with a variation amplitude smaller by a factor ~ 2. In Fig. 8.7 we show the difference between

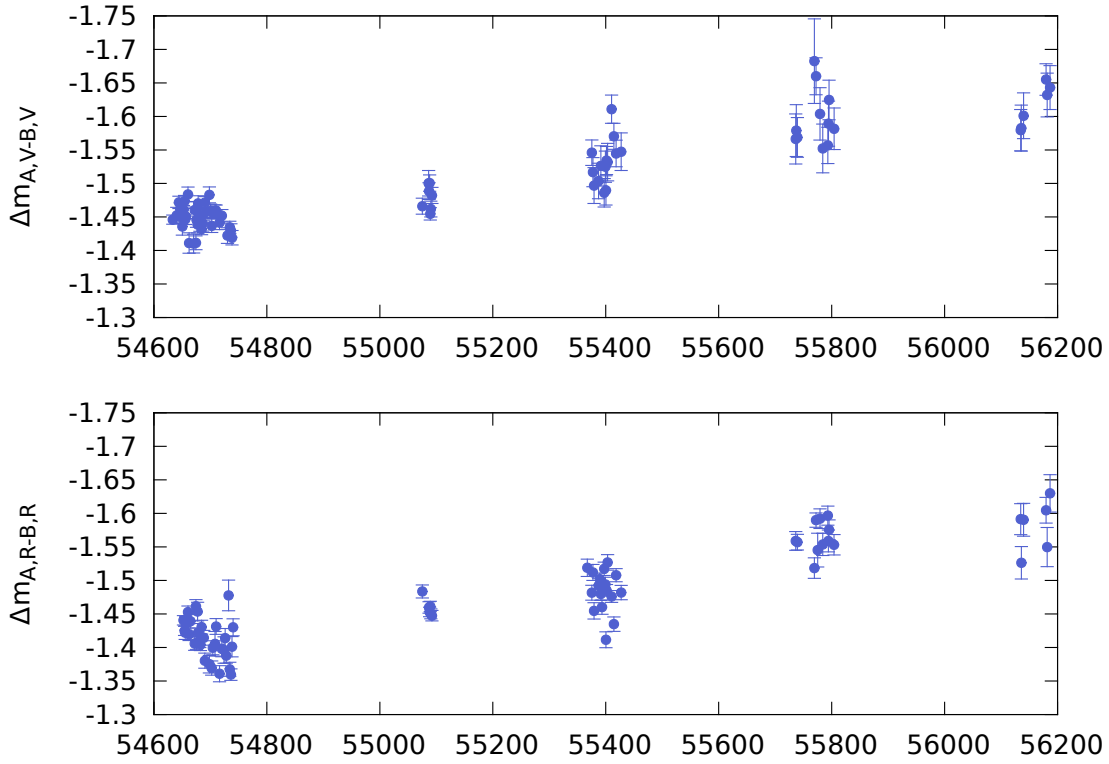

Figure 8.7: Difference between the light curves of HE 0047-1756 components A and B after shifting component A ahead by 7.6 days. Component A is interpolated at the epochs of component B before subtraction.

the light curves of components A and B in both filters. The error bars involved in the

difference computation were added in quadrature. From these plots it can be seen a secular evolution of the magnitude difference between the quasar components by ≈ 0.2 mag across the 5 periods, which is mainly linear and we explain it as due to a long-term microlensing perturbation. Such a behaviour has already been observed for the double quasar SBS 1520+530 by [54].

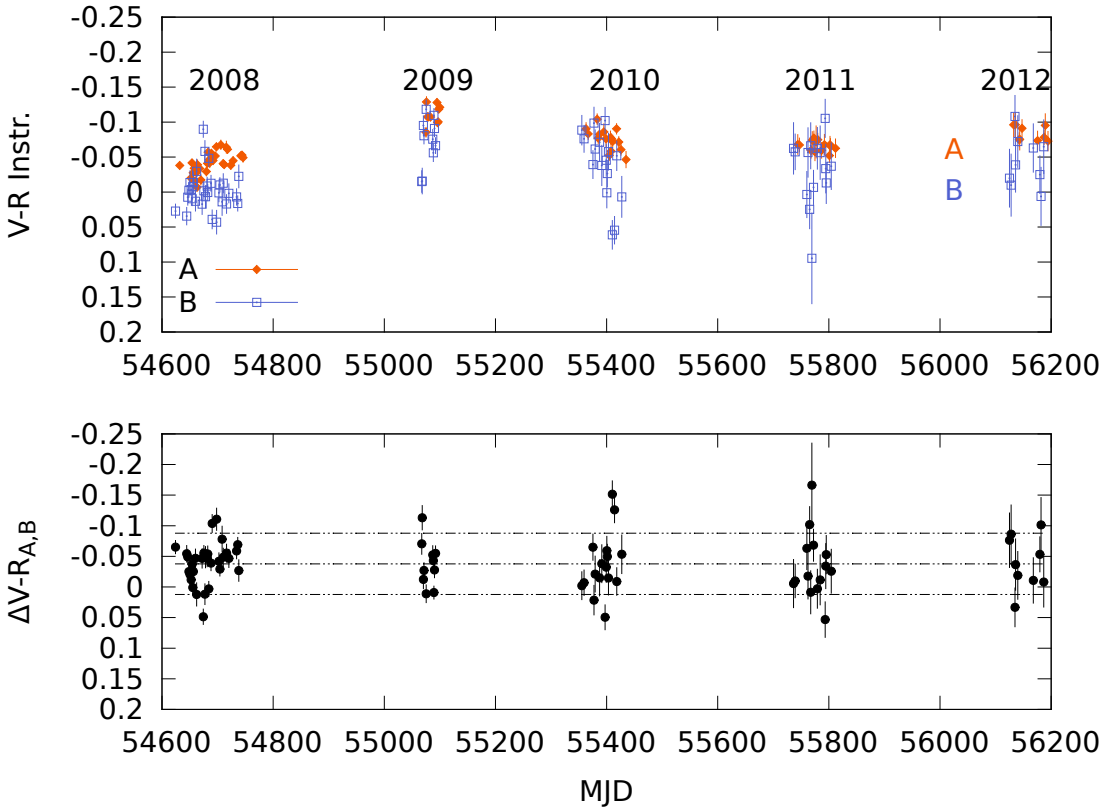

Figure 8.8: $(V-R)_{Instr.}$ light curves of HE 0047-1756 from 2008 to 2012. Components A (diamonds) and B (squares) are depicted, respectively, in orange and blue in the first upper panel. In the bottom panel we show how the color difference between the two components evolves. The difference is computed by interpolating the magnitude of the brightest component in the pair in correspondence to the dates at which the weakest one has been observed. The horizontal dashed lines define ±0.05 intervals around the average color difference.

An analysis of the color index $V-R_{Instr.}$ light curve as a function of the MJD, shown in the upper part of Fig. 8.8, reveals that the two components spanned the highest color variation of ≈ 0.07 mag between seasons 2008 and 2009, with both images turning bluer

in correspondence to the 2009 brightnening of the quasar, as already observed by [157], [116], [125], [124]. The yearly averages of the color are shown in Table 8.3.

Table 8.3: Yearly averages of the instrumental color $V-R_{Instr.}$ for the two lensed components of quasar HE 0047-1756.

	2008	2009	2010	2011	2012
$(V-R)_{Instr.A}$	-0.04 ± 0.02	-0.11 ± 0.01	-0.08 ± 0.02	-0.07 ± 0.01	-0.08 ± 0.01
$(V-R)_{Instr.B}$	0.00 ± 0.03	-0.07 ± 0.04	-0.04 ± 0.05	-0.03 ± 0.05	-0.04 ± 0.04

Table 8.4: Yearly average differences of the instrumental color $V-R_{Instr.}$ between components A and B of quasar HE 0047-1756.

	2008	2009	2010	2011	2012
$\overline{\Delta(V-R)_{Instr.}}$	-0.04 ± 0.04	-0.03 ± 0.03	-0.05 ± 0.05	-0.04 ± 0.06	-0.03 ± 0.04

The color difference between the quasar images was mainly constant ≈ 0.04 throughout the five seasons, as shown in the bottom panel of Fig. 8.8. We computed the color difference after shifting the color light curve of component A by 7.6 days and linearly interpolating it in correspondence to the observation dates of component B. The error bars involved in the difference computation were added in quadrature. The yearly averages of the color difference are shown in Table 8.4 and are consistent with a constant offset between the color light curves.

9

Q 2237+0305

9.1 Light curves for Q 2237+0305

Figures 9.1 and 9.2 show the light curves of the four components of quasar Q 2237+0305 in the standard *V* and *R* bands. The error bars were determined by using the GALFIT software as explained in paragraph 6.4. Figure 9.1 displays the light curves of components A in fuchsia and pale pink, component B in dark and pale green, component C in navy blue and sky blue, component D in two shades of yellow. The first twelve portions of the light curves, which are depicted using the lighter colors, represent the results of the OGLE campaign from 1997 to 2008, which are available from the OGLE internet archive [1]. We have been able to join up our results with the previous OGLE light curves in 2008, as explained in section 9.2. The last five years of monitoring, corresponding to our data, are displayed in more intense colors and are labelled at the bottom of the plot. The OGLE monitoring first showed, with smooth well sampled light curves, that microlensing is practically going on all the time in all multiple images of the quasar Q 2237+0305. Since the time delays between the quasar components are predicted to be of the order of 1 day, the light curves can be straightforwardly compared. None of the components followed the same variation pattern, which means that microlensing was constantly at work during the OGLE monitoring campaign. This is what we also recorded during the last five seasons of monitoring. In the V band the flux of image A became weaker by ≈ 0.5 mag during our monitoring. Image B became dimmer by ≈ 0.3 mag. Image C flux turned slowly weaker during the first three season, similarly to image B, to become then much brighter between 2011 and 2012 by ≈ 0.8 mag. During the five years of monitoring image D became weaker by ≈ 1.25 mag. So all the components are characterized by more or less dramatic, but independent, variation patterns. The most striking features are seen in image D, which became brighter than image B and C for the first time since the beginning of the OGLE monitoring campaign and then weaker again, as it used to be in the previous monitoring seasons. Additionally, image C became again weaker than image B after the reported high-magnification event in 1999

[1] http://ogle.astrouw.edu.pl/

Table 9.1: Yearly averages of the color $V-R$ for the four lensed components of quasar Q 2237+0305.

	2008	2009	2010	2011	2012
$(V-R)_A$	0.12 ± 0.14	0.04 ± 0.02	0.13 ± 0.04	0.14 ± 0.02	0.15 ± 0.02
$(V-R)_B$	-0.01 ± 0.09	-0.06 ± 0.03	-0.12 ± 0.04	-0.12 ± 0.03	-0.10 ± 0.05
$(V-R)_C$	-0.24 ± 0.26	-0.16 ± 0.08	-0.12 ± 0.10	-0.26 ± 0.13	-0.23 ± 0.04
$(V-R)_D$	0.34 ± 0.16	0.25 ± 0.06	0.27 ± 0.11	0.69 ± 0.10	0.85 ± 0.12

and again brighter in 2012. Figure 9.2 displays the light curves of components A in fuchsia, component B in green, component C in blue, component D in yellow. In the R band image A became fainter by ≈ 0.5 mag, image B weaker by ≈ 0.2 mag and image D by ≈ 0.75 mag. Image C also dimmed by ≈ 0.2 mag until 2011, getting suddenly brighter by more than ≈ 0.5 mag in 2012. While in the V band we were able to join up our light curves with the OGLE data, this was not possible in the R band, because OGLE did not use this filter. In this case we had to model the galaxy on the template image as explained in the following section. By proceeding in this way it was possible to plot the R-band magnitudes in standard magnitudes. The consistency of the obtained magnitudes has been checked by graphically comparing our data to the data collected at the MAIDANAK telescope, for which a plot is available at the observatory webpage [2], as a part of the publication prepared for MNRAS by Vakulik et al. The picture shown in Figure 3.5 has been graphically compared to our light curves in 2008 and we found qualitative agreement between the data.

We used the V- and R-band magnitudes obtained above to compute the $V-R$ color of the quasar images as a function of time (MJD). As we mentioned in Section 7.1, when the color light curves of the quasar images cannot be matched by simply shifting them by a constant, the simplest explanation we can provide is microlensing affecting images in an uncorrelated fashion. As shown in Figure 9.3, the $V-R$ color of component D showed an indipendent variation pattern during the last three seasons, in correspondence to its brightness variation, turning redder by ≈ 0.6 mag, in contrast to the other components. Component A showed a more modest color variation, turning redder by ≈ 0.1 mag. In Figure 9.4 we show how the color difference between the components BA, CA and DA evolves. The error bars of the terms involved in the difference computation were added in quadrature. These plots reveal that, taking the color of component A as a reference, component D behaves differently from the others and significantly turns towards the red. The yearly averages of the color for all the components are shown in Table 9.1.

[2] http://www.astron.kharkov.ua/dip/maindep.htm

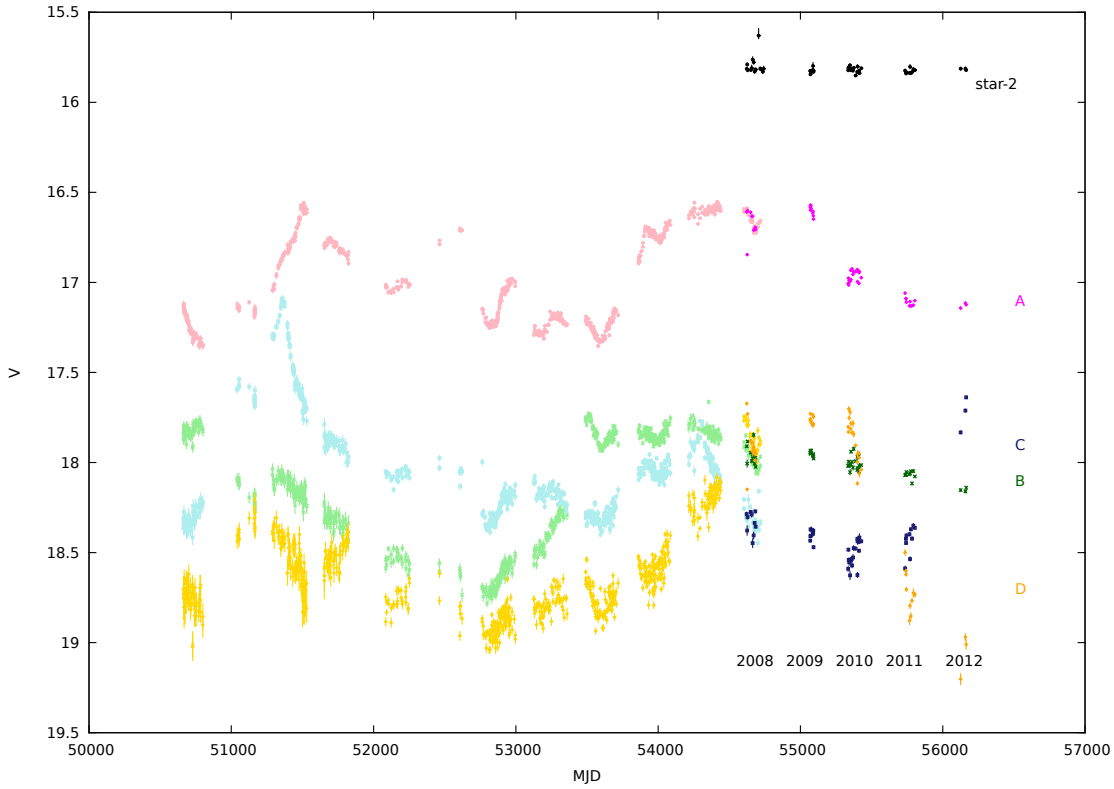

Figure 9.1: V-band light curves of Q 2237+0305 from 2008 to 2012 are shown on the right side of the plot. Components A (filled dots), B (asterisks), C (squares), D (filled diamonds) are depicted in fuchsia, green, blue and yellow, respectively. The light curve of a star in the field, labelled as Const. in Fig. 4.6, is shown in black and shifted by −2 mag. The light curves from the MiNDSTEp campaign have been photometrically joined up with the 12-year-long OGLE data.

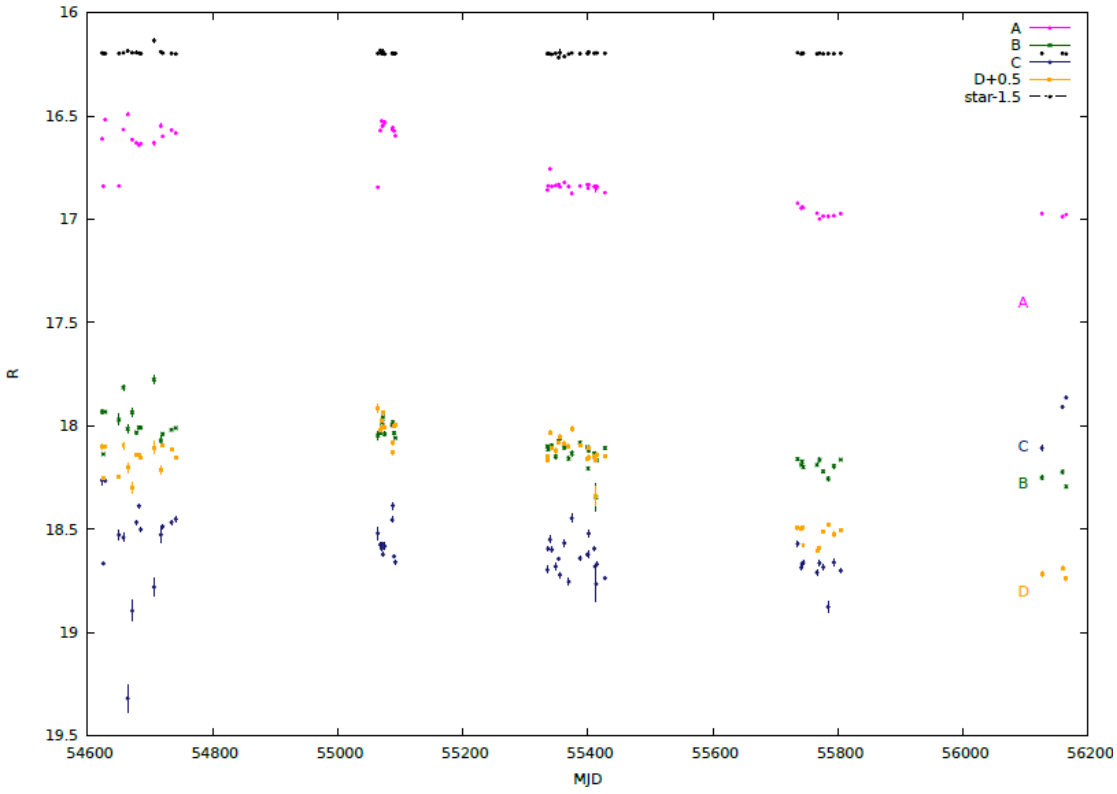

Figure 9.2: R-band light curves of Q 2237+0305 from 2008 to 2012. Components A (filled dots), B (asterisks), C (squares), D (filled diamonds) are depicted in fuchsia, green, blue and yellow, respectively. The light curve of component D is shifted by +0.5 mag. The light curve of a star in the field, labelled as Const. in Fig. 4.6, is shown in black and shifted by −1.5 mag.

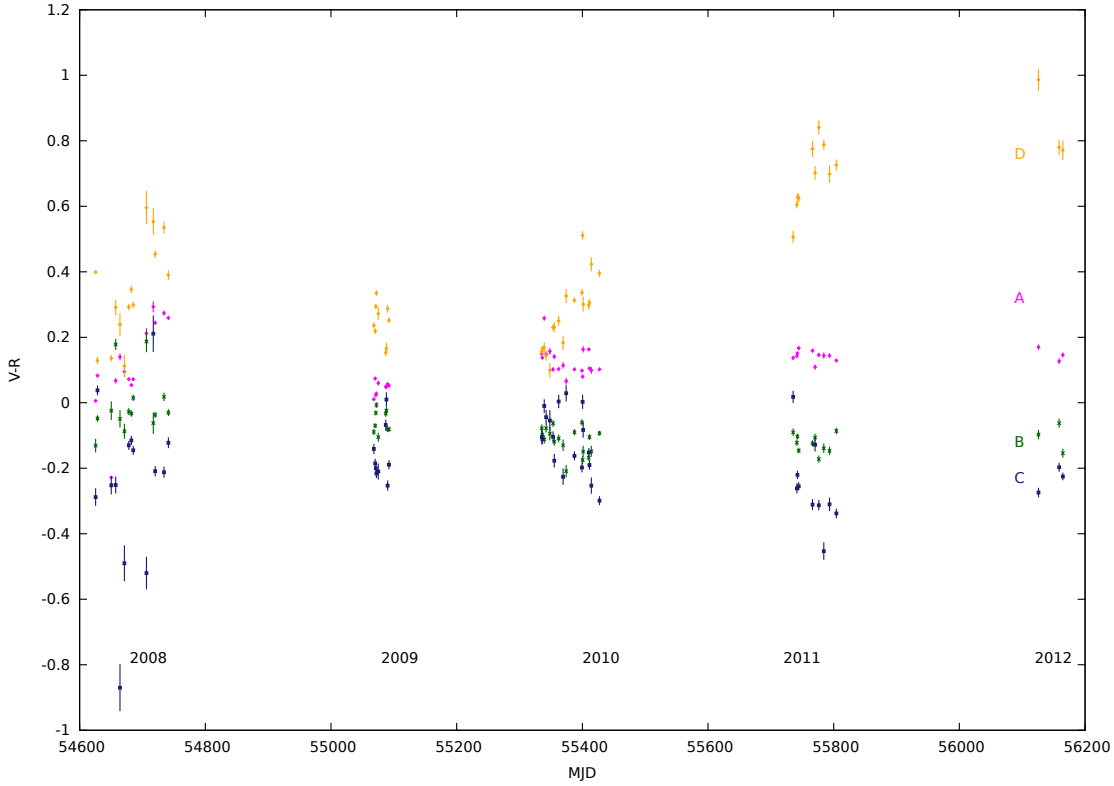

Figure 9.3: $V-R$ color of the components of the quasar Q 2237+0305 as a function of the MJD. Components A (filled dots), B (asterisks), C (squares), D (filled diamonds) are depicted in fuchsia, green, blue and yellow, respectively. The years in which data were collected appear at the bottom of the figure.

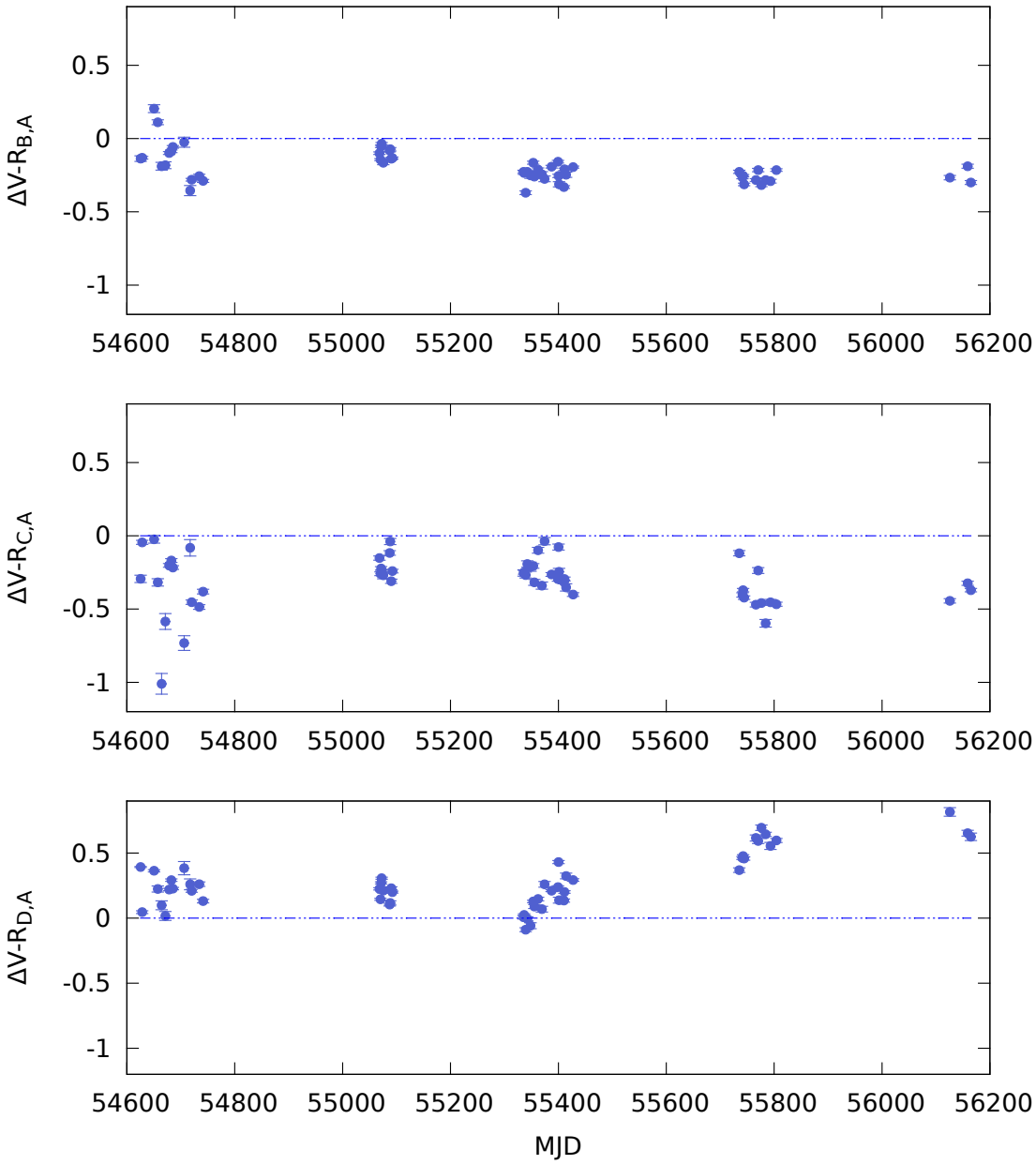

Figure 9.4: Differences of the $V-R$ colors of the component pairs BA, CA and DA of the quasar Q 2237+0305 as a function of the time (MJD).

9.2 Q 2237+0305 standard photometry: modeling the galaxy on the R-band template

The measurement of the flux for the template image $F_{X,T}$, which is necessary to calculate the magnitude as in equation 7.1, was calculated by neglecting the presence of the weak lensing galaxies in the case of WFI 2033-4723 and HE 0047-1756. This was no longer possible in the case of Q 2237+0305, whose lens is a barred spiral galaxy with an average magnitude of ≈ 15 mag in the optical bands ([177], [135], [127]). In the V band, our approach consisted in avoiding the galaxy modeling. Since in our images the galaxy is not well resolved, an attempt to fit a model to the galaxy has generally been regarded as the last resort. The OGLE light curves in the V band are public and their standard photometry was obtained by modeling the galaxy on HST images of the lens, as explained in [173]. Therefore, we opted for simply joining our light curves to the OGLE light curves. This was possible by noticing that, at any given night, the unknown flux of image i on the template is related to the corresponding image magnitude m_{Ai}, measured by OGLE, by the following relation

$$A_i + \delta A_i = A_\alpha 10^{\frac{m_\alpha - m_{Ai}}{2.5}} \tag{9.1}$$

where $A_i + \delta A_i$ is the sum of the flux on the template and the differential flux computed at that night, A_α the number of counts per second of the α star showed in Fig. 4.6, and m_α its magnitude, fixed at 17.5 mag according to [173]. We chose a good seeing night, common to our data and the OGLE campaign, and corresponding to a Modified Julian Date (MJD) of 54685.3 days. Substituting the values corresponding to each quasar image in the previous formula, we obtained, for each of them, the number of counts per second A_i for the template image. This allowed to translate our differential fluxes into total magnitudes, as those used for the OGLE light curves. The magnitude of the star α, m_α, and its flux at the chosen night provided the zero point needed to join the data.

On the other hand, in the R band, we could not compare our data with any other published light curves. So we chose to model the lensing galaxy of the quasar Q 2237+0305 by using the GALFIT software. The model consisted of:

1. The four point-like images of the quasar. The system geometry was fixed as outlined in Table 6.1. The position of one image was allowed to vary together with the fluxes of the four images.

2. A galactic exponential disk profile component.

3. A de Vaucouleurs' profile for the galactic bulge.

These choices are based on the evidence that a disk galaxy is a composite system well described by a combination of an exponential disk and a de Vaucouleurs' bulge profile.

A de Vaucouleurs' profile contributes to describing the surface brightness of an elliptical galaxy and can be written as a function $B(r)$ of the distance r from the center, as follows

$$B(r) = I_e e^{-7.67[(\frac{r}{Re})^{1/4}-1]} \tag{9.2}$$

where I_e is the surface brightness at the radius R_e, which encloses the disk region contributing to half of the galaxy brightness. This is a special case of Sersic's law, where the Sersic's index is fixed at n=4. The exponential disk component $I(r)$ typically describes the profile of disk galaxies at large radii and has the shape

$$I(r) = I_o e^{(-\frac{r}{R_o})} \tag{9.3}$$

where I_o represents the surface brightness of this component at the center of the disk and R_o is the exponential scale length.

For both the exponential disk and the de Vaucouleurs' profile components, the input parameters were the disk ellipticity, measured on the image and fixed at 0.65, and the PA, the position angle describing the orientation of the disk major axis, fixed at 58.36 degrees towards the right, as seen in Figure 4.6. Both the parameters were measured by using simple graphic tools of the package ds9. For both profiles the central position was left free, together with the profile scales R_e and R_o and the total profile magnitudes. The result of the fit is summarized in Table 9.2.

By adding the fluxes on the template image to the differential fluxes computed for each night and by making use of the standard magnitude for the star α in the R band (R_{alpha} = 17.28 mag according to [25]), it was possible to plot the light curves in standard magnitudes. The best fit model that we used is far from being accurate, since the lensing galaxy in Q 2237+0305 shows an important bar component that cannot easily be modeled with simple galaxy model profiles. Nevertheless in quasar microlensing the relative flux variations between the quasar components are the prime focus of interest and obtaining the light curves in standard magnitudes does not add any fundamental detail to our knowledge of microlensing, and can be regarded as a refining exercise.

Table 9.2: The table summarizes the best fit model parameters for the lensing galaxy of the system Q 2237+0305 in the R band. The labels x_{index}, y_{index} represent the central position of the brightness profiles. The letters A, B, C ,D stand for the flux of the quasar components on the R-band template image, M_{index} indicates the integrated instrumental magnitudes of the brightness profiles.

x_A	777.4 px
y_A	679.3 px
A	1477 counts/s
B	450 counts/s
C	278 counts/s
D	641 counts/s
x_{deVac}	776 px
y_{deVac}	681 px
M_{deVac}	16.4 mag
R_e	4.7 px
x_{exp}	776 px
y_{exp}	682 px
M_{exp}	15.5 mag
R_o	10.4 px
χ^2	42

10 Summary and conclusions

10.1 Summary

We have presented *V*-band and *R*-band photometry of the gravitational lens systems WFI 2033-4723, HE 0047-1756 and Q 2237+0305 from 2008 to 2012. Data were collected by the MiNDSTEp collaboration with the Danish 1.54 m telescope at La Silla, Chile. By applying the Alard & Lupton image subtraction method ([9], [8]), as implemented in the HOTPAnTS software, we have constructed the light curves of the multiple images of the quasars.

1. The lensed images of the quasar WFI 2033-4723 varied by ≈ 0.6 mag in the V band and ≈ 0.5 mag in the R band during the campaign, becoming brighter in 2009 and gradually weaker until 2012. After computing the A2-A1, B-A1, C-A1 light curves, we found that C-A1 showed a variation of ≈ 0.2 mag in the R band across the period 2008-2011. We suggest that microlensing affecting only the outer part of the accretion disk of image C could in principle explain the behaviour seen in the R band. This relies on the hypothesis that an outer and hence cooler part of the disk, with emission at longer wavelengths, is magnified by the caustic pattern.

2. The two lensed components of quasar HE 0047-1756 reached their maximum brightness in 2009 and again in 2012, with a magnitude variation of $\approx 0.2 - 0.3$ mag. We were able to provide a measurement of the time delay between the two components of this system for the first time. We applied the PyCS software by [147] to our whole V-band and R-band dataset. The free-knot spline technique and dispersion technique provided in the V-band consistent estimates of the time delay of 7.2 ± 3.8 and 8.0 ± 4.2 days. In the R-band the methods did not converge to a unique result. By making use of a linear-interpolation scheme applied to the brightest component A (see [54]), we carried out a zoom-in analysis on 2008 and determined the time delay value minimizing the magnitude difference between

the light curves A_V and B_V. We found out that component B is delayed with respect to A by $\Delta t = 7.6 \pm 1.8$ days. In order to verify the spurious nature of a 0 lag peak, included as a possible result in the above zoom-in analysis, we applied the linear-interpolation scheme to the light curves A_V and B_{VR}. The latter is the average of the light curves B_V and B_R in 2008. We estimated the corresponding time delay at $\Delta t = 7.6 \pm 2.9$ days. Therefore, we conclude that the time delay analysis carried out by taking into account only the year 2008 in the V band produces a result consistent with the analysis including the full light curves. The magnitude difference between the light curves of A and B in both bands increased from 2008 to 2012 by ≈ 0.2 mag, showing a long-term linear uncorrelation between the two components, which can be explained with a long-term microlensing perturbation. The images of quasars WFI 2033-4723 and HE 0047-1756 became bluer when getting brighter. This is consistent with previous studies (e.g. [157]). A possible explanation to this finding is obtained by considering the accretion disk models for quasars. A boost in the disk accretion rate could produce a temperature increase of the inner regions of a quasar, hence a brighter and bluer emission. The color difference between the components of each quasar is consistent with being constant across the five periods.

3. In the case of quasar Q 2237+0305 we were able to compute the photometry in standard magnitudes, joining up our curves with the OGLE ones in the V band and recurring to modeling the lensing galaxy in the R band. As already demonstrated by the previous monitoring campaigns, all the components of the system showed impressive and uncorrelated variations of flux. In the V band, image A became fainter by ≈ 0.5 mag during the 5-year monitoring. Image B became instead dimmer by ≈ 0.3 mag. Image C flux turned slowly dimmer during the first three season, similarly to image B, to become then much brighter between 2011 and 2012 by ≈ 0.8 mag. Image D dimmed by ≈ 1.25 mag. Hence, all the components showed independent variation patterns. The most striking features are seen in image D, which became brighter than image B and C for the first time since the beginning of the OGLE monitoring and then weaker again, in what appears to be a typical shape of a high-magnification event. Image C became again weaker than image B after the reported high-magnification event in 1999 ($MJD \approx 51400$) and brighter in 2012, in what resembles the ascending portion of another high-magnification event. We found similar variation patterns in the R band. Image A became fainter by ≈ 0.5 mag, image B by ≈ 0.2 mag, image D by ≈ 0.75 mag and image C by ≈ 0.2 mag until 2011, getting suddenly brighter by more than ≈ 0.5 mag in 2012. The computation of the $V - R$ colors of the quasar components indicated that component D became redder by ≈ 0.6 mag, in contrast to the smaller color variations of the other components. Chromatic microlensing might provide an explanation to this finding.

10.2 Conclusions and outlook

This thesis work has focussed on the observation of the quasar microlensing phenomenon in multiply imaged quasars. The relative light curves have been built by making use of the difference image analysis (DIA), arguably the best way of treating variable sources in presence of wide overlapping and non-varying galaxies. The outstanding results obtained with a 1.5 m class telescope, average exposures of 3 minutes and an average seeing of 1.3″, reveals how the technique has a huge potential for investigating an increased number of gravitational systems, with the aim of computing time delays and accessing the spatial structure of distant quasars. The possible development of a more automated software would help meet the requirement of analyzing a larger number of systems in order to build wider statistical samples, from which deducing fundamental astrophysical quantities and scales. Since 2012, no additional quasar monitoring has been going on at the Danish telescope. Nevertheless, a new quasar monitoring campaign has been started at the Las Cumbres Observatory Global Telescope Network (LCOGT) and the method presented above has already been applied to the first data.

11

Appendix A

Photometry of WFI 2033-4723, HE 0047-1756 and Q 2237+0305.

Table 11.1: V-and R-band photometry of HE 0047-1756 , as in Fig. 8.1.

mag A_V	$\sigma_{A,V}$	mag B_V	$\sigma_{B,V}$	mag A_R	$\sigma_{A,R}$	mag B_R	$\sigma_{B,R}$	MJD
-0.21	0.003	1.251	0.007	-0.172	0.003	1.224	0.007	54624.4
-0.202	0.003	1.243	0.008					54626.4
-0.2	0.002	1.216	0.005					54628.4
-0.204	0.002	1.241	0.006					54633.4
-0.213	0.004	1.249	0.011					54640.4
-0.214	0.004	1.264	0.009	-0.194	0.004	1.229	0.009	54644.4
-0.221	0.003	1.251	0.008	-0.179	0.004	1.244	0.008	54646.4
-0.222	0.003	1.237	0.007	-0.195	0.003	1.239	0.007	54648.4
-0.23	0.005	1.222	0.012	-0.196	0.005	1.236	0.012	54650.4
-0.211	0.002	1.245	0.005	-0.195	0.002	1.249	0.006	54652.4
-0.216	0.003	1.252	0.008	-0.188	0.002	1.243	0.006	54654.4
-0.22	0.003	1.225	0.006	-0.213	0.004	1.233	0.009	54655.4
-0.229	0.005	1.227	0.012	-0.19	0.004	1.241	0.01	54656.4
-0.233	0.004	1.272	0.011	-0.199	0.004	1.259	0.009	54660.3
-0.236	0.006	1.194	0.015	-0.219	0.004	1.224	0.009	54662.3
				-0.202	0.004	1.248	0.009	54664.3
-0.246	0.005	1.174	0.013					54670.3
-0.232	0.005	1.221	0.011	-0.203	0.004	1.204	0.009	54672.3
-0.256	0.003	1.17	0.007	-0.215	0.004	1.259	0.009	54674.3
-0.264	0.003	1.203	0.008	-0.207	0.004	1.204	0.008	54675.3
-0.26	0.004	1.193	0.008	-0.214	0.006	1.251	0.013	54677.3
-0.26	0.004	1.227	0.01	-0.218	0.005	1.22	0.012	54678.3
-0.275	0.004	1.19	0.009	-0.22	0.004	1.199	0.009	54681.3
-0.271	0.004	1.192	0.009	-0.218	0.003	1.192	0.008	54682.3
-0.264	0.003	1.17	0.007	-0.219	0.004	1.219	0.009	54684.3
-0.272	0.005	1.179	0.011					54686.3
-0.27	0.003	1.183	0.008	-0.218	0.004	1.195	0.008	54688.3
-0.272	0.003	1.201	0.008	-0.207	0.005	1.162	0.011	54690.3
-0.287	0.004	1.211	0.011	-0.219	0.005	1.168	0.012	54698.3
-0.257	0.004	1.183	0.009					54700.3
-0.257	0.004	1.157	0.009	-0.217	0.004	1.156	0.009	54702.4
-0.265	0.003	1.173	0.007	-0.226	0.003	1.183	0.008	54704.2
-0.262	0.004	1.202	0.008	-0.198	0.008	1.188	0.017	54708.2
-0.269	0.003	1.201	0.008	-0.208	0.005	1.214	0.011	54710.2
-0.254	0.004	1.178	0.01	-0.215	0.004	1.161	0.009	54716.2
-0.262	0.003	1.189	0.009	-0.217	0.005	1.187	0.011	54720.3
				-0.226	0.007	1.181	0.02	54724.2
				-0.198	0.005	1.198	0.013	54726.2
				-0.201	0.004	1.17	0.01	54728.2
-0.257	0.005	1.162	0.011					54730.3
				-0.23	0.01	1.258	0.022	54732.3
-0.266	0.003	1.176	0.008	-0.214	0.004	1.169	0.009	54734.3
-0.269	0.004	1.172	0.008	-0.216	0.003	1.155	0.007	54736.3
-0.265	0.004	1.161	0.01	-0.215	0.005	1.183	0.013	54738.2
				-0.207	0.004	1.203	0.008	54740.2
				-0.344	0.003	1.092	0.006	55066.4
-0.455	0.005	1.03	0.011	-0.37	0.005	1.045	0.011	55067.4
-0.496	0.006	1.053	0.015	-0.367	0.005	1.069	0.011	55068.3

Table 11.1: continued.

mag A_V	$\sigma_{A,V}$	mag B_V	$\sigma_{B,V}$	mag A_R	$\sigma_{A,R}$	mag B_R	$\sigma_{B,R}$	MJD
-0.468	0.005	1.003	0.011	-0.361	0.003	1.098	0.008	55070.3
-0.451	0.004	1.01	0.008	-0.343	0.003	1.09	0.008	55071.4
-0.475	0.004	1.055	0.01					55074.3
-0.478	0.004	0.997	0.011	-0.371	0.003	1.115	0.008	55075.3
-0.488	0.006	1.019	0.019					55086.4
-0.517	0.005	1.007	0.011	-0.389	0.003	1.082	0.008	55087.3
-0.494	0.005	1.018	0.011	-0.394	0.003	1.074	0.006	55088.3
-0.488	0.003	0.971	0.007	-0.388	0.003	1.081	0.007	55089.4
-0.513	0.004	0.977	0.01	-0.395	0.003	1.068	0.006	55090.3
-0.514	0.004	0.996	0.009	-0.393	0.003	1.062	0.006	55092.3
-0.423	0.01	1.067	0.026					55352.4
-0.41	0.008	1.069	0.019	-0.32	0.003	1.158	0.008	55355.4
-0.408	0.007	1.101	0.017	-0.325	0.003	1.177	0.008	55359.4
				-0.293	0.005	1.195	0.013	55367.4
-0.384	0.006	1.15	0.017	-0.28	0.004	1.189	0.01	55375.4
-0.376	0.007	1.124	0.02	-0.299	0.004	1.223	0.011	55377.4
-0.365	0.01	1.107	0.025	-0.283	0.004	1.169	0.011	55379.4
-0.361	0.011	1.139	0.025	-0.275	0.004	1.21	0.01	55387.4
				-0.284	0.003	1.222	0.007	55389.4
-0.346	0.011	1.163	0.028	-0.27	0.003	1.201	0.008	55391.4
				-0.261	0.003	1.183	0.009	55393.4
-0.323	0.007	1.133	0.016	-0.271	0.004	1.236	0.01	55397.3
-0.347	0.008	1.18	0.021	-0.269	0.004	1.226	0.01	55399.4
-0.327	0.008	1.149	0.019	-0.269	0.005	1.148	0.011	55400.4
-0.338	0.006	1.197	0.017	-0.262	0.003	1.223	0.008	55401.4
-0.349	0.008	1.202	0.024	-0.276	0.004	1.26	0.011	55403.4
-0.342	0.007	1.266	0.019	-0.251	0.003	1.205	0.008	55410.4
-0.339	0.006	1.225	0.017	-0.267	0.004	1.17	0.01	55414.4
-0.328	0.007	1.203	0.019	-0.267	0.004	1.255	0.009	55418.3
-0.325	0.011	1.22	0.027	-0.279	0.004	1.213	0.01	55427.3
				-0.314	0.005	1.206	0.013	55723.4
				-0.353	0.005	1.212	0.012	55725.4
-0.422	0.015	1.154	0.041					55726.4
-0.404	0.013	1.149	0.034	-0.336	0.005	1.211	0.013	55736.4
-0.425	0.013	1.163	0.035					55737.4
-0.416	0.009	1.156	0.023	-0.349	0.004	1.214	0.01	55739.4
-0.4	0.01	1.217	0.029	-0.341	0.005	1.213	0.015	55760.4
-0.402	0.011	1.183	0.032	-0.328	0.005	1.24	0.014	55762.4
-0.414	0.009	1.225	0.025	-0.337	0.004	1.2	0.011	55765.4
-0.404	0.012	1.169	0.03	-0.347	0.005	1.235	0.013	55767.3
-0.398	0.022	1.281	0.063	-0.327	0.006	1.186	0.014	55769.4
-0.423	0.009	1.249	0.023	-0.348	0.003	1.255	0.008	55772.4
				-0.366	0.006	1.203	0.025	55775.4
-0.412	0.01	1.186	0.027	-0.353	0.005	1.249	0.013	55779.4
-0.404	0.013	1.136	0.035	-0.336	0.006	1.192	0.015	55784.4
-0.41	0.009	1.152	0.024	-0.358	0.004	1.258	0.013	55793.3
-0.402	0.011	1.184	0.031	-0.335	0.005	1.217	0.015	55794.3
-0.413	0.009	1.218	0.026	-0.347	0.005	1.231	0.013	55795.3
-0.404	0.012	1.17	0.03	-0.342	0.006	1.207	0.014	55804.3

Table 11.1: continued.

mag A_V	$\sigma_{A,V}$	mag B_V	$\sigma_{B,V}$	mag A_R	$\sigma_{A,R}$	mag B_R	$\sigma_{B,R}$	MJD
-0.501	0.011	1.088	0.029	-0.405	0.012	1.107	0.029	56124.9
-0.513	0.014	1.099	0.037	-0.416	0.01	1.109	0.025	56127.9
-0.523	0.008	1.07	0.026	-0.448	0.005	1.178	0.015	56134.8
-0.525	0.012	1.069	0.032	-0.45	0.009	1.108	0.022	56135.9
-0.545	0.01	1.082	0.03	-0.454	0.007	1.154	0.021	56139.9
-0.533	0.011	1.021	0.029					56164.8
-0.541	0.01	1.033	0.027	-0.467	0.009	1.096	0.021	56167.9
-0.532	0.008	1.117	0.021	-0.454	0.006	1.142	0.017	56179.8
-0.53	0.012	1.096	0.031	-0.435	0.012	1.089	0.028	56181.7
-0.535	0.01	1.11	0.029	-0.462	0.009	1.175	0.025	56186.7

Table 11.2: V- and R- band photometry of WFI 2033-4723 , as in Fig. 7.1.

mag B_V	$\sigma_{B,V}$	mag $A1_V$	$\sigma_{A1,V}$	mag $A2_V$	$\sigma_{A2,V}$	mag C_V	$\sigma_{C,V}$	mag B_R	$\sigma_{B,R}$	mag $A1_R$	$\sigma_{A1,R}$	mag $A2_R$	$\sigma_{A2,R}$	mag C_R	$\sigma_{C,R}$	*MJD*
2.003	0.006	1.43	0.007	2.015	0.011	2.31	0.009	2.073	0.007	1.456	0.008	2.01	0.013	2.296	0.009	54623.4
1.979	0.004	1.461	0.006	1.985	0.008	2.273	0.005	2.056	0.002	1.473	0.002	1.99	0.002	2.286	0.002	54625.4
1.988	0.004	1.456	0.006	2.006	0.009	2.306	0.007	2.064	0.002	1.459	0.002	1.997	0.003	2.291	0.002	54627.4
1.994	0.006	1.444	0.007	2.039	0.01	2.295	0.008	2.056	0.004	1.454	0.003	2.008	0.005	2.293	0.004	54629.4
2.026	0.01	1.454	0.016	2.003	0.025	2.305	0.015	2.056	0.007	1.48	0.008	1.988	0.012	2.267	0.01	54641.4
2.021	0.008	1.397	0.009	2.048	0.013	2.319	0.009	2.088	0.004	1.443	0.004	2.039	0.005	2.298	0.004	54645.4
2.047	0.005	1.439	0.006	2.025	0.008	2.354	0.006	2.085	0.004	1.46	0.003	1.998	0.005	2.304	0.003	54647.4
2.051	0.007	1.431	0.008	2.029	0.013	2.363	0.009	2.093	0.006	1.461	0.007	2	0.012	2.29	0.008	54649.4
2.06	0.007	1.385	0.009	2.046	0.014	2.385	0.01	2.085	0.005	1.436	0.006	2.03	0.009	2.31	0.006	54651.4
2.021	0.017	1.473	0.03	1.99	0.046	2.387	0.029									54653.4
2.071	0.008	1.396	0.009	2.05	0.013	2.359	0.01	2.092	0.004	1.459	0.003	1.996	0.004	2.313	0.004	54655.4
2.037	0.011	1.49	0.015	1.91	0.022	2.366	0.016	2.117	0.011	1.473	0.014	1.976	0.021	2.316	0.015	54657.4
2.051	0.009	1.421	0.009	2.022	0.013	2.356	0.012	2.123	0.009	1.453	0.008	2.001	0.011	2.292	0.01	54661.3
2.038	0.009	1.426	0.013	2.062	0.022	2.337	0.013	2.106	0.009	1.457	0.014	2.028	0.022	2.328	0.013	54671.3
2.04	0.009	1.404	0.01	2.123	0.018	2.39	0.012	2.084	0.011	1.449	0.013	2.046	0.021	2.319	0.015	54674.3
2.043	0.007	1.441	0.009	2.075	0.013	2.344	0.009	2.078	0.007	1.464	0.008	2.047	0.012	2.296	0.008	54675.3
2.041	0.006	1.482	0.007	2.021	0.01	2.36	0.008	2.083	0.006	1.493	0.007	2.034	0.009	2.303	0.006	54677.3
1.962	0.022	1.469	0.038	2.076	0.066	2.37	0.038									54679.3
2.014	0.014	1.432	0.015	2.057	0.022	2.339	0.019	2.07	0.006	1.5	0.007	1.988	0.009	2.3	0.007	54681.3
2.011	0.008	1.533	0.01	2.007	0.014	2.284	0.009	2.082	0.006	1.535	0.008	1.986	0.01	2.279	0.008	54683.3
2.008	0.006	1.529	0.008	2.023	0.011	2.327	0.007	2.079	0.006	1.523	0.007	2.022	0.01	2.29	0.008	54685.3
2.013	0.004	1.519	0.007	2.043	0.01	2.364	0.008	2.043	0.011	1.499	0.011	2.099	0.017	2.293	0.013	54687.3
1.995	0.009	1.533	0.011	2.028	0.015	2.35	0.013	2.059	0.009	1.49	0.01	2.033	0.015	2.31	0.012	54699.3
2.012	0.01	1.519	0.013	2.03	0.019	2.427	0.014	2.069	0.008	1.515	0.01	2.031	0.016	2.288	0.011	54703.3
2.043	0.008	1.552	0.011	1.975	0.015	2.341	0.011	2.069	0.008	1.495	0.01	2.027	0.015	2.315	0.011	54705.3
1.999	0.011	1.501	0.018	1.998	0.028	2.378	0.018	2.07	0.012	1.529	0.016	1.965	0.023	2.326	0.016	54715.2
1.997	0.008	1.462	0.01	2.024	0.014	2.334	0.011	2.056	0.009	1.514	0.01	1.975	0.013	2.339	0.011	54717.2
1.985	0.012	1.473	0.013	1.992	0.02	2.379	0.017	2.086	0.009	1.46	0.01	2.069	0.016	2.353	0.013	54728.2
2.044	0.014	1.519	0.022	1.942	0.03	2.393	0.024	2.075	0.011	1.525	0.015	1.949	0.021	2.263	0.016	54729.2
2.012	0.006	1.47	0.006	2.003	0.008	2.363	0.008	2.062	0.005	1.488	0.006	2	0.008	2.316	0.006	54731.2
2.025	0.005	1.461	0.007	2.048	0.011	2.391	0.008	2.054	0.005	1.489	0.007	2.003	0.01	2.333	0.007	54733.2
2.024	0.012	1.498	0.017	2	0.026	2.376	0.018	2.057	0.015	1.491	0.023	2.061	0.038	2.289	0.022	54735.1
2.025	0.009	1.528	0.011	2.002	0.016	2.338	0.011	2.081	0.008	1.523	0.012	2.012	0.017	2.309	0.014	54739.1
2.02	0.006	1.481	0.008	2.036	0.012	2.365	0.008	2.048	0.006	1.479	0.007	2.045	0.009	2.332	0.007	54741.1
2.025	0.006	1.507	0.009	2.022	0.012	2.353	0.009	2.055	0.007	1.522	0.009	2.028	0.012	2.293	0.008	54743.1
								1.808	0.01	1.301	0.016	1.771	0.024	2.149	0.017	55001.4
								1.811	0.006	1.296	0.011	1.872	0.018	2.19	0.012	55004.4
								1.816	0.007	1.332	0.012	1.807	0.018	2.188	0.013	55005.4
								1.82	0.008	1.326	0.012	1.82	0.018	2.168	0.013	55006.4
								1.81	0.007	1.303	0.011	1.811	0.017	2.206	0.012	55008.4
1.636	0.006	1.112	0.006	1.718	0.008	2.114	0.008	1.739	0.005	1.168	0.006	1.746	0.008	2.108	0.007	55068.2
1.611	0.007	1.101	0.006	1.703	0.008	2.106	0.009	1.72	0.005	1.175	0.006	1.722	0.007	2.123	0.007	55070.2
1.623	0.005	1.112	0.006	1.693	0.008	2.101	0.007	1.743	0.005	1.203	0.006	1.672	0.007	2.129	0.006	55071.2
1.609	0.006	1.099	0.006	1.712	0.009	2.079	0.007	1.699	0.006	1.201	0.006	1.675	0.008	2.117	0.006	55072.2
								1.734	0.013	1.169	0.02	1.709	0.032	2.175	0.027	55075.2
								1.724	0.018	1.111	0.026	1.76	0.045	2.248	0.038	55076.2
1.629	0.007	1.07	0.008	1.667	0.013	2.124	0.009	1.737	0.007	1.113	0.007	1.761	0.011	2.121	0.008	55087.2
1.641	0.007	1.067	0.007	1.645	0.009	2.106	0.008	1.74	0.005	1.144	0.006	1.69	0.009	2.109	0.007	55088.2

Table 11.2: continued.

mag B_V	$\sigma_{B,V}$	mag $A1_V$	$\sigma_{A1,V}$	mag $A2_V$	$\sigma_{A2,V}$	mag C_V	$\sigma_{C,V}$	mag B_R	$\sigma_{B,R}$	mag $A1_R$	$\sigma_{A1,R}$	mag $A2_R$	$\sigma_{A2,R}$	mag C_R	$\sigma_{C,R}$	MJD
1.646	0.007	1.104	0.007	1.64	0.011	2.084	0.008	1.75	0.007	1.146	0.007	1.697	0.011	2.102	0.009	55089.2
1.65	0.009	1.097	0.012	1.622	0.019	2.085	0.014	1.737	0.01	1.15	0.014	1.68	0.021	2.147	0.016	55091.2
1.64	0.005	1.068	0.006	1.654	0.008	2.068	0.007	1.718	0.005	1.146	0.007	1.698	0.009	2.09	0.007	55092.2
1.857	0.007	1.139	0.008	1.788	0.011	2.187	0.01	1.912	0.007	1.218	0.007	1.758	0.009	2.193	0.007	55325.4
1.865	0.007	1.176	0.008	1.756	0.012	2.133	0.009	1.911	0.007	1.237	0.009	1.749	0.012	2.15	0.01	55334.4
1.872	0.005	1.166	0.006	1.784	0.009	2.152	0.007	1.923	0.007	1.256	0.007	1.769	0.009	2.159	0.007	55336.4
1.861	0.007	1.143	0.009	1.806	0.014	2.15	0.011	1.9	0.008	1.223	0.009	1.8	0.014	2.161	0.011	55339.4
1.897	0.006	1.284	0.009	1.733	0.012	2.106	0.007	1.971	0.008	1.281	0.009	1.769	0.014	2.148	0.01	55341.4
1.924	0.007	1.272	0.007	1.765	0.01	2.151	0.006	1.981	0.008	1.279	0.008	1.834	0.01	2.188	0.008	55352.4
1.932	0.007	1.237	0.01	1.861	0.016	2.234	0.013	1.998	0.008	1.358	0.01	1.705	0.012	2.208	0.011	55354.4
1.95	0.009	1.283	0.011	1.798	0.016	2.174	0.012	2.007	0.006	1.31	0.009	1.795	0.013	2.183	0.01	55358.3
1.939	0.007	1.262	0.008	1.813	0.012	2.18	0.009	1.996	0.006	1.342	0.008	1.762	0.011	2.192	0.008	55362.3
1.946	0.007	1.251	0.007	1.859	0.012	2.154	0.007	1.99	0.006	1.337	0.008	1.783	0.011	2.177	0.008	55365.3
1.94	0.008	1.296	0.01	1.83	0.016	2.195	0.01	2.013	0.012	1.319	0.013	1.846	0.019	2.181	0.015	55368.4
1.891	0.008	1.321	0.009	1.872	0.013	2.176	0.011	1.971	0.009	1.363	0.008	1.811	0.011	2.202	0.01	55378.4
1.9	0.006	1.293	0.008	1.837	0.012	2.218	0.01	1.972	0.007	1.316	0.009	1.848	0.012	2.242	0.01	55380.3
1.933	0.009	1.325	0.01	1.868	0.016	2.248	0.012	1.966	0.006	1.345	0.01	1.881	0.016	2.28	0.01	55384.4
1.879	0.006	1.342	0.009	1.798	0.011	2.209	0.007	1.956	0.006	1.331	0.009	1.863	0.012	2.208	0.01	55386.4
								1.992	0.009	1.393	0.011	1.82	0.015	2.216	0.011	55390.4
2.021	0.011	1.604	0.014	1.827	0.016	2.192	0.012	1.975	0.006	1.402	0.008	1.825	0.011	2.2	0.009	55392.3
1.84	0.011	1.425	0.016	1.863	0.024	2.314	0.017	1.939	0.017	1.402	0.028	1.909	0.044	2.213	0.025	55396.3
1.895	0.011	1.368	0.014	1.921	0.022	2.219	0.018	1.961	0.009	1.388	0.01	1.857	0.014	2.23	0.012	55399.3
1.84	0.008	1.363	0.009	1.864	0.012	2.248	0.011	1.955	0.008	1.365	0.008	1.887	0.01	2.252	0.008	55408.3
1.841	0.005	1.351	0.009	1.884	0.014	2.284	0.01	1.946	0.007	1.367	0.008	1.856	0.012	2.263	0.009	55410.3
1.847	0.006	1.343	0.009	1.881	0.013	2.296	0.011	1.947	0.008	1.384	0.01	1.89	0.015	2.293	0.012	55411.3
1.839	0.02	1.475	0.028	1.654	0.035	2.3	0.036	1.906	0.036	1.329	0.04	1.919	0.066	2.279	0.061	55413.3
1.881	0.007	1.337	0.011	1.853	0.017	2.265	0.012	1.913	0.013	1.374	0.019	1.851	0.028	2.24	0.024	55418.3
1.884	0.007	1.358	0.009	1.814	0.013	2.263	0.01	1.978	0.009	1.359	0.011	1.874	0.017	2.251	0.012	55421.3
1.896	0.008	1.337	0.009	1.809	0.013	2.304	0.011	1.943	0.008	1.324	0.01	1.876	0.015	2.247	0.011	55425.3
1.945	0.007	1.352	0.007	1.909	0.009	2.276	0.007	1.949	0.008	1.366	0.006	1.844	0.008	2.26	0.007	55427.3
2.052	0.008	1.65	0.012	2.088	0.017	2.587	0.015	2.096	0.008	1.548	0.01	2.189	0.017	2.528	0.014	55735.4
2.026	0.006	1.601	0.01	2.156	0.014	2.584	0.012	2.105	0.007	1.603	0.009	2.127	0.012	2.499	0.008	55737.4
2.019	0.008	1.583	0.01	2.128	0.015	2.593	0.013	2.111	0.006	1.641	0.009	2.095	0.012	2.536	0.011	55739.4
2.083	0.007	1.492	0.008	2.073	0.013	2.549	0.012	2.095	0.008	1.536	0.008	2.027	0.011	2.528	0.011	55762.3
2.059	0.008	1.499	0.009	2.11	0.015	2.576	0.014	2.104	0.009	1.557	0.01	1.997	0.014	2.563	0.014	55763.2
2.101	0.017	1.49	0.029	2.018	0.044	2.563	0.031									55772.3
2.248	0.007	1.736	0.012	2.212	0.016	2.676	0.013	2.228	0.01	1.555	0.012	2.213	0.02	2.643	0.018	56164.8
2.17	0.009	1.637	0.012	2.23	0.02	2.668	0.016	2.253	0.01	1.582	0.012	2.366	0.024	2.623	0.017	56179.7

Table 11.3: V- and R- band photometry of Q 2237+0305, as in Fig.9.1 and 9.2.

mag A_V	$\sigma_{A,V}$	mag B_V	$\sigma_{B,V}$	mag C_V	$\sigma_{C,V}$	mag D_V	$\sigma_{D,V}$	mag A_R	$\sigma_{A,R}$	mag B_R	$\sigma_{B,R}$	mag C_R	$\sigma_{C,R}$	mag D_R	$\sigma_{D,R}$	MJD
16.609	0.003	17.909	0.006	18.286	0.010	17.672	0.008									54622.4
								16.611	0.006	17.931	0.011	18.263	0.020	17.598	0.013	54623.4
16.846	0.001	18.005	0.019	18.378	0.025	18.149	0.004	16.840	0.001	18.136	0.002	18.666	0.003	17.750	0.001	54625.4
16.601	0.003	17.883	0.005	18.304	0.009	17.730	0.008	16.518	0.003	17.932	0.005	18.266	0.009	17.601	0.006	54628.4
16.610	0.003	17.946	0.006	18.274	0.008	17.880	0.007	16.839	0.000	17.970	0.027	18.527	0.025	17.745	0.005	54650.4
16.633	0.004	17.991	0.010	18.288	0.014	17.886	0.015	16.566	0.006	17.814	0.012	18.540	0.020	17.594	0.016	54657.4
16.633	0.007	17.966	0.016	18.447	0.024	17.940	0.024	16.493	0.007	18.015	0.019	19.318	0.065	17.701	0.022	54664.3
16.709	0.006	17.847	0.011	18.405	0.019	17.913	0.020	16.614	0.008	17.934	0.017	18.895	0.049	17.801	0.026	54671.3
16.703	0.003	18.005	0.006	18.336	0.007	17.936	0.006	16.631	0.003	18.032	0.007	18.466	0.009	17.643	0.006	54678.3
16.694	0.003	17.974	0.005	18.271	0.008	17.988	0.007	16.641	0.003	18.007	0.006	18.387	0.010	17.642	0.005	54682.3
16.706	0.003	18.024	0.006	18.356	0.008	17.950	0.006	16.634	0.003	18.009	0.006	18.501	0.009	17.651	0.005	54685.3
16.842	0.010	17.963	0.021	18.260	0.021	18.201	0.039	16.630	0.010	17.776	0.023	18.780	0.044	17.605	0.030	54706.3
16.842	0.011	18.009	0.019	18.737	0.036	18.267	0.033	16.549	0.010	18.071	0.025	18.526	0.041	17.714	0.021	54717.3
16.842	0.004	18.002	0.006	18.278	0.010	18.048	0.010	16.598	0.003	18.038	0.005	18.486	0.010	17.594	0.005	54720.2
16.842	0.005	18.036	0.010	18.255	0.012	18.148	0.015	16.568	0.003	18.018	0.005	18.467	0.009	17.613	0.006	54734.2
16.842	0.004	17.980	0.007	18.329	0.011	18.041	0.011	16.583	0.003	18.010	0.005	18.451	0.011	17.651	0.007	54741.2
								16.845	0.001	18.046	0.021	18.519	0.030	17.416	0.018	55064.3
16.581	0.003	17.944	0.006	18.434	0.008	17.758	0.006	16.570	0.003	18.034	0.006	18.575	0.012	17.522	0.005	55068.3
16.598	0.003	17.934	0.004	18.408	0.007	17.729	0.005	16.524	0.002	18.003	0.005	18.593	0.010	17.509	0.005	55070.3
16.572	0.003	17.951	0.005	18.371	0.008	17.767	0.006	16.549	0.002	17.982	0.004	18.570	0.009	17.472	0.004	55071.3
16.572	0.003	17.950	0.005	18.406	0.007	17.766	0.005	16.544	0.002	17.957	0.005	18.622	0.010	17.432	0.004	55072.3
16.589	0.005	17.934	0.009	18.373	0.015	17.779	0.014	16.530	0.004	18.039	0.009	18.582	0.019	17.506	0.011	55075.3
16.615	0.003	17.963	0.005	18.386	0.008	17.736	0.006	16.566	0.003	17.997	0.006	18.454	0.013	17.583	0.008	55087.2
16.605	0.004	17.958	0.006	18.396	0.011	17.794	0.010	16.556	0.005	17.983	0.008	18.386	0.016	17.629	0.012	55088.2
16.630	0.004	17.953	0.006	18.378	0.011	17.786	0.009	16.573	0.002	18.034	0.005	18.631	0.009	17.499	0.005	55090.2
16.649	0.003	17.978	0.005	18.470	0.008	17.747	0.006	16.596	0.002	18.059	0.004	18.658	0.008	17.495	0.004	55092.2
17.007	0.004	18.020	0.006	18.590	0.012	17.803	0.009	16.858	0.004	18.098	0.008	18.696	0.017	17.646	0.010	55335.4
16.977	0.004	18.016	0.006	18.484	0.008	17.830	0.006	16.838	0.002	18.113	0.007	18.594	0.009	17.667	0.005	55336.4
17.014	0.005	17.995	0.007	18.540	0.009	17.702	0.010	16.756	0.004	18.107	0.008	18.550	0.016	17.533	0.010	55339.4
16.990	0.005	18.018	0.008	18.554	0.016	17.752	0.011	16.841	0.003	18.096	0.007	18.598	0.013	17.608	0.008	55342.4
16.994	0.008	18.054	0.014	18.626	0.022	17.719	0.017	16.837	0.006	18.148	0.013	18.680	0.019	17.621	0.013	55348.4
16.934	0.005	18.010	0.008	18.539	0.012	17.813	0.007	16.831	0.003	18.073	0.005	18.643	0.009	17.582	0.004	55353.4
16.984	0.004	17.940	0.007	18.544	0.013	17.782	0.010	16.843	0.004	18.059	0.009	18.721	0.014	17.552	0.010	55355.4
16.925	0.004	17.996	0.007	18.571	0.013	17.834	0.010	16.822	0.004	18.105	0.008	18.567	0.014	17.584	0.008	55362.4
16.955	0.007	18.028	0.013	18.528	0.016	17.782	0.017	16.841	0.004	18.158	0.010	18.754	0.017	17.599	0.009	55369.4
16.941	0.006	17.924	0.010	18.475	0.013	17.843	0.015	16.875	0.006	18.133	0.014	18.447	0.020	17.517	0.013	55374.4
16.941	0.003	17.992	0.005	18.478	0.007	17.904	0.005	16.839	0.002	18.082	0.006	18.64	0.009	17.592	0.004	55387.4
16.930	0.003	18.042	0.007	18.424	0.010	17.997	0.008	16.833	0.002	18.102	0.004	18.622	0.008	17.660	0.005	55399.3
16.930	0.004	18.031	0.007	18.624	0.014	18.117	0.009	16.850	0.004	18.205	0.007	18.621	0.014	17.606	0.007	55400.4
16.996	0.006	17.969	0.012	18.437	0.017	17.954	0.018	16.833	0.005	18.118	0.011	18.520	0.015	17.653	0.011	55401.3
17.005	0.004	17.964	0.006	18.441	0.009	17.948	0.010	16.842	0.003	18.133	0.006	18.593	0.008	17.650	0.007	55410.3
16.946	0.003	18.050	0.005	18.490	0.008	17.974	0.007	16.841	0.003	18.155	0.005	18.680	0.010	17.668	0.006	55411.3
								16.852	0.015	18.345	0.067	18.765	0.085	17.839	0.048	55413.3
16.940	0.008	18.019	0.013	18.416	0.020	18.062	0.019	16.841	0.003	18.167	0.007	18.669	0.011	17.639	0.006	55414.4
16.974	0.003	18.014	0.005	18.437	0.007	18.039	0.007	16.871	0.002	18.107	0.004	18.736	0.009	17.644	0.005	55427.3
17.059	0.004	18.071	0.006	18.588	0.013	18.499	0.015	16.922	0.003	18.161	0.007	18.570	0.012	17.993	0.009	55735.4
17.089	0.004	18.067	0.005	18.424	0.008	18.601	0.008	16.946	0.003	18.189	0.006	18.685	0.011	17.996	0.006	55741.4
17.091	0.003	18.068	0.004	18.447	0.006	18.621	0.008	16.941	0.003	18.172	0.006	18.667	0.009	17.993	0.006	55742.4

Table 11.3: continued.

mag A_V	$\sigma_{A,V}$	mag B_V	$\sigma_{B,V}$	mag C_V	$\sigma_{C,V}$	mag D_V	$\sigma_{D,V}$	mag A_R	$\sigma_{A,R}$	mag B_R	$\sigma_{B,R}$	mag C_R	$\sigma_{C,R}$	mag D_R	$\sigma_{D,R}$	MJD
17.110	0.004	18.052	0.005	18.405	0.008	18.705	0.011	16.943	0.002	18.199	0.005	18.660	0.008	18.080	0.006	55744.4
17.130	0.004	18.065	0.005	18.398	0.009	18.878	0.021	16.971	0.003	18.188	0.006	18.709	0.012	18.103	0.010	55766.3
17.107	0.004	18.059	0.006	18.536	0.011	18.795	0.016	16.998	0.004	18.164	0.008	18.664	0.015	18.094	0.010	55770.4
17.131	0.003	18.048	0.006	18.371	0.008	18.852	0.018	16.985	0.003	18.220	0.007	18.683	0.012	18.012	0.009	55776.3
17.129	0.005	18.116	0.008	18.423	0.010	18.767	0.011	16.985	0.006	18.256	0.010	18.875	0.023	17.979	0.009	55784.3
17.126	0.005	18.048	0.008	18.351	0.011	18.724	0.022	16.983	0.004	18.195	0.009	18.661	0.015	18.025	0.012	55793.3
17.102	0.003	18.077	0.006	18.362	0.007	18.733	0.013	16.973	0.003	18.163	0.006	18.700	0.010	18.007	0.007	55804.3
17.143	0.005	18.153	0.007	17.833	0.008	19.203	0.030	16.972	0.005	18.250	0.011	18.107	0.011	18.217	0.011	56125.9
17.115	0.005	18.160	0.008	17.711	0.008	18.969	0.019	16.988	0.005	18.222	0.010	17.908	0.009	18.189	0.009	56158.8
17.124	0.005	18.140	0.009	17.638	0.008	19.009	0.026	16.977	0.003	18.294	0.008	17.863	0.007	18.239	0.010	56164.8

List of Figures

List of Tables

Bibliography

[1] Book Review: An introduction to active galactic nuclei / Cambridge U Press, 1997. *The Observatory*, 117:314, October 1997.

[2] Book Review: Opticks [CD-ROM] / Octavo. *Astronomy*, 27:106, 1999.

[3] C. Abajas, E. Mediavilla, J. A. Muñoz, P. Gómez-Álvarez, and R. Gil-Merino. Microlensing of a Biconical Broad-Line Region. *ApJ*, 658:748–762, April 2007.

[4] C. Abajas, E. Mediavilla, J. A. Muñoz, L. Č. Popović, and A. Oscoz. The Influence of Gravitational Microlensing on the Broad Emission Lines of Quasars. *ApJ*, 576:640–652, September 2002.

[5] A. A. Abdo, M. Ackermann, M. Ajello, W. B. Atwood, L. Baldini, J. Ballet, G. Barbiellini, D. Bastieri, B. M. Baughman, K. Bechtol, R. Bellazzini, B. Berenji, R. D. Blandford, E. D. Bloom, E. Bonamente, A. W. Borgland, J. Bregeon, A. Brez, M. Brigida, P. Bruel, T. H. Burnett, S. Buson, G. A. Caliandro, R. A. Cameron, P. A. Caraveo, J. M. Casandjian, E. Cavazzuti, C. Cecchi, Ö. Çelik, A. Chekhtman, C. C. Cheung, J. Chiang, S. Ciprini, R. Claus, J. Cohen-Tanugi, S. Colafrancesco, L. R. Cominsky, J. Conrad, L. Costamante, S. Cutini, D. S. Davis, C. D. Dermer, A. de Angelis, F. de Palma, S. W. Digel, E. do Couto e Silva, P. S. Drell, R. Dubois, D. Dumora, C. Farnier, C. Favuzzi, S. J. Fegan, J. Finke, W. B. Focke, P. Fortin, Y. Fukazawa, S. Funk, P. Fusco, F. Gargano, D. Gasparrini, N. Gehrels, M. Georganopoulos, S. Germani, B. Giebels, N. Giglietto, F. Giordano, M. Giroletti, T. Glanzman, G. Godfrey, I. A. Grenier, J. E. Grove, L. Guillemot, S. Guiriec, Y. Hanabata, A. K. Harding, M. Hayashida, E. Hays, R. E. Hughes, M. S. Jackson, Jóhannesson G., S. Johnson, T. J. Johnson, W. N. Johnson, T. Kamae, H. Katagiri, J. Kataoka, N. Kawai, M. Kerr, J. Knödlseder, M. L. Kocian, M. Kuss, J. Lande, L. Latronico, M. Lemoine-Goumard, F. Longo, F. Loparco, B. Lott, M. N. Lovellette, P. Lubrano, G. M. Madejski, A. Makeev, M. N. Mazziotta, W. McConville, J. E. McEnery, C. Meurer, P. F. Michelson, W. Mitthumsiri, T. Mizuno, A. A. Moiseev, C. Monte, M. E. Monzani, A. Morselli, I. V. Moskalenko, S. Murgia, P. L. Nolan, J. P. Norris, E. Nuss, T. Ohsugi, N. Omodei, E. Orlando, J. F. Ormes, D. Paneque, D. Parent, V. Pelassa, M. Pepe, M. Pesce-Rollins, F. Piron, T. A. Porter, S. Rainò, R. Rando, M. Razzano, S. Razzaque, A. Reimer, O. Reimer, T. Reposeur, S. Ritz, L. S. Rochester, A. Y. Rodriguez, R. W. Romani, M. Roth, F. Ryde, H. F.-W. Sadrozinski, R. Sambruna, D. Sanchez, A. Sander, P. M. Saz Parkinson, J. D. Scargle, C. Sgrò, J. Siskind, D. A. Smith, P. D. Smith, G. Spandre, P. Spinelli, J.-L. Starck, L. Stawarz, M. S. Strickman, D. J. Suson, H. Tajima, H. Takahashi, T. Takahashi, T. Tanaka, J. B. Thayer, J. G. Thayer, D. J. Thompson, L. Tibaldo, D. F. Torres, G. Tosti, A. Tramacere, Y. U. Uchiyama, T. L.,

V. Vasileiou, N. Vilchez, V. Vitale, A. P. Waite, E. Wallace, P. Wang, B. L. Winer, K. S. Wood, T. Ylinen, M. Ziegler, M. J. Hardcastle, D. Kazanas, and Fermi LAT Collaboration. Fermi Gamma-Ray Imaging of a Radio Galaxy. *Science*, 328:725, May 2010.

[6] E. Agol, B. Jones, and O. Blaes. Keck Mid-Infrared Imaging of QSO 2237+0305. *ApJ*, 545:657–663, December 2000.

[7] E. Agol and J. Krolik. Imaging a Quasar Accretion Disk with Microlensing. *ApJ*, 524:49–64, October 1999.

[8] C. Alard. Image subtraction using a space-varying kernel. *A&AS*, 144:363–370, June 2000.

[9] C. Alard and R. H. Lupton. A Method for Optimal Image Subtraction. *ApJ*, 503:325–331, August 1998.

[10] D. Alcalde, E. Mediavilla, O. Moreau, J. A. Muñoz, C. Libbrecht, L. J. Goicoechea, J. Surdej, E. Puga, Y. De Rop, R. Barrena, R. Gil-Merino, B. A. McLeod, V. Motta, A. Oscoz, and M. Serra-Ricart. QSO 2237+0305 VR Light Curves from Gravitational LensES International Time Project Optical Monitoring. *ApJ*, 572:729–734, June 2002.

[11] T. Anguita, R. W. Schmidt, E. L. Turner, J. Wambsganss, R. L. Webster, K. A. Loomis, D. Long, and R. McMillan. The multiple quasar Q2237+0305 under a microlensing caustic. *A&A*, 480:327–334, March 2008.

[12] A. Atoyan and C. D. Dermer. Synchrotron versus Compton Interpretations for Extended X-Ray Jets. *ApJ*, 613:151–158, September 2004.

[13] J. E. Barnes and L. E. Hernquist. Fueling starburst galaxies with gas-rich mergers. *ApJL*, 370:L65–L68, April 1991.

[14] R. D. Blandford and M. J. Rees. A 'twin-exhaust' model for double radio sources. *MNRAS*, 169:395–415, December 1974.

[15] M. Blanton, E. L. Turner, and J. Wambsganss. Ultraviolet images of the gravitationally lensed quadruple quasar Q2237+0305 with the HST WFPC2. *MNRAS*, 298:1223–1232, August 1998.

[16] I. A. Bond, A. Udalski, M. Jaroszyński, N. J. Rattenbury, B. Paczyński, I. Soszyński, L. Wyrzykowski, M. K. Szymański, M. Kubiak, O. Szewczyk, K. Żebruń, G. Pietrzyński, F. Abe, D. P. Bennett, S. Eguchi, Y. Furuta, J. B. Hearnshaw, K. Kamiya, P. M. Kilmartin, Y. Kurata, K. Masuda, Y. Matsubara,

Y. Muraki, S. Noda, K. Okajima, T. Sako, T. Sekiguchi, D. J. Sullivan, T. Sumi, P. J. Tristram, T. Yanagisawa, P. C. M. Yock, and OGLE Collaboration. OGLE 2003-BLG-235/MOA 2003-BLG-53: A Planetary Microlensing Event. *ApJL*, 606:L155–L158, May 2004.

[17] V. Bromm and A. Loeb. Formation of the First Supermassive Black Holes. *ApJ*, 596:34–46, October 2003.

[18] I. Burud, P. Magain, S. Sohy, and J. Hjorth. A novel approach for extracting time-delays from lightcurves of lensed quasar images. *A&A*, 380:805–810, December 2001.

[19] I. Burud, R. Stabell, P. Magain, F. Courbin, R. Ostensen, S. Refsdal, M. Remy, and J. Teuber. Three photometric methods tested on ground-based data of Q 2237+0305. *A&A*, 339:701–708, November 1998.

[20] K. Chang and S. Refsdal. Flux variations of QSO 0957+561 A, B and image splitting by stars near the light path. *Nature*, 282:561–564, December 1979.

[21] V. Chantry, D. Sluse, and P. Magain. COSMOGRAIL: the COSmological MOnitoring of GRAvItational Lenses. VIII. Deconvolution of high resolution near-IR images and simple mass models for 7 gravitationally lensed quasars. *A&A*, 522:A95, November 2010.

[22] D. Chelouche. AGN Outflows: Observations and Their Interpretation. In L. C. Ho and J.-W. Wang, editors, *The Central Engine of Active Galactic Nuclei*, volume 373 of *Astronomical Society of the Pacific Conference Series*, page 277, October 2007.

[23] W. N. Colley, R. E. Schild, C. Abajas, D. Alcalde, Z. Aslan, I. Bikmaev, V. Chavushyan, L. Chinarro, J.-P. Cournoyer, R. Crowe, V. Dudinov, A. K. D. Evans, Y.-B. Jeon, L. J. Goicoechea, O. Golbasi, I. Khamitov, K. Kjernsmo, H. J. Lee, J. Lee, K. W. Lee, M. G. Lee, O. Lopez-Cruz, E. Mediavilla, A. F. J. Moffat, R. Mujica, A. Ullan, J. Muñoz, A. Oscoz, M.-G. Park, N. Purves, O. Saanum, N. Sakhibullin, M. Serra-Ricart, I. Sinelnikov, R. Stabell, A. Stockton, J. Teuber, R. Thompson, H.-S. Woo, and A. Zheleznyak. Around-the-Clock Observations of the Q0957+561A,B Gravitationally Lensed Quasar. II. Results for the Second Observing Season. *ApJ*, 587:71–79, April 2003.

[24] W. N. Colley, I. I. Shapiro, J. Pegg, E. L. Turner, T. Kundić, K. Loomis, N. C. Hastings, and R. McMillan. Rapid Brightness Fluctuations in Q0957+561A,B: Microlensing or Seeing? *ApJ*, 588:711–715, May 2003.

[25] R. T. Corrigan, M. J. Irwin, J. Arnaud, G. G. Fahlman, J. M. Fletcher, P. C. Hewett, J. N. Hewitt, O. Le Fevre, R. McClure, C. J. Pritchet, D. P. Schneider, E. L. Turner, R. L. Webster, and H. K. C. Yee. Initial light curve of Q2237 + 0305. *AJ*, 102:34–40, July 1991.

[26] F. Courbin, V. Chantry, Y. Revaz, D. Sluse, C. Faure, M. Tewes, E. Eulaers, M. Koleva, I. Asfandiyarov, S. Dye, P. Magain, H. van Winckel, J. Coles, P. Saha, M. Ibrahimov, and G. Meylan. COSMOGRAIL: the COSmological MOnitoring of GRAvItational Lenses. IX. Time delays, lens dynamics and baryonic fraction in HE 0435-1223. *A&A*, 536:A53, December 2011.

[27] P. Crane, R. Albrecht, C. Barbieri, J. C. Blades, A. Bokensenberg, J. M. Deharveng, M. J. Disney, P. Jakobsen, T. M. Kamperman, I. R. King, F. Macchetto, C. D. Mackay, F. Paresce, G. Weigelt, D. Baxter, P. Greenfield, R. Jedrzejewski, A. Nota, and W. B. Sparks. First results from the Faint Object Camera - Images of the gravitational lens system G2237 + 0305. *ApJL*, 369:L59–L61, March 1991.

[28] B. Czerny and M. Elvis. Constraints on quasar accretion disks from the optical/ultraviolet/soft X-ray big bump. *ApJ*, 321:305–320, October 1987.

[29] X. Dai, G. Chartas, E. Agol, M. W. Bautz, and G. P. Garmire. Chandra Observations of QSO 2237+0305. *ApJ*, 589:100–110, May 2003.

[30] N. Dalal and C. S. Kochanek. Direct Detection of Cold Dark Matter Substructure. *ApJ*, 572:25–33, June 2002.

[31] M. M. De Robertis and H. K. C. Yee. Spatially Resolved Spectroscopy of Lyα and C IV in the Gravitational Lens 2237+030. In *Bulletin of the American Astronomical Society*, volume 22 of , page 1196, September 1990.

[32] M. M. De Robertis, H. K. C. Yee, and K. Hayhoe. A CCD Study of the Environment of Seyfert Galaxies. II. Testing the Interaction Hypothesis. *ApJ*, 496:93–102, March 1998.

[33] B. Devecchi and M. Volonteri. Formation of the First Nuclear Clusters and Massive Black Holes at High Redshift. *ApJ*, 694:302–313, March 2009.

[34] T. Di Matteo, V. Springel, and L. Hernquist. Energy input from quasars regulates the growth and activity of black holes and their host galaxies. *Nature*, 433:604–607, February 2005.

[35] M. Dominik, U. G. Jørgensen, N. J. Rattenbury, M. Mathiasen, T. C. Hinse, S. Calchi Novati, K. Harpsøe, V. Bozza, T. Anguita, M. J. Burgdorf, K. Horne, M. Hundertmark, E. Kerins, P. Kjærgaard, C. Liebig, L. Mancini, G. Masi,

S. Rahvar, D. Ricci, G. Scarpetta, C. Snodgrass, J. Southworth, R. A. Street, J. Surdej, C. C. Thöne, Y. Tsapras, J. Wambsganss, and M. Zub. Realisation of a fully-deterministic microlensing observing strategy for inferring planet populations. *Astronomische Nachrichten*, 331:671, July 2010.

[36] V. Dudinov, P. Bliokh, B. Paczynski, H. N. Omma, R. Schild, W. Colley, V. Vakulik, A. Zheleznyak, A. Sergeyev, B. Artamonov, S. Nuritdinov, and S. Ehgamberdiev. A program of international cooperative investigation of gravitational lens systems. *Kinematika i Fizika Nebesnykh Tel Supplement*, 3:170–173, September 2000.

[37] V. N. Dudinov, V. G. Vakulik, A. P. Zheleznyak, V. V. Konichek, I. Y. Sinelnikov, V. S. Tsvetkova, A. A. Minakov, B. P. Artamonov, V. V. Bruevich, S. N. Nuritdinov, and I. M. Hamitov. Brightness and colour variations in the Q2237+0305 gravitational lens system from observations of 1997 and 1998. *Kinematika i Fizika Nebesnykh Tel*, 16:346–354, September 2000.

[38] F. W. Dyson, A. S. Eddington, and C. Davidson. A Determination of the Deflection of Light by the Sun's Gravitational Field, from Observations Made at the Total Eclipse of May 29, 1919. *Philosophical Transactions of the Royal Society of London Series A*, 220:291–333, 1920.

[39] A. Eigenbrod, F. Courbin, and G. Meylan. COSMOGRAIL: the COSmological MOnitoring of GRAvItational Lenses. VI. Redshift of the lensing galaxy in seven gravitationally lensed quasars. *A&A*, 465:51–56, April 2007.

[40] A. Eigenbrod, F. Courbin, G. Meylan, E. Agol, T. Anguita, R. W. Schmidt, and J. Wambsganss. Microlensing variability in the gravitationally lensed quasar QSO 2237+0305 = the Einstein Cross. II. Energy profile of the accretion disk. *A&A*, 490:933–943, November 2008.

[41] A. Eigenbrod, F. Courbin, G. Meylan, C. Vuissoz, and P. Magain. COSMOGRAIL: the COSmological MOnitoring of GRAvItational Lenses. III. Redshift of the lensing galaxy in eight gravitationally lensed quasars. *A&A*, 451:759–766, June 2006.

[42] A. Eigenbrod, F. Courbin, D. Sluse, G. Meylan, and E. Agol. Microlensing variability in the gravitationally lensed quasar QSO 2237+0305 = the Einstein Cross. I. Spectrophotometric monitoring with the VLT. *A&A*, 480:647–661, March 2008.

[43] A. Eigenbrod, F. Courbin, C. Vuissoz, G. Meylan, P. Saha, and S. Dye. COSMOGRAIL: The COSmological MOnitoring of GRAvItational Lenses. I. How

to sample the light curves of gravitationally lensed quasars to measure accurate time delays. *A&A*, 436:25–35, June 2005.

[44] A. Einstein. Zur allgemeinen Relativitätstheorie (Nachtrag). *Sitzungsberichte der Königlich Preußischen Akademie der Wissenschaften (Berlin), Seite 799-801*, 1915.

[45] A. Einstein. Lens-Like Action of a Star by the Deviation of Light in the Gravitational Field. *Science*, 84:506–507, December 1936.

[46] M. Elitzur. Unification Issues and the AGN Torus. In L. C. Ho and J.-W. Wang, editors, *The Central Engine of Active Galactic Nuclei*, volume 373 of *Astronomical Society of the Pacific Conference Series*, page 415, October 2007.

[47] E. E. Falco, J. Lehar, R. A. Perley, J. Wambsganss, and M. V. Gorenstein. VLA Observations of the Gravitational Lens System Q2237+0305. *AJ*, 112:897, September 1996.

[48] B. L. Fanaroff and J. M. Riley. The morphology of extragalactic radio sources of high and low luminosity. *MNRAS*, 167:31P–36P, May 1974.

[49] C. Fitte and G. Adam. Sub-arcsecond integral field spectroscopy of the Einstein Cross 2237+0305: Lensing and microlensing effects. *A&A*, 282:11–18, February 1994.

[50] P. J. Francis, P. C. Hewett, C. B. Foltz, F. H. Chaffee, R. J. Weymann, and S. L. Morris. A high signal-to-noise ratio composite quasar spectrum. *ApJ*, 373:465–470, June 1991.

[51] W. L. Freedman, B. F. Madore, B. K. Gibson, L. Ferrarese, D. D. Kelson, S. Sakai, J. R. Mould, R. C. Kennicutt, Jr., H. C. Ford, J. A. Graham, J. P. Huchra, S. M. G. Hughes, G. D. Illingworth, L. M. Macri, and P. B. Stetson. Final Results from the Hubble Space Telescope Key Project to Measure the Hubble Constant. *ApJ*, 553:47–72, May 2001.

[52] M. A. Garrett, R. J. Calder, R. W. Porcas, L. J. King, D. Walsh, and P. N. Wilkinson. Global VLBI Observations of the Gravitational Lens System 0957+561A, B. *MNRAS*, 270:457, September 1994.

[53] B. S. Gaudi. *Microlensing by Exoplanets*, pages 79–110. December 2010.

[54] E. R. Gaynullina, R. W. Schmidt, T. Akhunov, O. Burkhonov, S. Gottlöber, K. Mirtadjieva, S. N. Nuritdinov, I. Tadjibaev, J. Wambsganss, and L. Wisotzki. Microlensing in the double quasar SBS 1520+530. *A&A*, 440:53–58, September 2005.

[55] R. Gil-Merino, L. Wisotzki, and J. Wambsganss. The Double Quasar HE 1104-1805: A case study for time delay determination with poorly sampled lightcurves. *A&A*, 381:428–439, January 2002.

[56] G. Gonzalez, C. Laws, and M. Braunstein. HD 209458. *IAU Circ.*, 7317, September 1999.

[57] J. R. Gott, III. Are heavy halos made of low mass stars - A gravitational lens test. *ApJ*, 243:140–146, January 1981.

[58] B. Grieger and R. Kayser. Microgravitational lenses as keys to quasar structure. *Sterne und Weltraum*, 27:355–357, 1988.

[59] B. Grieger, R. Kayser, and T. Schramm. The deconvolution of the quasar structure from microlensing light curves. *A&A*, 252:508–512, December 1991.

[60] K. Gültekin, D. O. Richstone, K. Gebhardt, T. R. Lauer, S. Tremaine, M. C. Aller, R. Bender, A. Dressler, S. M. Faber, A. V. Filippenko, R. Green, L. C. Ho, J. Kormendy, J. Magorrian, J. Pinkney, and C. Siopis. The M-σ and M-L Relations in Galactic Bulges, and Determinations of Their Intrinsic Scatter. *ApJ*, 698:198–221, June 2009.

[61] M. Hamuy, M. M. Phillips, N. B. Suntzeff, R. A. Schommer, J. Maza, and R. Aviles. The Hubble Diagram of the Calan/Tololo Type IA Supernovae and the Value of HO. *AJ*, 112:2398, December 1996.

[62] D. E. Harris and H. Krawczynski. X-Ray Emission from Extragalactic Jets. *Annual review of astronomy and astrophysics*, 44:463–506, September 2006.

[63] H. Hoekstra and B. Jain. Weak Gravitational Lensing and Its Cosmological Applications. *Annual Review of Nuclear and Particle Science*, 58:99–123, November 2008.

[64] M. Houde and R. Racine. Image restoration and photometric monitoring of the gravitational lens Q2237+0305. *AJ*, 107:466–470, February 1994.

[65] J. Huchra, M. Gorenstein, S. Kent, I. Shapiro, G. Smith, E. Horine, and R. Perley. 2237 + 0305: A new and unusual gravitational lens. *AJ*, 90:691–696, May 1985.

[66] M. J. Irwin, R. L. Webster, P. C. Hewett, R. T. Corrigan, and R. I. Jedrzejewski. Photometric variations in the Q2237 + 0305 system - First detection of a microlensing event. *AJ*, 98:1989–1994, December 1989.

[67] G. Kauffmann and M. Haehnelt. A unified model for the evolution of galaxies and quasars. *MNRAS*, 311:576–588, January 2000.

[68] R. Kayser. Micro gravitation lenses and their significance for astrophysics. *Sterne und Weltraum*, 25:252–254, May 1986.

[69] R. Kayser and S. Refsdal. Detectability of gravitational microlensing in the quasar QSO2237 + 0305. *Nature*, 338:745, April 1989.

[70] A. G. Kim, S. Gabi, G. Goldhaber, D. E. Groom, I. M. Hook, M. Y. Kim, J. C. Lee, C. R. Pennypacker, S. Perlmutter, I. A. Small, A. Goobar, R. Pain, R. S. Ellis, R. G. McMahon, B. J. Boyle, P. S. Bunclark, D. Carter, M. J. Irwin, K. Glazebrook, H. J. M. Newberg, A. V. Filippenko, T. Matheson, M. Dopita, W. J. Couch, and (. S. C. Project). Implications for the Hubble Constant from the First Seven Supernovae at z >= 0.35. *ApJL*, 476:L63–L66, February 1997.

[71] C. S. Kochanek. What Do Gravitational Lens Time Delays Measure? *ApJ*, 578:25–32, October 2002.

[72] C. S. Kochanek. Quantitative Interpretation of Quasar Microlensing Light Curves. *ApJ*, 605:58–77, April 2004.

[73] C. S. Kochanek, N. D. Morgan, E. E. Falco, B. A. McLeod, J. N. Winn, J. Dembicky, and B. Ketzeback. The Time Delays of Gravitational Lens HE 0435-1223: An Early-Type Galaxy with a Rising Rotation Curve. *ApJ*, 640:47–61, March 2006.

[74] L. V. E. Koopmans and CLASS Collaboration. The Hubble Constant from (CLASS) Gravitational Lenses. *Publications of the Astronomical Society of Australia*, 18:179–181, 2001.

[75] E. Koptelova, W. P. Chen, T. Chiueh, B. P. Artamonov, V. L. Oknyanskij, S. N. Nuritdinov, O. Burkhonov, T. Akhunov, V. V. Bruevich, O. V. Ezhkova, A. S. Gusev, A. V. Sergeyev, S. A. Ehgamberdiev, and M. A. Ibragimov. Time delay between images of the lensed quasar UM673. *A&A*, 544:A51, August 2012.

[76] E. Koptelova, V. Oknyanskij, B. Artamonov, and W.-P. Chen. Multiwavelengths observations of lensed quasars: interband time delays. *Memorie della Societa Astronomica Italiana*, 81:138, 2010.

[77] E. A. Koptelova, V. L. Oknyanskij, and E. V. Shimanovskaya. Determining time delay in the gravitationally lensed system QSO2237+0305. *A&A*, 452:37–46, June 2006.

[78] A. Koratkar and O. Blaes. The Ultraviolet and Optical Continuum Emission in Active Galactic Nuclei: The Status of Accretion Disks. *PASP*, 111:1–30, January 1999.

[79] J. Kormendy and R. C. Kennicutt, Jr. Secular Evolution and the Formation of Pseudobulges in Disk Galaxies. *Annual review of astronomy and astrophysics*, 42:603–683, September 2004.

[80] H. Krawczynski and E. Treister. Active galactic nuclei the physics of individual sources and the cosmic history of formation and evolution. *Frontiers of Physics*, 8:609–629, December 2013.

[81] T. Kundić, E. L. Turner, W. N. Colley, J. R. Gott, III, J. E. Rhoads, Y. Wang, L. E. Bergeron, K. A. Gloria, D. C. Long, S. Malhotra, and J. Wambsganss. A Robust Determination of the Time Delay in 0957+561A, B and a Measurement of the Global Value of Hubble's Constant. *ApJ*, 482:75–82, June 1997.

[82] D. W. Latham, R. P. Stefanik, T. Mazeh, M. Mayor, and G. Burki. The unseen companion of HD114762 - A probable brown dwarf. *Nature*, 339:38–40, May 1989.

[83] A. Lawrence. The relative frequency of broad-lined and narrow-lined active galactic nuclei - Implications for unified schemes. *MNRAS*, 252:586–592, October 1991.

[84] G. F. Lewis and K. E. Belle. Microlensing of broad absorption line quasars. *MNRAS*, 297:69–76, June 1998.

[85] G. F. Lewis and R. A. Ibata. Quasar Image Shifts Resulting from Gravitational Microlensing. *ApJ*, 501:478–485, July 1998.

[86] G. F. Lewis and R. A. Ibata. Gravitational microlensing of quasar broad-line regions at large optical depths. *MNRAS*, 348:24–33, February 2004.

[87] G. F. Lewis, M. J. Irwin, P. C. Hewett, and C. B. Foltz. Microlensing-induced spectral variability in Q 2237+0305. *MNRAS*, 295:573, April 1998.

[88] M. S. Longair, M. Ryle, and P. A. G. Scheuer. Models of extended radiosources. *MNRAS*, 164:243, 1973.

[89] D. Lynden-Bell. Galactic Nuclei as Collapsed Old Quasars. *Nature*, 223:690–694, August 1969.

[90] G. M. MacAlpine and F. R. Feldman. Discovery and spectrophotometry of high-redshift quasars. *ApJ*, 261:412–421, October 1982.

[91] J. Machalski, D. Kozieł-Wierzbowska, M. Jamrozy, and D. J. Saikia. J1420-0545: The Radio Galaxy Larger than 3C 236. *ApJ*, 679:149–155, May 2008.

[92] J. Magorrian, S. Tremaine, D. Richstone, R. Bender, G. Bower, A. Dressler, S. M. Faber, K. Gebhardt, R. Green, C. Grillmair, J. Kormendy, and T. Lauer. The Demography of Massive Dark Objects in Galaxy Centers. *AJ*, 115:2285–2305, June 1998.

[93] A. Marconi, G. Risaliti, R. Gilli, L. K. Hunt, R. Maiolino, and M. Salvati. Local supermassive black holes, relics of active galactic nuclei and the X-ray background. *MNRAS*, 351:169–185, June 2004.

[94] R. Massey, T. Kitching, and J. Richard. The dark matter of gravitational lensing. *Reports on Progress in Physics*, 73(8):086901, August 2010.

[95] T. A. Matthews and A. R. Sandage. Optical Identification of 3c 48, 3c 196, and 3c 286 with Stellar Objects. *ApJ*, 138:30, July 1963.

[96] B. A. McLeod, E. E. Falco, J. Lehar, C. D. Impey, C. S. Kochanek, C. Y. Peng, and H.-W. Rix. Lens galaxies revealed: highlights of the CASTLES lens survey. In *American Astronomical Society Meeting Abstracts*, volume 29 of *Bulletin of the American Astronomical Society*, page 1307, December 1997.

[97] B. R. McNamara and P. E. J. Nulsen. Mechanical feedback from active galactic nuclei in galaxies, groups and clusters. *New Journal of Physics*, 14(5):055023, May 2012.

[98] E. Mediavilla, J. Jiménez-Vicente, J. A. Muñoz, and T. Mediavilla. Resolving the Innermost Region of the Accretion Disk of the Lensed Quasar Q2237+0305 through Gravitational Microlensing. *ApJL*, 814:L26, December 2015.

[99] R. B. Metcalf and H. Zhao. Flux Ratios as a Probe of Dark Substructures in Quadruple-Image Gravitational Lenses. *ApJL*, 567:L5–L8, March 2002.

[100] B. Moore, N. Katz, G. Lake, A. Dressler, and A. Oemler. Galaxy harassment and the evolution of clusters of galaxies. *Nature*, 379:613–616, February 1996.

[101] O. Moreau, C. Libbrecht, D.-W. Lee, and J. Surdej. Accurate photometric light curves of the lensed components of Q2237+0305 derived with an optimal image subtraction technique: Evidence for microlensing in image A. *A&A*, 436:479–492, June 2005.

[102] N. D. Morgan, J. A. R. Caldwell, P. L. Schechter, A. Dressler, E. Egami, and H.-W. Rix. WFI J2026-4536 and WFI J2033-4723: Two New Quadruple Gravitational Lenses. *AJ*, 127:2617–2630, May 2004.

[103] D. J. Mortlock, S. J. Warren, B. P. Venemans, M. Patel, P. C. Hewett, R. G. McMahon, C. Simpson, T. Theuns, E. A. Gonzáles-Solares, A. Adamson, S. Dye, N. C. Hambly, P. Hirst, M. J. Irwin, E. Kuiper, A. Lawrence, and H. J. A. Röttgering. A luminous quasar at a redshift of z = 7.085. *Nature*, 474:616–619, June 2011.

[104] M. J. Mortonson, P. L. Schechter, and J. Wambsganss. Size Is Everything: Universal Features of Quasar Microlensing with Extended Sources. *ApJ*, 628:594–603, August 2005.

[105] D. Nadeau, H. K. C. Yee, W. J. Forrest, J. D. Garnett, Z. Ninkov, and J. L. Pipher. Infrared and visible photometry of the gravitational lens systems 2237 + 030. *ApJ*, 376:430–438, August 1991.

[106] M. Nenkova, M. M. Sirocky, Ž. Ivezić, and M. Elitzur. AGN Dusty Tori. I. Handling of Clumpy Media. *ApJ*, 685:147–159, September 2008.

[107] E. O. Ofek, D. Maoz, H.-W. Rix, C. S. Kochanek, and E. E. Falco. Spectroscopic Redshifts for Seven Lens Galaxies. *ApJ*, 641:70–77, April 2006.

[108] R. Ostensen, S. Refsdal, R. Stabell, J. Teuber, P. I. Emanuelsen, L. Festin, R. Florentin-Nielsen, G. Gahm, E. Gullbring, F. Grundahl, J. Hjorth, M. Jablonski, A. O. Jaunsen, A. A. Kaas, H. Karttunen, J. Kotilainen, E. Laurikainen, H. Lindgren, P. Maehoenen, K. Nilsson, G. Olofsson, O. Olsen, B. R. Pettersen, V. Piirola, A. N. Sorensen, L. Takalo, B. Thomsen, E. Valtaoja, M. Vestergaard, and T. Av Vianborg. Monitoring of the Einstein Cross with the Nordic Optical Telescope. *A&A*, 309:59–64, May 1996.

[109] B. Paczynski. Gravitational microlensing at large optical depth. *ApJ*, 301:503–516, February 1986.

[110] B. Paczynski. Gravitational microlensing by the galactic halo. *ApJ*, 304:1–5, May 1986.

[111] B. Paczynski and A. Udalski. Optical Gravtational Lensing Experiment (OGLE). *IAU Circ.*, 5997, May 1994.

[112] R. Pello, B. Sanahuja, J.-F. Le Borgne, G. Soucail, and Y. Mellier. A straight gravitational image in Abell 2390 - A striking case of lensing by a cluster of galaxies. *ApJ*, 366:405–411, January 1991.

[113] J. Pelt, R. Kayser, S. Refsdal, and T. Schramm. The light curve and the time delay of QSO 0957+561. *A&A*, 305:97, January 1996.

[114] C. Y. Peng, E. E. Falco, J. Lehar, C. D. Impey, C. S. Kochanek, B. A. McLeod, and H.-W. Rix. The CASTLES Imaging Survey of Gravitational Lenses. In *American Astronomical Society Meeting Abstracts*, volume 29 of *Bulletin of the American Astronomical Society*, page 1348, December 1997.

[115] C. Y. Peng, L. C. Ho, C. D. Impey, and H.-W. Rix. Detailed Structural Decomposition of Galaxy Images. *AJ*, 124:266–293, July 2002.

[116] N. A. Pereyra, D. E. Vanden Berk, D. A. Turnshek, D. J. Hillier, B. C. Wilhite, R. G. Kron, D. P. Schneider, and J. Brinkmann. Characteristic QSO Accretion Disk Temperatures from Spectroscopic Continuum Variability. *ApJ*, 642:87–95, May 2006.

[117] B. M. Peterson. The Masses of Black Holes in Active Galactic Nuclei. In L. C. Ho and J.-W. Wang, editors, *The Central Engine of Active Galactic Nuclei*, volume 373 of *Astronomical Society of the Pacific Conference Series*, page 3, October 2007.

[118] L. Č. Popović, P. Jovanović, E. Mediavilla, A. F. Zakharov, C. Abajas, J. A. Muñoz, and G. Chartas. A Study of the Correlation between the Amplification of the Fe Kα Line and the X-Ray Continuum of Quasars due to Microlensing. *ApJ*, 637:620–630, February 2006.

[119] R. Racine. Continuum and semiforbidden C III microlensing in Q2237 + 0305 and the quasar geometry. *ApJL*, 395:L65–L67, August 1992.

[120] M. J. Rees. New Interpretation of Extragalactic Radio Sources. *Nature*, 229:312–317, January 1971.

[121] S. Refsdal. On the possibility of determining Hubble's parameter and the masses of galaxies from the gravitational lens effect. *MNRAS*, 128:307, 1964.

[122] S. Refsdal, R. Stabell, J. Pelt, and R. Schild. Constraints on source and lens parameters from microlensing variability in QSO 0957+561 A,B. *A&A*, 360:10–14, August 2000.

[123] D. Reimers, T. Koehler, and L. Wisotzki. The Hamburg/ESO survey for bright QSOs. II. Follow-up spectroscopy of 160 quasars and Seyferts. *A&AS*, 115:235, February 1996.

[124] D. Ricci, A. Elyiv, F. Finet, O. Wertz, K. Alsubai, T. Anguita, V. Bozza, P. Browne, M. Burgdorf, S. Calchi Novati, P. Dodds, M. Dominik, S. Dreizler, T. Gerner, M. Glitrup, F. Grundahl, S. Hardis, K. Harpsøe, T. C. Hinse, A. Hornstrup, M. Hundertmark, U. G. Jørgensen, N. Kains, E. Kerins, C. Liebig,

G. Maier, L. Mancini, G. Masi, M. Mathiasen, M. Penny, S. Proft, S. Rahvar, G. Scarpetta, K. Sahu, S. Schäfer, F. Schönebeck, R. Schmidt, J. Skottfelt, C. Snodgrass, J. Southworth, C. C. Thöne, J. Wambsganss, F. Zimmer, M. Zub, and J. Surdej. Flux and color variations of the doubly imaged quasar UM673. *A&A*, 551:A104, March 2013.

[125] D. Ricci, J. Poels, A. Elyiv, F. Finet, P. G. Sprimont, T. Anguita, V. Bozza, P. Browne, M. Burgdorf, S. Calchi Novati, M. Dominik, S. Dreizler, M. Glitrup, F. Grundahl, K. Harpsøe, F. Hessman, T. C. Hinse, A. Hornstrup, M. Hundertmark, U. G. Jørgensen, C. Liebig, G. Maier, L. Mancini, G. Masi, M. Mathiasen, S. Rahvar, G. Scarpetta, J. Skottfelt, C. Snodgrass, J. Southworth, J. Teuber, C. C. Thöne, J. Wambsganß, F. Zimmer, M. Zub, and J. Surdej. Flux and color variations of the quadruply imaged quasar HE 0435-1223. *A&A*, 528:A42, April 2011.

[126] G. T. Richards, C. R. Keeton, B. Pindor, J. F. Hennawi, P. B. Hall, E. L. Turner, N. Inada, M. Oguri, S.-I. Ichikawa, R. H. Becker, M. D. Gregg, R. L. White, J. S. B. Wyithe, D. P. Schneider, D. E. Johnston, J. A. Frieman, and J. Brinkmann. Microlensing of the Broad Emission Line Region in the Quadruple Lens SDSS J1004+4112. *ApJ*, 610:679–685, August 2004.

[127] H.-W. Rix, D. P. Schneider, and J. N. Bahcall. Hubble Space Telescope Wide Field Camera imaging of the gravitational lens 2237 + 0305. *AJ*, 104:959–967, September 1992.

[128] D. B. Sanders, B. T. Soifer, J. H. Elias, B. F. Madore, K. Matthews, G. Neugebauer, and N. Z. Scoville. Ultraluminous infrared galaxies and the origin of quasars. *ApJ*, 325:74–91, February 1988.

[129] A. B. Saust. Determining the size of the emission line region in Q2237+031 from microlensing. *A&AS*, 103, January 1994.

[130] P. L. Schechter and J. Wambsganss. Quasar Microlensing at High Magnification and the Role of Dark Matter: Enhanced Fluctuations and Suppressed Saddle Points. *ApJ*, 580:685–695, December 2002.

[131] P. A. G. Scheuer. Models of extragalactic radio sources with a continuous energy supply from a central object. *MNRAS*, 166:513–528, March 1974.

[132] M. Schmidt. 3C 273 : A Star-Like Object with Large Red-Shift. *Nature*, 197:1040, March 1963.

[133] R. Schmidt, R. L. Webster, and G. F. Lewis. Weighing a galaxy bar in the lens Q2237 + 0305. *MNRAS*, 295:488, April 1998.

[134] R. W. Schmidt and J. Wambsganss. Quasar microlensing. *General Relativity and Gravitation*, 42:2127–2150, September 2010.

[135] D. P. Schneider, E. L. Turner, J. E. Gunn, J. N. Hewitt, M. Schmidt, and C. R. Lawrence. Erratum: High-Resolution CCD Imaging and Derived Gravitational Lens Models of 2237+0305 (A.J. 95, 1619 (1988). *AJ*, 96:1755, November 1988.

[136] P. Schneider. A new formulation of gravitational lens theory, time-delay, and Fermat's principle. *A&A*, 143:413–420, February 1985.

[137] P. Schneider and J. Wambsganss. Are the broad emission lines of quasars affected by gravitational microlensing? *A&A*, 237:42–53, October 1990.

[138] N. I. Shakura and R. A. Sunyaev. Black holes in binary systems. Observational appearance. *A&A*, 24:337–355, 1973.

[139] F. Shankar, P. Salucci, G. L. Granato, G. De Zotti, and L. Danese. Supermassive black hole demography: the match between the local and accreted mass functions. *MNRAS*, 354:1020–1030, November 2004.

[140] G. A. Shields. Thermal continuum from acretion disks in quasars. *Nature*, 272:706–708, April 1978.

[141] D. Sluse, M. Kishimoto, T. Anguita, O. Wucknitz, and J. Wambsganss. Mid-infrared microlensing of accretion disc and dusty torus in quasars: effects on flux ratio anomalies. *A&A*, 553:A53, May 2013.

[142] A. Smette, J. Surdej, P. A. Shaver, C. B. Foltz, F. H. Chaffee, R. J. Weymann, R. E. Williams, and P. Magain. A spectroscopic study of UM 673 A and B - On the size of Lyman-alpha clouds. *ApJ*, 389:39–62, April 1992.

[143] A. Soltan. Masses of quasars. *MNRAS*, 200:115–122, July 1982.

[144] L. S. Sparke and J. S. Gallagher, III. *Galaxies in the Universe*. February 2007.

[145] J. Surdej, P. Magain, J.-P. Swings, U. Borgeest, T. J.-L. Courvoisier, R. Kayer, K. I. Kellermann, H. Kuhr, and S. Refsdal. Observations of the new gravitational lens system UM 673 = Q 0142-100. *A&A*, 198:49–60, June 1988.

[146] J. Surdej, P. Magain, J.-P. Swings, U. Borgeest, T. J.-L. Courvoisier, R. Kayser, K. I. Kellermann, H. Kuhr, and S. Refsdal. A new case of gravitational lensing. *Nature*, 329:695, October 1987.

[147] M. Tewes, F. Courbin, and G. Meylan. COSMOGRAIL: the COSmological MOnitoring of GRAvItational Lenses. XI. Techniques for time delay measurement in presence of microlensing. *A&A*, 553:A120, May 2013.

[148] E. Treister, P. Natarajan, D. B. Sanders, C. M. Urry, K. Schawinski, and J. Kartaltepe. Major Galaxy Mergers and the Growth of Supermassive Black Holes in Quasars. *Science*, 328:600, April 2010.

[149] E. Treister, K. Schawinski, C. M. Urry, and B. D. Simmons. Major Galaxy Mergers Only Trigger the Most Luminous Active Galactic Nuclei. *ApJL*, 758:L39, October 2012.

[150] E. Treister and C. M. Urry. The Evolution of Obscuration in Active Galactic Nuclei. *ApJL*, 652:L79–L82, December 2006.

[151] E. Treister, C. M. Urry, and S. Virani. The Space Density of Compton-Thick Active Galactic Nucleus and the X-Ray Background. *ApJ*, 696:110–120, May 2009.

[152] M. Treyer and J. Wambsganss. Astrometric microlensing of quasars. Dependence on surface mass density and external shear. *A&A*, 416:19–34, March 2004.

[153] A. Udalski, M. K. Szymanski, M. Kubiak, G. Pietrzynski, I. Soszynski, K. Zebrun, O. Szewczyk, L. Wyrzykowski, K. Ulaczyk, and T. Wiêckowski. The Optical Gravitational Lensing Experiment. OGLE-III Long Term Monitoring of the Gravitational Lens QSO 2237+0305. *Acta Astronomica*, 56:293–305, December 2006.

[154] V. Vakulik, R. Schild, V. Dudinov, S. Nuritdinov, V. Tsvetkova, O. Burkhonov, and T. Akhunov. Observational determination of the time delays in gravitational lens system Q2237+0305. *A&A*, 447:905–913, March 2006.

[155] V. G. Vakulik, V. N. Dudinov, A. P. Zheleznyak, V. S. Tsvetkova, P. Notni, V. N. Shalyapin, and B. P. Artamonov. VRI photometry of the Einstein Cross Q2237+0305 at Maidanak observatory. *Astronomische Nachrichten*, 318:73, February 1997.

[156] V. G. Vakulik, R. E. Schild, V. N. Dudinov, A. A. Minakov, S. N. Nuritdinov, V. S. Tsvetkova, A. P. Zheleznyak, V. V. Konichek, I. Y. Sinelnikov, O. A. Burkhonov, B. P. Artamonov, and V. V. Bruevich. Color effects associated with the 1999 microlensing brightness peaks in gravitationally lensed quasar Q2237+0305. *A&A*, 420:447–457, June 2004.

[157] D. E. Vanden Berk, B. C. Wilhite, R. G. Kron, S. F. Anderson, R. J. Brunner, P. B. Hall, Ž. Ivezić, G. T. Richards, D. P. Schneider, D. G. York, J. V. Brinkmann, D. Q. Lamb, R. C. Nichol, and D. J. Schlegel. The Ensemble Photometric Variability of ˜25,000 Quasars in the Sloan Digital Sky Survey. *ApJ*, 601:692–714, February 2004.

[158] C. Vuissoz, F. Courbin, D. Sluse, G. Meylan, V. Chantry, E. Eulaers, C. Morgan, M. E. Eyler, C. S. Kochanek, J. Coles, P. Saha, P. Magain, and E. E. Falco. COSMOGRAIL: the COSmological MOnitoring of GRAvItational Lenses. VII. Time delays and the Hubble constant from WFI J2033-4723. *A&A*, 488:481–490, September 2008.

[159] D. Walsh, R. F. Carswell, and R. J. Weymann. 0957 + 561 A, B - Twin quasistellar objects or gravitational lens. *Nature*, 279:381–384, May 1979.

[160] J. Wambsganss. Gravitational Microlensing. *ArXiv Astrophysics e-prints*, April 2006.

[161] J. Wambsganss and B. Paczynski. Expected color variations of the gravitationally microlensed QSO 2237 + 0305. *AJ*, 102:864–868, September 1991.

[162] J. Wambsganss and B. Paczynski. A direct gravitational lensing test for 10 exp 6 solar masses black holes in halos of galaxies. *ApJL*, 397:L1–L4, September 1992.

[163] J. Wambsganss and B. Paczynski. Parameter degeneracy in models of the quadruple lens system Q2237+0305. *AJ*, 108:1156–1162, October 1994.

[164] J. Wambsganss, B. Paczynski, and P. Schneider. Interpretation of the microlensing event in QSO 2237 + 0305. *ApJL*, 358:L33–L36, August 1990.

[165] J. Wambsganss, R. W. Schmidt, W. Colley, T. Kundić, and E. L. Turner. Microlensing results from APO monitoring of the double quasar Q0957+561A,B between 1995 and 1998. *A&A*, 362:L37–L40, October 2000.

[166] L. L. R. Williams and P. Saha. Improper Motions in Lensed QSOs. *AJ*, 110:1471, October 1995.

[167] C. J. Willott, L. Albert, D. Arzoumanian, J. Bergeron, D. Crampton, P. Delorme, J. B. Hutchings, A. Omont, C. Reylé, and D. Schade. Eddington-limited Accretion and the Black Hole Mass Function at Redshift 6. *AJ*, 140:546–560, August 2010.

[168] L. Wisotzki, T. Becker, L. Christensen, A. Helms, K. Jahnke, A. Kelz, M. M. Roth, and S. F. Sanchez. Integral-field spectrophotometry of the quadruple QSO HE 0435-1223: Evidence for microlensing. *A&A*, 408:455–463, September 2003.

[169] L. Wisotzki, N. Christlieb, N. Bade, V. Beckmann, T. Köhler, C. Vanelle, and D. Reimers. The Hamburg/ESO survey for bright QSOs. III. A large flux-limited sample of QSOs. *A&A*, 358:77–87, June 2000.

[170] L. Wisotzki, T. Koehler, D. Groote, and D. Reimers. The Hamburg/ESO survey for bright QSOs. I. Survey design and candidate selection procedure. *A&AS*, 115:227, February 1996.

[171] L. Wisotzki, P. L. Schechter, H. V. Bradt, J. Heinmüller, and D. Reimers. HE 0435-1223: A wide separation quadruple QSO and gravitational lens. *A&A*, 395:17–23, November 2002.

[172] L. Wisotzki, P. L. Schechter, H.-W. Chen, D. Richstone, K. Jahnke, S. F. Sánchez, and D. Reimers. HE 0047-1756: A new gravitationally lensed double QSO. *A&A*, 419:L31–L34, May 2004.

[173] P. R. Woźniak, C. Alard, A. Udalski, M. Szymański, M. Kubiak, G. Pietrzyński, and K. Zebruń. The Optical Gravitational Lensing Experiment Monitoring of QSO 2237+0305. *ApJ*, 529:88–92, January 2000.

[174] P. R. Woźniak, A. Udalski, M. Szymański, M. Kubiak, G. Pietrzyński, I. Soszyński, and K. Żebruń. The Optical Gravitational Lensing Experiment: A Hunt for Caustic Crossings in QSO 2237+0305. *ApJL*, 540:L65–L67, September 2000.

[175] J. S. B. Wyithe, R. L. Webster, and E. L. Turner. A small source in Q2237+0305? *MNRAS*, 318:762–768, November 2000.

[176] R.-z. Yang, N. Sahakyan, E. D. O. Wilhelmi, F. Aharonian, and F. Rieger. Deep observation of the giant radio lobes of Centaurus A with the Fermi large area telescope. In F. A. Aharonian, W. Hofmann, and F. M. Rieger, editors, *American Institute of Physics Conference Series*, volume 1505 of *American Institute of Physics Conference Series*, pages 590–593, December 2012.

[177] H. K. C. Yee. High-resolution imaging of the gravitational lens system candidate 2237+030. *AJ*, 95:1331–1339, May 1988.

[178] A. Yonehara. Evidence for a Source Size of Less than 2000 AU in Quasar 2237+0305. *ApJL*, 548:L127–L130, February 2001.

[179] A. Yonehara, S. Mineshige, T. Manmoto, J. Fukue, M. Umemura, and E. L. Turner. An X-Ray Microlensing Test of AU-Scale Accretion Disk Structure in Q2237+0305. *ApJL*, 501:L41–L44, July 1998.

[180] P. Young, J. E. Gunn, J. B. Oke, J. A. Westphal, and J. Kristian. Q0957+561 - Detailed models of the gravitational lens effect. *ApJ*, 244:736–755, March 1981.

[181] F. Zwicky. Nebulae as Gravitational Lenses. *Physical Review*, 51:290–290, February 1937.

[182] F. Zwicky. On the Probability of Detecting Nebulae Which Act as Gravitational Lenses. *Physical Review*, 51:679–679, April 1937.

Acknowledgements

Apparently I made it to the end against the odds.
And if this happened it is just because of a few very special people I met on my way. It's the time to say thank you to everyone has accompanied and sometimes, I'd dare say, pushed me through this long journey.
I would like to thank my supervisor Professor Joachim Wambsganß for advice, support during all the stages of this work, and for the infinite and unique understanding regarding my private life events.
I owe my deepest gratitude to Dr. Robert W. Schmidt for help, suggestions, support, computational advice, especially when it seemed that our project had led us to what we used to define a "Cul-de-sac". Thank you for always being so enthusiastic about the "Quasar microlensing business" and having helped me digging into dirt!
A special thank you goes to Dr. Anna Pasquali, the backbone of the second floor at the ARI Neubau. My time at ARI would have been much sadder without having such a cheerful person next door. Thanks for the scientifical support and the funny chats, the shortest lunches of our lives and the shopaholic Saturdays.
Thanks to Christiane, Frederik, Clio and Giulio for having shared their time and thoughts with me at the ARI coffee breaks.
A special thanks goes to Federica e Alessandra. Due forze della natura. You made me laugh so much.
Thanks to all the fellows of this adventure, the 7th IMPRS generation, for sharing with me their triumphs and despair.
Anahí and Jan, you made my life easier and nicer more than once.
A special thank you goes to my officemate, Svea, for useful discussions, for helping me filling up otherwise unbearable german forms, and for keeping each other very good company.
Eleonora, grazie della tua presenza confortante e della tua ironia.
Camilla, la mia vicina di casa. Mi hai aiutato tanto nel momento del bisogno e offerto un'altra finestra sul mondo.
Agnese I am grateful for having met you on that airplane. We went through a long journey together and I am not going to forget all the things we shared, la disperazione, l'aridità e la passione per i dolci. Grazie della tua dolcezza e mitezza.
Many many special thanks to my flatmates: Anja, Jassi, Isa. I very much enjoyed our WG trips and reunions through Germany after we had to split up.
Grazie a Martina, tra le poche certezze di questa vita.
Un ringraziamento speciale va alla mia famiglia, Ennio, Marina e Clarissa, il cui supporto mi ha aiutato a varcare il traguardo. Grazie per l'incalcolabile aiuto che mi offrite mentre attraverso un momento difficile.
Un grazie speciale va infine al mio caro Luca, per essere sempre e comunque al mio fianco, e spronarmi a vedere quella lucina giù in fondo.

List of Publications

[1] Giannini E. and Lunine J.I. Microlensing detection of extrasolar planets. *Reports on Progress in Physics*, 76, May 2013.

[2] Giannini E. et al. MiNDSTEp differential photometry of the gravitationally lensed quasars WFI2033-4723 and HE0047-1756: Microlensing and a new time delay. Accepted for publication in A&A.

[3-9] MiNDSTEp member in 2012 and coauthor of a series of papers published by the MiNDSTEp collaboration since 2013.

Statement of Authorship - Selbständigkeitserklärung

Ich, Emanuela Giannini, versichere, dass ich die vorgelegte Dissertation selbstständig verfasst habe und keine anderen als die angegebenen Quellen und Hilfsmittel benutzt habe.